UC San Diego

UC San Diego Electronic Theses and Dissertations

Title

Preparations, properties, and applications of periodic nano arrays using anodized aluminum oxide and di-block copolymer

Permalink

https://escholarship.org/uc/item/93p8n773

Author

Noh, Kunbae

Publication Date

2011

Peer reviewed|Thesis/dissertation

eScholarship.org Powered by the California Digital Library
University of California

UNIVERSITY OF CALIFORNIA, SAN DIEGO

Preparations, Properties, and Applications of Periodic Nano Arrays using Anodized Aluminum Oxide and Di-block Copolymer

A dissertation submitted in partial satisfaction of the

requirements for the degree Doctor of Philosophy

in

Materials Science and Engineering

by

Kunbae Noh

Committee in Charge:

Professor Sungho Jin, Chair
Professor Jennifer Cha
Professor Yu-Hwa Lo
Professor Vlado Lubarda
Professor Yu Qiao

2011

Copyright

Kunbae Noh, 2011

All rights reserved

The dissertation of Kunbae Noh is approved, and it is acceptable in quality and form for publication on microfilm:

Chair

University of California, San Diego

2011

Dedicated to

my family

"There are two ways to live: you can live as if nothing is a miracle; you can live as if everything is a miracle."

Albert Einstein

TABLE OF CONTENTS

Signature page....iii
Dedication....iv
Epigraph....v
Table of Contents....vi
List of Figures....ix
List of Tables....xv
Acknowledgements....xvi
Vita....xix
Abstract of the Dissertation....xxiv
CHAPTER 1: Introduction....1
CHAPTER 2: Background....3
2.1 Aluminum anodization....3
2.1.1 Self-organized AAO....3
2.1.1.1 Self-ordering regime....4
2.1.1.2 Controlling factors for self-ordereing phenomena....7
2.1.2 Guided AAO self-assembly....10
2.1.2.1 Serial guiding process....10
2.1.2.2 Parallel guiding process....12
2.1.2.3 Emerging guiding process....14
2.1.3 Hard anodization....16
2.1.4 Modified AAO nanostructures....20
2.2 Block copolymer....23
2.1.1 Self-organized BCP....25
2.1.1 Directed BCP....25
CHAPTER 3: Nanoimprint-guided AAO on Al thin film....30
3.1 Introduction....29
3.2 Experimental procedures....30
3.2.1 Al thin film deposition....30
3.2.2 Master mold fabrication....30

3.2.3 Nanoimprint 31
3.2.4 Pattern transfer 31
3.2.5 Anodization 33
3.2.6 Characterization 34
3.3 Results and discussion 34
3.3.1 Al thin film roughness control 34
3.3.2 Guided anodization 38
3.3.3 Al thin film surface engineering 42
3.4 Summary 47
3.5 Future work 47

CHAPTER 4: Fabrication and applications of self-assembled S4VP directed AAO template 51

4.1 Introduction 49
4.1.1 Magnetic multilayer for bit patterned media (BPM) 49
4.1.2 S4VP-guided Al thin film anodization and magnetic nanowires synthesis 51
4.2 Experimental procedures 52
4.2.1 Si substrate pre-treatment 52
4.2.2 Thin film deposition 52
4.2.3 BCP film fabrication 52
4.2.4 Pattern transfer 53
4.2.4.1 Si wafer 53
4.2.4.2 Al thin film 54
4.2.5 Guided anodization 54
4.2.6 Co/Pd magnetic multilayer deposition 54
4.2.7 NiNWs Electrodeposition 55
4.2.8 Characterization 57
4.3 Experimental procedures 57
4.3.1 Structural evolution of S4VP self-assembly 57
4.3.2 Pattern transfer 59
4.3.3 Templates for magnetic materials synthesis 64
4.3.3.1 Alternative Co/Pd multilayer 64

4.3.3.2 NiNWs 68
4.4 Summary 72
4.5 Future work on BCP-guided AAO 73

CHAPTER 5: Novel nanotubular AAO nanostructures and its biomedical applications 77

5.1 Introduction 75
5.2 Experimental procedures 76
5.2.1 Al foil pre-treatment 76
5.2.2 Anodization 78
5.2.3 Substrate transfer 78
5.2.4 Porosity and surface area calculation 80
5.2.5 Cell culture assay for adhesion and viability 81
5.2.6 Antibiotic loading, release, and collection 82
5.3 Results and discussion 83
5.3.1 Nanostructure evolution 83
5.3.2 Cell culture assay for adhesion and viability 91
5.3.3 Drug loading and release 93
5.4 Summary 102
5.5 Future work 103

CHAPTER 6: Overall Summary, Conclusions, and Future Work 108

REFERENCES 111

LIST OF FIGURES

Figure 2.1: Schematic diagram of (a) porous alumina with structural parameters[10] and (b) volume expansion of Al during anodic oxidation. Existing pore walls are pushed upwards.[9] 4

Figure 2.2: SEM micrographs of self-ordered porous AAO (mild anodization) in various dimension anodized at: (a) 25V in sulfuric acid,[12] (b) 40V in oxalic acid,[14] and (c) 195V in phosphoric acid.[13] 5

Figure 2.3: SEM micrographs of recently found self-ordered porous AAO (hard anodization) in various dimension anodized at: (a) 140V in malonic acid (barrier layer),[15] (b) 140V in oxalic acid,[16] and (c) graphical summary of self-ordering regime reported.[16] 6

Figure 2.4 Representative SEM micrographs of serial guided anodization: (a) e-beam lithography-assisted AAO, (this work) (b) AFM image of FIB-guided AAO,[26] (c) indentation of SPM-guided AAO,[27] and (d) holographic lithography-induced AAO.[11] 12

Figure 2.5: Representative SEM micrographs of parallel guided anodization: (a) self-ordered (left) and NIL-assisted AAO (right),[31] (b) NIL-assisted AAO pattern multiplication on Al foil,[35] (c) on Al thin film, (this work) and (d) NIL-assisted AAO patternPS-b-P4VP BCP-guided AAO.[36] 14

Figure 2.6: Self-repair of the pattern with periodic deficiencies: (a) SiC master mold (top) and guided AAO (bottom),[33] and (b) the mosaic composite composed of gold (bright dots) and nickel (dark dots).[34] 15

Figure 2.7: Schematic illustration of “Millipede” concept for future 2D AFM cantilever array.[40] 16

Figure 2.8: Dip-pen lithography (DPN) : (a) single DPN[41] and (b,c,d) parallel-probe DPN: (b) SEM image of a high-density, 2D array of passive DPN probes, (c) SEM images of a commercial “Massively Parallel Pen” (MPP) array and (d) fluorescence micrograph of spots written with the MPP array.[42] 17

Figure 2.9: Hard anodization vs. mild anodization[16]: (a) Film thickness as a function of anodizing time of HA (blue line) and MA (red line) and (b) SEM micrographs of the corresponding AAO samples formed by MA (left column) and HA (right column) for 2 hr, respectively, (c) current-time transients during HA in 0.3M oxalic acid at 1℃ with reference transient during MA (denoted as 40V) in the same condition, and (b) the evolution of interpore distance (D_{int}), pore diameter (D_p) and porosity (P) as a function of the HA voltage. 19

Figure 2.10: Modulation of pore diameter by pulsed anodization: (a) scheme for the fabrication of AAO with modulated pore diameters and (b) SEM micrograph representing the cross-sectional view of an as-anodized AAO.[17] 21

Figure 2.11: Various nanostructures derived from modified anodization techniques. (a) pore wall oscillation by spontaneous current oscillation,[44] (b) serrated pore channel,[45] (c) perforated pore wall by cyclic anodization,[49] (d) bimodal pore distribution by constant current anodization,[50] (e) hollow structured pore arrangement by ultra-high voltage anodization,[51] and (f) arrayed AAO nanotubes by constant voltage anodization (this work) 24

Figure 2.12: Evolution of structure with the combined parameter χN for a symmetric, di-block copolymer with f = 0.5. When $\chi N \sim 10$, small variations in system entropy ($\sim$ N-1) or energy ($\sim\chi$) leads to ordered ($\chi N \geq 10$) or disordered ($\chi N \leq 10$) states. A homogeneous composition profile (Φ_A vs r) results when entropic factors dominate ($\chi N << 10$), whereas a strongly microphase segregated pattern characterizes the limit where energetic factors prevail ($\chi N >> 10$).[62] 25

Figure 2.13: Representative guided BCP array of PS-b-PMMA on an e-beam patterned PS/SiO_x substrate: (a) schematic fabrication process (A-D) and SEM images of e-beam pre-patterns (E) and BCP patterns by means of density multiplication (F), and (b) SEM images of developed e-beam resist (A-D) and the block copolymer film (E-H) on top of the prepattern defined by the corresponding e-beam pattern above.[65] 28

Figure 2.14: Representative guided BCP array of PS-b-PEO on highly oriented crystalline facets on a single crystal sapphire: (a) schematic fabrication process (A-D) and (b) AFM phase images of BCP having different M_n, (E) 25.4kg/mol and (F) 7.0kg/mol[66] 29

Figure 3.1: Schematic illustration of the Si nanotemplate fabrication process using DUV lithography.[78] 33

Figure 3.2: SEM micrographs of NIL stamps: (a) hexagonally arranged Si tip and (b) triangularly arranged Si tip. 33

Figure 3.3: Two strategies for pattern multiplication: (a) self-healing and (b) pattern tripling. 34

Figure 3.4: Schematic illustration of guided anodization procedures: (a) Nano-indentation imprinting on spin coated PMMA layer, (b) RIE process for pattern transfer to underlying Al film layer, (c) PMMA removal, and (d) anodization using the nano-indented array as nucleation sites. 35

Figure 3.5: (a) Surface roughness of Al films sputter deposited on Si substrate at various temperatures and at different overall Al film thicknesses and representative AFM images of 500nm-thick Al films deposited at (b) 25℃ and (c) -90℃ 38

Figure 3.6: Anodized Al_2O_3 morphology and interpore distance on indentation-implanted Al film samples as a function of applied anodization voltage. 40

Figure 3.7: SEM micrographs of PMMA assisted process: (a) pre-patterned Al film surface after removing PMMA residue after patterns transfer, (b) the resulting AAO surface viewed at an angle, and (c) low magnification image representing highly long-range ordered AAO structures, which is evident pores were guided at the dimples location and newly formed at the center of six pre-patterns surrounding. The arrows in (b) show newly created pores in the center of pseudo hexagon during anodization. The sample was anodized in 0.17M phosphoric acid at 130V 42

Figure 3.8: Top-view ((a),(b),(c)) and tilted-view ((d),(e),(f)) SEM images of AAO surface modification engineered by dry etching (RIE) of nano-indented PMMA prior to guided anodization: (a,d) a periodic nanopores, (b,e) a nano-donut, and (c,f) a nanotube array structure (pore widening for 70 minutes). Two consecutive dry etching recipes for PMMA first and then for Al underlayer were used for pattern replication. RIE etching time for PMMA and Al, respectively, was (90s, 60s) in (a,d), (120s, 60s) in (b,e), and (150s, 90s) in (c,f). The corresponding surface structures after RIE and guided anodization are schematically illustrated in the top panel. The subsequent anodization was conducted in 0.17M phosphoric acid at 130V. 45

Figure 3.9: SEM photographs of the sample directly imprinted on Al film: (a) pre-patterned Al film surface after nanoimprint process, (b) the resulting AAO surface ensuring ordered fashion of the result AAO, (c) image at an angle, and (d) the cross-sectional image representing pores were vertically grown to Si substrate. The sample was anodized in 0.04M oxalic acid at 120V and pores were widened for 30 minutes. Note that the bottom of pre-patterned pores has no barrier layer while that of the newly created ones surrounded by pre-patterns has yet hemispherical barrier layer representing pores at the dimples reached Si substrate faster than the newly formed pores which might result from time delay due to pore initiation at the center of each hexagon.. 46

Figure 3.10: Triangular patterned Al nano-indentation on Al film and guided anodization for pattern tripling: (a) schematics for triangular indentation, (b) pattern tripling by self assembly anodization, (c) SEM micrograph of anodized AAO structure, and (d) microstructure after pore widening for 60 minutes. The arrows in (c) and (d) show newly created pores at the in-between spaces during anodization.. 47

Figure 3.11: Schematic daughter stamp fabrication procedures: (a) nanoimprinting on PMMA resist, (b) pattern transfer into Al film surface by RIE, (c) PMMA removal, (d) guided anodization, (e) pattern transfer into Si substrate by RIE, (f) AAO removal, (g) nanoimprinting on PMMA resist, and (h) pattern transfer into Si daughter stamp by RIE. 50

Figure 4.1: Schematics of overall anti-dots array fabrication and Co/Pd multilayer structure. 57

Figure 4.2: Schematic illustration of the overall NiNWs synthesis using S4VP-guided AAO template.. 58

Figure 4.3: SEM micrographs of S4VP film on a Si substrate: (a) as-spun and (b) after THF-annealing for 1.5 hr. Note that images were taken after samples were immersed in ethanol during 30 min for the P4VP phase to swell so as to form a porous structure. 60

Figure 4.4: Structural evolution of S4VP thin film with respect to annealing time in THF vapor. 61

Figure 4.5: SEM micrographs of S4VP assisted Si nanopore formation: (a) tilted view after partially removing Cr coated S4VP film to reveal the Si layer (b) cross-sectional view of Si hole depth for two different RIE times, 1 minute (left image) and 2 minutes (right image). 62

Figure 4.6: SEM micrographs of pattern transferred Si nanoholes vs RIE time: (a) 1 min, (b) 2 min, and (c) 3 min. Each pore is enlarged and eventually meet with adjacent pores as RIE time is increased. Contrast difference near interpore areas in (c) corresponds to height difference from the original Si surface due to extended RIE time which leads to an undercut profile of pore geometry and Si erosion. 63

Figure 4.7: THF-annealed nanoporous S4VP film on Al thin film. Sample was immersed into ethanol for 20 min to develop porous structure. 65

Figure 4.8: SEM micrographs of S4VP film after RIE process: (a) RIE I: Residual P4VP etching located bottom of the pores. Bright spots reveal Al underneath porous S4VP film (b) RIE II: Selective Al etching exposed to the surface. Dark spots inside bright rims reveal bare Al indents created by RIE process. 65

Figure 4.9: SEM micrographs of S4VP-guided AAO: (a) top and (b) tilted view. A specimen was anodized in 8M sulfuric acid under constant voltage of 19.4V..... 66

Figure 4.10: Cross-sectional images of $(Co/Pd)_4$ magnetic multilayer deposited on Si nanohole arrays corresponding to Figure 4.6 (a), (b) and (c), respectively (1, 2, and

3 minutes RIE from left to right), showing that most of the magnetic materials are well-deposited on Si surface. 68

Figure 4.11: Magnetic hysteresis data measured (a) normal to and (b) parallel to the sample surface. A, B, and C correspond to samples shown in Figure 4.10 (1, 2, and 3 minutes RIE from left to right), respectively. 69

Figure 4.12: Electrodeposited NiNWs (a) confined into AAO nanopores and (b) liberated from AAO template removed by selective chemical etch in 1M NaOH (aq.). 72

Figure 4.13: Magnetic hysteresis loop measured out-of-plane (normal to the sample surface) and in-plane (parallel to the sample surface) direction, respectively. 73

Figure 4.14: Scheme of magnetic anti-dot structure fabrication using chemically driven metal nanodots, e.g. Au or Pt, and the representative preliminary data. 76

Figure 5.1: Typical current evolution with respect to electropolishing time. Inset shows current evolution at the initial reaction stage. A representative photograph clearly shows the mirror-like Al surface is achieved after process. 79

Figure 5.2: Schematic illustration of nanotubular AAO fabrication. (a) mild anodization to form porous AAO layer in 0.3M sulfuric acid, (b) hard anodization to form tubular AAO layer, (c) selective aluminum removal by etching in ($CuCl_2$+HCl) solution, and (d) attaching AAO upside-down on Si substrate and pore widening etch in 5wt% phosphoric acid. 81

Figure 5.3: Schematic concept of drug loading and release. (a) drug loading, (b) drug store and (c) drug release. Drug can be stored for certain amount of time or released immediately when necessary. 85

Figure 5.4: Representative anodic current changes during anodization experiments. Mild anodization (black dot line) was conducted at 25V in 0.3M sulfuric acid at 1℃, and hard anodization (red solid line) was conducted at 40V in 0.01M sulfuric acid. Mild anodization for 30 minutes led to the porous AAO structure which was used as the basis to start the subsequent hard anodization. 86

Figure 5.5: SEM images showing; (a) Top view of upside down barrier layer for the porous AAO after mild anodization with 0.3M sulfuric acid at 25V, (b) Porous structure after the barrier layer is removed, (c) Top view of upside down tubular AAO right after hard anodized at 0.01M sulfuric acid 40V. (d) Top view SEM after the nanotube tip is etched away and the tubular geometry is realized. The schematics for porous AAO formation mechanism is presented on the left of image (b) while the mechanism of nanotube formation is illustrated by the schematics on the right side of image (d). 87

Figure 5.6: SEM image of free standing AAO nanotubes placed on Si substrate (after removal of Al substrate), (a) low and (b) high magnification, respectively. Some of the loose nanotubes indicate mechanical robustness as they can be bent without fracture. 90

Figure 5.7: Oblique view SEM image of vertically aligned periodic AAO nanotubes. (a) Low magnification image, (b) high magnification image showing the nanotube and hole dimension, (c) cross-sectional SEM showing the aligned nature of the AAO nanotubes and an example bent (mechanically flexible) behavior of a separated individual alumina nanotube. Highly ordered hexagonal arrangement was obtained by hard anodization (at 40V with 0.01M sulfuric acid), followed by chemical etching in 5 wt% phosphoric acid. 91

Figure 5.8: Osteoblast (bone) cell viability determined by FDA (live fluorescent staining, green color) after 24 hours of culture time (a) on flat Al_2O_3 and (b) on Al_2O_3 nanotubes. Clearly, the cell adhesion/spreading are significantly enhanced on the nanotube surface. (c) Oblique view SEM image of vertically aligned highly periodic AAO nanotubes for cell culture. 95

Figure 5.9: Top row: bottom view, cross-sectional view, and oblique angle (inset) SEM images of AAO nanostructures used as drug carriers showing a vertically aligned, periodic nanotube films. Bottom row: Chart describing the details of the physical dimensions of the nanotube films. Note that values in the asterisk is the distance of center to center hole, center hole to surrounding void distance, void-to-void distance, respectively. 96

Figure 5.10: Absolute release rates of amoxicillin as a function of sampling time for the AAO nanotube drug carriers. The initial burst of drug from the surface is shown in the inset. The graphs show the mean ± SE (n=3). 99

Figure 5.11: (a) Accumulative amoxicillin released as a function of time and (b) release rate per day vs. time. The graph shows mean ± SE (n=3). In (a), the dotted line reveals the daily accumulation over time and the bars represent the average accumulation per week. In (b), release rate is normalized per weekly time point.

Figure 5.12: Plot of fractional release versus the square root of time representing a near perfect linear fit ($y = 0.154x + 0.092$, $R^2 = 0.998$) 101

Figure 5.13: SEM images of vertically aligned periodic AAO nanotubes. (a) As hard-anodized, tip-closed nanotube geometry, (b) After chemical etching to open the nanotube tip, (c) After additional Cr sputter deposition to intentionally re-close the nanotube entrance. An intermediate, partially blocked nanotube structure is obtained if the sputtering time is reduced 103

LIST OF TABLES

Table 2.1: Characteristics of mild anodization vs. hard anodization in 0.3M oxalic acid ($C_2H_4O_2$) at 1℃. 20

Table 3.1: Number of periodic pores in a single hexagonal cell before and after anodization in each case. 36

ACKNOWLEDGEMENTS

First and foremost, I wish to acknowledge and deeply thank my advisor, Professor Sungho Jin for his steadfast encouragement, guidance, and support during the course of this research here at University of California, San Diego. I sincerely thank to my dissertation committee members for their precious time and helpful suggestions: Professor Yu-Hwa Lo, Professor Vlado Lubarda, Professor Yu Qiao, and Professor Jennifer Cha. I also would like to thank Professor Sang-Im Yoo for implanting his tireless passion, enthusiasm, and endeavor for academic research in my mind while I was earning an M.S. degree in Seoul National University in Korea.

I wish to express my gratefulness to the JIN Group members for their numerous help, stimulating discussions, and invaluable contributions, especially Dr. Chulmin Choi, Dr. Karla Brammer, Hyunsu Kim, Young Oh, Christine Frandsen, Dr. Li-Han Chen and Duyoung Choi. Also, I wish to thank the former JIN Group members, especially Dr. Seunghan Oh, Dr. Daehoon Hong, Dr. Andrew Gapin, Dr. Jeongwon Park and Dr. Jin-Yeol Kim for showing me the way of research. I appreciate all the helps from my collaborators. In retrospect, it was a hardship, hence pleasure, to face numerous tangled problems and unravel a complicated problem one by one. Priceless memories shared with each of you will be in my heart for the rest of my life.

I would like to recognize and thank Charlotte Lauve and Betty Manoulian for the administrative paperwork, invaluable advice and informative seminar notices. I also wish to thank Nano3 staffs: Sean Parks, Larry Grissom, Ryan Anderson, Dr. Maribel

Montero, Dr. Xuekun Lu, and Dr. Bernd Fruhberger for helping with the fabrication process.

I would like to thank Korean seniors and juniors in UC, San Diego and their family for helping me in the aspects of not only various academic matters but also everyday life in San Diego. It was my great pleasure to share memories with each of you, especially Yong Sung Hwang, Dr. Soonkook Hong, Dr. Sung Hwan Cho, Dr. Sunghoon Park, Dr. Ji-Ho Park, and Dr. Sungsik Hur.

Finally, I wish to thank my dear family members for their cares, supports, and sacrifices shown not only through the course of this time but also the moment I am not recognized. Last but not least, I wish to express my infinite gratitude to my beloved wife, Youngsoon Kim and my lovely sons, Matthew and Mark for sharing all sorts of emotions. Their truly support and encouragement have been always fueled me up whenever I am tired, frustrated, and exhausted. Without their endless love and sacrifice, nothing would have been accomplished.

Chapter 2, in full, has been prepared for review publication in NANO written by Kunbae Noh, Karla Brammer, Tae-Yeon Seong, and Sungho Jin.

Chapter 3, in full, is a reprint of the material as it appears in Journal of Vacuum Science and Technology B, 28(6), C6M88 (2010) written by Kunbae Noh, Chulmin Choi, Jin-Yeol Kim, Young Oh, Karla Brammer, Mariana Loya, and Sungho Jin. The dissertation author was the primary investigator and author of this work.

Chapter 4, in full, is a reprint of the material as it was submitted for publication in IEEE Transactions on Magnetics written by Kunbae Noh, Chulmin Choi, Hyunsu Kim, Young Oh, Jin-Yeol Kim, Daehoon Hong, Li-Han Chen and Sungho Jin; and, in

part, has been prepared for publication in Journal of Vacuum Science and Technology B written by Kunbae Noh, Chulmin Choi, Hyunsu Kim, Young Oh, Jin-Yeol Kim, Se-Yeon Jung, Tae-Yeon Seong and Sungho Jin. The dissertation author was the primary investigator and author of both these papers.

Chapter 5, in full, is a reprint of the material as it appears in Journal of Materials Research, 26(2), 186 (2011) written by Kunbae Noh, Karla S. Brammer, Hyunsu Kim, Se-Yeon Jung, Tae-Yeon Seong, and Sungho Jin; and as it was accepted for publication in Journal of Biomaterials and Nanobiotechnology written by Kunbae Noh, Karla S. Brammer, Chulmin Choi, Seung Hyun Kim, Christine J. Frandsen, and Sungho Jin; and The dissertation author was the primary investigator and author of both these papers.

Lastly, I would like to show appreciation to the financial support of this research by Iwama Endowment Funding, Veeco Funding, UC Discovery/Kinamed Grant, NSF-Nanomanufacturing Division Grant, CMRR at UC San Diego, National Research Foundation (NRF) grant, AFOSR-MOST Program, CNMT Grant Frontier R&D Program, and very mostly Samsung Cheil Fellowship.

Kunbae (Kevin) Noh

La Jolla, August 2011

VITA

1976	Born in Korea
1995 ~ 1999	B.S., Materials Science and Engineering, Seoul National University, Korea
1999 ~ 2001	M.S., Materials Science and Engineering, Seoul National University, Korea
2001 ~ 2003	Military Service (R.O.K. Army), Korea
2003 ~ present	Cheil Industries, Inc, Korea
2006 ~ 2011	Ph.D., Materials Science and Engineering, University of California, San Diego, U.S.A.

PUBLICATIONS

Journals Articles:

1. Young Oh, Jin-Yeol Kim, Chulmin Choi, Daehoon Hong, Kunbae Noh, Sungdeok Kong and Sungho Jin, "Magnetic-field-guided, Microscale Partitioning of Silicon for Potential Solar Energy", (in preparation)
2. Kunbae Noh, Chulmin Choi, Hyunsu Kim, Young Oh, Jin-Yeol Kim and Sungho Jin, "Di-block Copolymer Directed Anodization of Hexagonally Ordered Porous Aluminum Oxide", Journal of Vacuum Science and Technology B (submitted)
3. Chulmin Choi, Kunbae Noh, Young Oh, Cihan Kuru, Li-Han Chen and Sungho Jin, "Geometry Controlled Periodic Si Nanopillar Arrays by Dry Oxidation and Wet Etching", Journal of Vacuum Science and Technology B (submitted)
4. Young Oh, Chulmin Choi, Kunbae Noh, Diana Villwock, Gwangmin Kwon, Haiwon Lee and Sungho Jin, "Multi-Tip AFM Lithography System for High Throughput Nano-patterning", Journal of Vacuum Science and Technology B (submitted)
5. Christine J. Frandsen, Karla S. Brammer, Kunbae Noh, Laura S. Connelly, Seunghan Oh, Li-Han Chen, and Sungho Jin, "Zirconium Oxide Nanotube Surface Prompts Increased Osteoblast Functionality and Mineralization", Materials Science and Engineering C (submitted)
6. Kunbae Noh, Karla S. Brammer, Tae-Yeon Seong and Sungho Jin, "Guided Nanostructures Using Anodized Aluminum Oxide Templates", NANO (accepted in press)
7. Kunbae Noh, Chulmin Choi, Hyunsu Kim, Young Oh, Jin-Yeol Kim, Daehoon Hong, Li-Han Chen and Sungho Jin, "Magnetic Properties of Anti-dot Patterned Co/Pd Multilayer Film", IEEE Transactions on Magnetics (accepted in press)
8. Chulmin Choi, Kunbae Noh, Young Oh, Cihan Kuru, Daehoon Hong, Li-Han Chen, Sy-Hwang Liou and Sungho Jin, "Fabrication and Magnetic Properties of Non-magnetic Ion Implanted Magnetic Recording Films for Bit Patterned Media", IEEE Transactions on Magnetics (accepted in press)
9. Chulmin Choi, Kunbae Noh, Young Oh, Cihan Kuru, Daehoon Hong, Diana Villwock, Li-Han Chen and Sungho Jin, "Diameter-reduced Islands for Nanofabrication toward Bit Patterned Magnetic Media", IEEE Transactions on Magnetics (accepted in press)
10. Hyunsu Kim, Kunbae Noh, Chulmin Choi, Jirapon Khamwannah, Diana Villwock and Sungho Jin, "Extreme Superomniphobicity of Multiwalled 8nm TiO_2 Nanotubes", Langmuir (accepted in press)
11. Kunbae Noh*, Karla S. Brammer*, Chulmin Choi, Seung Hyun Kim, Christine J. Frandsen, and Sungho Jin, "A New Nano-platform for Drug Release via

Nanotubular Aluminum Oxide", Journal of Biomaterials and Nanobiotechnology, 2011 (accepted in press) *equally contributed

12. Hyunsu Kim, Jongjin Park, Kunbae Noh, Calvin J. Gardner, Seong Deok Kong, Jongmin Kim and Sungho Jin, "X-Y Addressable Matrix Odor Generating System Using On-Off Switchable Device", Angewandte Chemie-International Edition, 50(30), 6771 (2011)
13. Kunbae Noh, Karla S. Brammer, Hyunsu Kim, Se-Yeon Jung, Tae-Yeon Seong, and Sungho Jin, "Highly Self-assembled Nanotubular Aluminum Oxide by Hard Anodization", Journal of Materials Research, 26(2), 186 (2011)
14. Karla S. Brammer, Hyunsu Kim, Kunbae Noh, Mariana Loya, Christine J. Frandsen, Li-Han Chen, Laura S. Connelly and Sungho Jin, "Highly Bioactive 8nm Hydrothermal TiO_2 Nanotubes Elicit Enhanced Bone Cell Response", Advanced Engineering Materials, 13(3), B88 (2011)
15. Kunbae Noh, Chulmin Choi, Jin-Yeol Kim, Young Oh, Karla Brammer, Mariana Loya, and Sungho Jin, "Long-Range Ordered Aluminum Oxide Nanotubes by Nanoimprint-Assisted Aluminum Film Surface Engineering", Journal of Vacuum Science and Technology B, 28(6), C6M88 (2010)
16. Jin-Yeol Kim, Kunbae Noh, Chulmin Choi, Karla S. Brammer, Mariana Loya, Li-Han Chen and Sungho Jin, "Optically Transparent Glass with Vertically Aligned Surface Al_2O_3 Nanowires Having Superhydrophobic Characteristics", NANO, 5(2), 89 (2010)
17. Chulmin Choi, Daehoon Hong, Young Oh, Kunbae Noh, Jin Yeol Kim, Leon Chen, Sy-Hwang Liou, and Sungho Jin, "Enhanced Magnetic Properties of Bit Patterned Magnetic Recording Media by Trench-Filled Nanostructure", Electronic Materials Letters, 6(3), 113 (2010)
18. Chulmin Choi, Yeoungchin Yoon, Daehoon Hong, Karla S. Brammer, Kunbae Noh, Young Oh, Seunghan Oh, Frank E. Talke and Sungho Jin, "Strongly Superhydrophobic Silicon Nanowires by Supercritical CO_2 Drying", Electronic Materials Letters, 6(2), 59 (2010)
19. Kunbae Noh, Sangdon Yang, and Sang-Im Yoo, "Control of the Composition of $Ba_{1-x}Sr_xTiO_3$ Single Crystal", Korean Journal of Crystallography, 14 (2003)

Patents / Technology disclosures:

1. Sungho Jin, Jin-Yeol Kim, Kunbae Noh, and Chulmin Choi, "Nanostructred Superhydrophobic, Superoleophobic and/or Superomniphobic Coatings, Methods for Fabrication, and Applications Thereof", U.S. Pub. No. WO2010/022107 (2010)

2. Jo Gyun Kim, Kun Bae Noh, and Yoon Kok Park, “Epoxy Resin Composition for Packaging Semiconductor Device”, U.S. Pub. No. WO2007/015591 (2007)
3. In Gui Park, Kun Bae Noh, Yeon Hee Sohn and Yoon Kok Park, “Epoxy Resin Composition for Encapsulating Semiconductor Device and Semiconductor Device Using The Same”, KR. Pub. No. 100870078 (2008)
4. Jo Gyun Kim, Kun Bae Noh and Yoon Kok Park, “Epoxy Resin Composition for Encapsulating Semiconductor Device” KR. Pub. No. 100739363 (2007)
5. Kun Bae Noh, Seong Han and Yoon Kok Park, “Epoxy Resin Composition for Encapsulating Semiconductor Device” KR. Pub. No. 100673626 (2007)
6. Kun Bae Noh, Seong Han and Yoon Kok Park, “Epoxy Resin Composition for Encapsulating Semiconductor Device”, KR. Pub. No. 100655131 (2006)
7. Jo Gyun Kim, Je Hong Ryu and Kun Bae Noh, “Epoxy Resin Composition for Encapsulating Semiconductor Device” KR. Pub. No. 100611459 (2006)
8. Jo Gyun Kim, Yoon Kok Park and Kun Bae Noh, “Epoxy Resin Composition for Encapsulating Semiconductor Device” KR. Pub. No. 100561575 (2006)
9. Kun Bae Noh, Yoon Kok Park and Jo Gyun Kim, “Epoxy Resin Composition for Packaging Semiconductor Device” KR. Pub. No. 100561569 (2006)

Conference proceedings:

1. Kunbae Noh, Chulmin Choi, Hyunsu Kim, Young Oh, Jin-Yeol Kim and Sungho Jin, “Di-block Copolymer Directed Anodization of Hexagonally Ordered Porous Aluminum Oxide”, International conference on Electron, Ion, and Photon Beam Technology and Nanofabrication, Las Vegas, U.S.A. (Jun. 2011)
2. Chulmin Choi, Kunbae Noh, Young Oh, Cihan Kuru, Li-Han Chen and Sungho Jin, “Geometry Controlled Periodic Si Nanopillar Arrays by Dry Oxidation and Wet Etching", International conference on Electron, Ion, and Photon Beam Technology and Nanofabrication, Las Vegas, U.S.A. (Jun. 2011)
3. Young Oh, Chulmin Choi, Kunbae Noh, Diana Villwock, Gwangmin Kwon, Haiwaon Lee and Sungho Jin, "Multi-Tip AFM Lithography System for High Throughput Nano-patterning", International conference on Electron, Ion, and Photon Beam Technology and Nanofabrication, Las Vegas, U.S.A. (Jun. 2011)
4. Kunbae Noh, Chulmin Choi, Hyunsu Kim, Young Oh, Jin-Yeol Kim, Li-Han Chen and Sungho Jin, “Magnetic Properties of Anti-dot Patterned Co/Pd Multilayer Film”, IEEE International Magnetics Conference, Taipei, Taiwan (Apr. 2011)

5. Chulmin Choi, Kunbae Noh, Young Oh, Cihan Kuru, Daehoon Hong, Diana Villwock, Li-Han Chen and Sungho Jin, "Diameter-reduced Islands for Nanofabrication toward Bit Patterned Magnetic Media", IEEE International Magnetics Conference, Taipei, Taiwan (Apr. 2011)
6. Chulmin Choi, Kunbae Noh, Young Oh, Cihan Kuru, Daehoon Hong, Li-Han Chen, Sy-Hwang Liou and Sungho Jin, "Fabrication and Magnetic Properties of Non-magnetic Ion Implanted Magnetic Recording Films for Bit Patterned Media", IEEE International Magnetics Conference, Taipei, Taiwan (Apr. 2011)
7. Christine Frandsen, Karla Brammer, Kunbae Noh, and Sungho Jin, "Enhanced Bone Cell Response on Zirconium Oxide Nanotube Surface", The Minerals, Metals and Materials Society, San Diego, U.S.A. (Mar. 2011)
8. Kunbae Noh, Chulmin Choi, Karla S. Brammer, Jin-Yeol Kim, Young Oh, Mariana C. Loya, and Sungho Jin, "Long-Range Ordered Aluminum Oxide Nanotubes by Nanoimprint-Assisted Aluminum Film Surface Engineering", The 54th international conference on EIPBN 2010, Anchorage, AK, U.S.A. (Jun. 2010)
9. Kunbae Noh and Sungho Jin, "Guided Anodization for Long-range, Periodically Ordered Oxide Nanotubes.", Materials Research Society, MRS Spring Meeting, Symposium LL, San Francisco, CA, U.S.A. (invited) (Apr. 2010)
10. Kunbae Noh, Chulmin Choi, Jin-Yeol Kim, Mariana Loya, and Sungho Jin, "Long-Range Ordered Aluminum Oxide Nanotubes by Guided Anodization", Materials Research Society, MRS Fall Meeting, Symposium KK, Boston, MA, U.S.A. (Dec. 2009)
11. Jin-Yeol Kim, Kunbae Noh, Chulmin Choi, Mariana Loya, and Sungho Jin, "Non-wettable Surface Created from Alumina Nanowire Arrays", US-Korea Conference, North Carolina, U.S.A. (Jul. 2009)
12. Kunbae Noh, Chulmin Choi, Karla Brammer, Jin-Yeol Kim, Young Oh, Mariana Loya, and Sungho Jin, "Long-Range Ordered Aluminum Oxide Nanotubes by Nanoimprint-Assisted Aluminum Film Surface Engineering" 10^{th} All Grad Research Symposium, UCSD, U.S.A. (Feb. 2010)
13. Kunbae Noh, Chansoo Kim, and Sang-Im Yoo, "Crystal Growth of High-Quality $BaTiO_3$ Single Crystals" 4th CMR Workshop, SNU, Korea (Feb. 2000)
14. Kunbae Noh and Sang-Im Yoo, "Compositional control of $(Ba_{1-x}Sr_x)TiO_3$ (x=0, 0.4, 0.6) Single Crystals", The Korean Ceramic Society, Gangwon university, Korea (Oct. 2000)
15. Kunbae Noh and Sang-Im Yoo, "Dielectric Properties of $(Ba_{1-x}Sr_x)TiO_3$ (x=0, 0.4, 0.6) Single Crystals", 1st Korea-Japan Symposium on Strongly Correlated Electron Systems, SNU, Korea (Oct. 2000)

ABSTRACT OF THE DISSERTATION

Preparations, Properties, and Applications of Periodic Nano Arrays using Anodized Aluminum Oxide and Di-block Copolymer

by

Kunbae Noh

Doctor of Philosophy in Materials Science and Engineering

University of California, San Diego, 2011

Professor Sungho Jin, Chair

Self-ordered arrangements observed in various materials systems such as anodic aluminum oxide, polystyrene nanoparticles, and block copolymer are of great interest in terms of providing new opportunities in nanofabrication field where lithographic techniques are broadly used in general. Investigations on self-assembled nano arrays to understand how to obtain periodic nano arrays in an efficient yet inexpensive way, and how to realize advanced material and device systems thereof, can lead to significant impacts on science and technology for many forefront device applications.

In this thesis, various aspects of periodic nano-arrays have been discussed including novel preparations, properties and applications of anodized aluminum oxide (AAO) and PS-b-P4VP (S4VP) di-block copolymer self-assembly.

First, long-range ordered AAO arrays have been demonstrated. Nanoimprint lithography (NIL) process allowed a faithful pattern transfer of the imprint mold pattern

onto Al thin film, and interesting self-healing and pattern tripling phenomena were observed, which could be applicable towards fabrication of the NIL master mold having highly dense pattern over large area, useful for fabrication of a large-area substrate for predictable positioning of arrayed devices.

Second, S4VP diblock copolymer self-assembly and S4VP directed AAO self-assembly have been demonstrated in the Al thin film on Si substrate. Such a novel combination of two dissimilar self-assembly techniques demonstrated a potential as a versatile tool for nanopatterning formation on a Si substrate, capable of being integrated into Si process technology. As exemplary applications, vertically aligned Ni nanowires have been synthesized into an S4VP-guided AAO membrane on a Si substrate in addition to anti-dot structured $[Co/Pd]_n$ magnetic multilayer using S4VP self assembly.

Third, a highly hexagonally ordered, vertically parallel aluminum oxide nanotube array was successfully fabricated via hard anodization technique. The Al_2O_3 nanotube arrays so fabricated exhibit a uniform and reproducible dimension, and a quite high aspect ratio of greater than ~1,000. Such high-aspect-ratio, mechanically robust, large-surface-area nanotube array structure can be useful for many technical applications. As a potential application in biomedical research, drug storage/controlled drug release from such AAO nanotubes was investigated, and the advantageous potential of using AAO nanotubes for biological implant surface coatings alternative to TiO_2 nanotubes has been discussed.

CHAPTER 1: Introduction

From a materials science and engineering point of view, aluminum oxide is one of the most widely used ceramic materials due to superior properties such as high thermal conductivity, high dielectric constant, high mechanical strength and high thermal stability. Moreover, the beneficial effect of thin protective alumina film naturally formed on Al surface inspired academic investigation and industrial efforts on anodic aluminum oxide in various aspects.[1-5] However, it has not been paid great attention as to potential nanotechnology applications until Masuda and Fukuda demonstrated ordered a nanoscale, vertically aligned anodic aluminum oxide (AAO) pore array by using so-called two step anodization,[6] along with Martin's pioneering work on a membrane-based synthetic approach using nanomaterials.[7] Since then, self-ordered AAO approach has been popular for broad applications in the reduced dimensional systems such as nanodots, nanowires, nanotubes and so on. Similarly to other self-ordered approaches, e.g. polystyrene particles monolayer and di-block copolymer, self-ordered nature of AAO is promising since process is simple and easy, inexpensive and allows a parallel processing (for high throughput), and suitable for large area patterning which is not always possible in other nano-patterning lithography. In addition, a pore array with high aspect ratio (the ratio of AAO film thickness to pore diameter) highlights its uniqueness as a nanotemplate for useful one-dimensional nanowire array synthesis.

In this thesis work, we have developed novel nanofabrication techniques for periodic arrays using self-assembled AAO and block copolymer (BCP). Various

applications including high density magnetic recording media and biomedical template applications have been investigated.

Chapter 1 gives a brief introduction on self-assembled nano arrays related to anodized aluminum oxide.

Chapter 2 gives broad background on Al anodization and block copolymer (BCP). Self-assembly and guided self-assembly of AAO and BCP are discussed in detail. In addition, recent development on AAO structural modification is discussed.

Chapter 3 demonstrates nanoimprint-guided AAO self-assembly on deposited Al thin film on silicon.

Chapter 4 contains fabrication and application of self-assembled BCP nanotemplate and BCP-directed AAO self-assembly.

Chapter 5 demonstrates novel nanotubular AAO structures and its biomedical applications.

Chapter 6 gives a summary of the research results achieved, discusses the ongoing research, and makes suggestions as to what additional advances need to be made in the future.

CHAPTER 2: Background

2.1 Aluminum anodization

2.1.1 Self-organized AAO

Anodizing, an electrolytic passivation process, is often used to increase natural oxide thickness on the surface of metal such as Ti, Zr, Al, Hf and other metals or alloys. Oxide formed in such a process tends to be readily dissolved preferentially in electric-field concentrated area, i.e. on the concave surface region where electric field is stronger than that in the flat or convex area. Multiple pores thus nucleate and grow at these concave sites that are initially provided by the random surface corrugation. In the same way, oxide growth is also electric-field dependent, basically assisted by field-assisted migration of anions (O^{2-}, OH^{-}) and cations (Al^{3+}), and reaction among them. The balance between the electric field enhanced oxide dissolution at the electrolyte/oxide interface and oxide formation at oxide/metal interface is essential to the formation of proper nanoporous AAO because it enables the barrier thickness to be constant over the entire anodizing process resulting from constant anodic current flow, and thus leading to a steady-state vertical pore propagation into underlying Al substrate as schematically illustrated in Figure 2.1.[4, 8, 9]

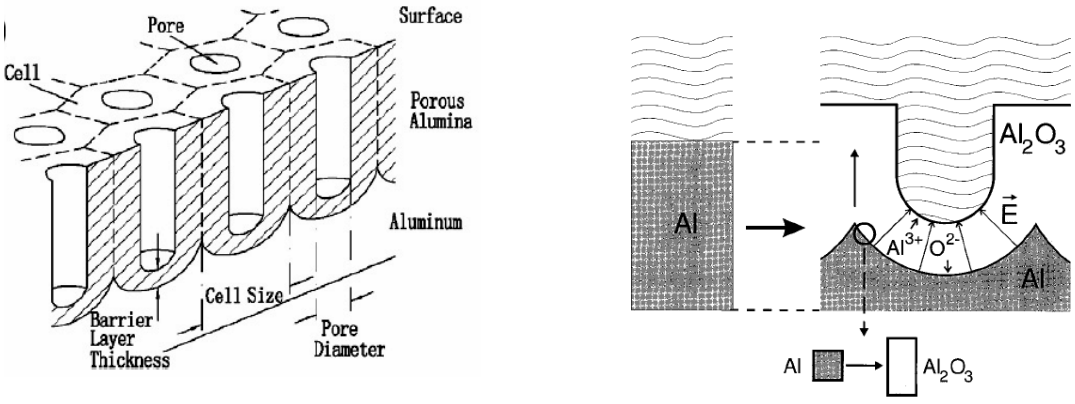


Figure 2.1: Schematic diagram of (a) porous alumina with structural parameters[10] and (b) volume expansion of Al during anodic oxidation. Existing pore walls are pushed upwards.[9]

Either bulk Al or Al thin film can be anodized in principle. However, deposited thin Al films usually have much smaller grain sizes compared with polycrystalline bulk foils, and the anodization order development is often disrupted by the randomly-distributed, densely-spaced grain boundaries from the initial stage of pore formation. As such, a high-quality growth of well ordered pore arrays on thin film aluminum has remained as one of the major challenges, especially as the pore size gets smaller toward further nano-dimensions.[11]

2.1.1.1 Self-ordering regime

It is well known that ordered porous AAO can be obtained in various processing windows.[6, 12-19] Masuda and co-workers reported ordered porous AAO in several self-ordering regimes, i.e., 25V in sulfuric acid, 40V in oxalic acid, 195V in phosphoric acid as shown in Figure 2.2. In addition, Gösele and co-workers recently reported new self-ordering regime as shown in Figure 2.3: 110~140V in malonic acid and 110~150V in oxalic acid, which drew renewed attention to hard anodization (HA) process typically associated with high anodic currents[15-19] and often leading to formation of unique nano-array structures, which will be further discussed in Chapter 2.1.3 and 2.1.4.

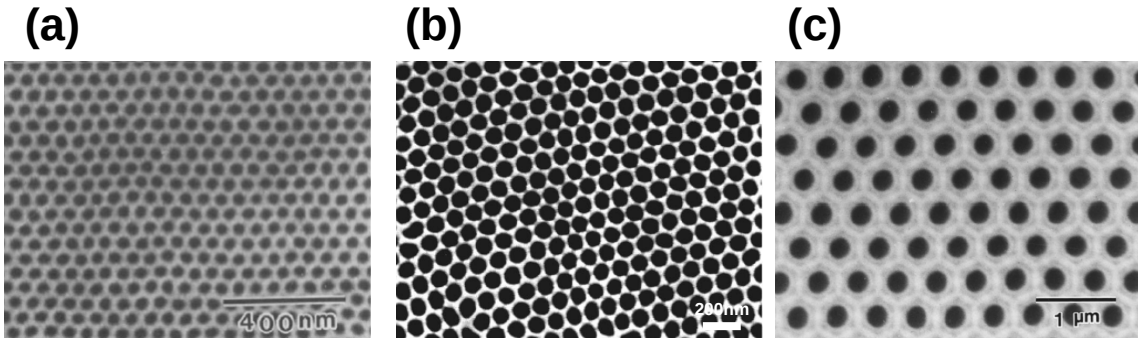


Figure 2.2: SEM micrographs of self-ordered porous AAO (mild anodization) in various dimension anodized at: (a) 25V in sulfuric acid,[12] (b) 40V in oxalic acid,[14] and (c) 195V in phosphoric acid.[13]

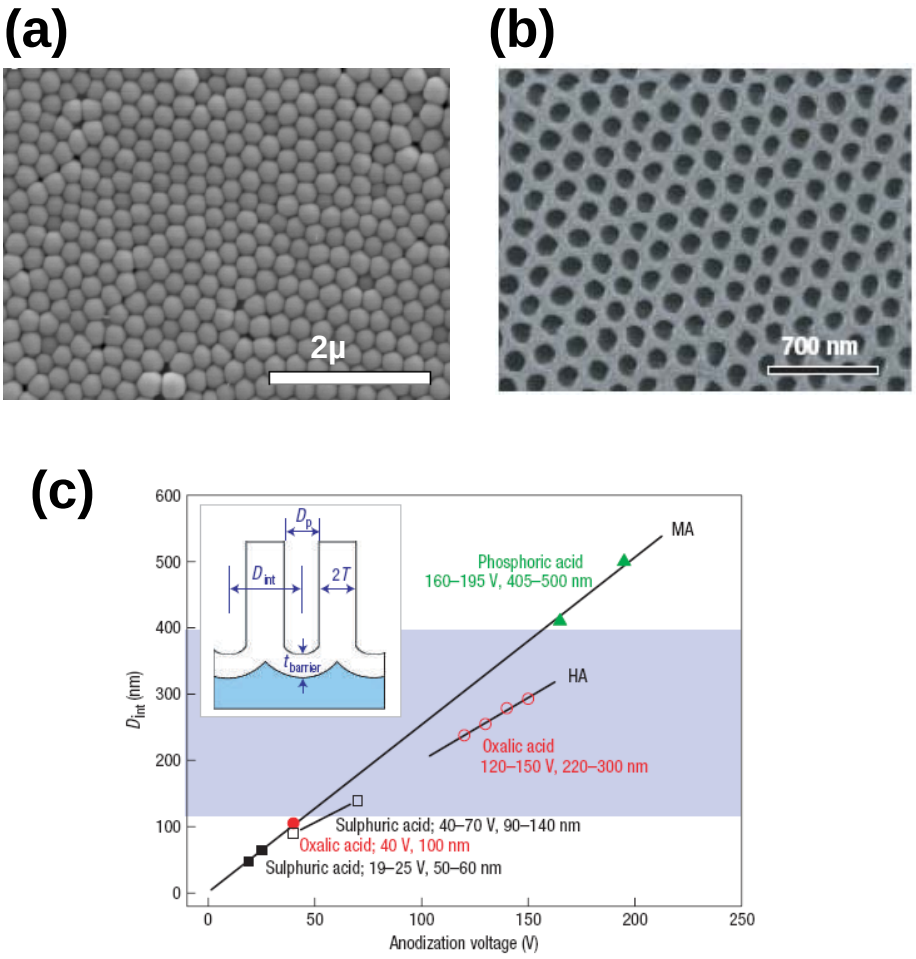


Figure 2.3: SEM micrographs of recently found self-ordered porous AAO (hard anodization) in various dimension anodized at: (a) 140V in malonic acid (barrier layer),[15] (b) 140V in oxalic acid,[16] and (c) graphical summary of self-ordering regime reported.[16]

In the case of conventional porous AAO, hexagonally ordered AAO pores are vertically grown in the underlying Al substrate under the well-known self-assembly condition as discussed above. The pore channels are straight and parallel to each other,

and the bottom of each vertical pore is closed with hemispherical end (Figure 2.3(a)) that forms continuous oxide layer over the whole anodized area, which is known as a "barrier layer".[1] Shown in Figure 2.3(c) are well-summarized self-ordering regimes of AAO reported so far.

2.1.1.2 Controlling factors for self-ordering phenomena

Most commonly cited factors for self-organized AAO are anodizing voltage, current density, species of electrolyte used and its concentration, and anodizing temperature. Since these factors are correlated each other, the role of each parameter should be taken into consideration to understand the underlying overall nanopore formation mechanism.

Applied voltage is one of the most important parameters to determine geometric AAO dimensions such as pore diameter and interpore distance (or cell size). The effect of applied voltage has been shown empirically and theoretically[1, 4] and the valid relationship between applied voltage, V_{app} and interpore distance, D_{int} or pore diameter, D_p can be expressed as:

$$D_{int} = 2.5V_{app} \tag{2-1}$$

$$D_{int} = 2\ D_p \tag{2-2}$$

This relationship is valid as long as a relatively small anodic current is evolved. However, if the high current evolves under unstable anodic process conditions such as high electrolyte concentration, elevated temperature and high applied voltage, the effect of current density should be taken into account. In addition, it is noteworthy that a pore

widening step after anodization can change pore diameter while maintaining the cell size constant.

Highly ordered AAO could be associated with high current evolution, directly related to high electric field across barrier layer near the pore bottom. The current density during anodization is dependent on various parameters and the applied electric field, i.e.,

$$j = j_0 \exp(\beta E) \tag{2-3}$$

where both j_0 and β are temperature- and material-dependent parameters and E is the effective electric field.[20] Increasing applied voltage at a given electrolyte raises effective electric field at the pore bottom, which accelerates more ionic species movement through dielectric barrier and, in turn, current flows catastrophically at those areas, thus leading to dielectric breakdown.[21] Therefore, these aspects should be taken into account especially in hard anodization, which typically involves high current flow during ordered AAO formation.

As experimentally demonstrated by Lee et al., current density, i.e. the electric field strength at the pore bottom, is an important parameter governing self-ordering phenomena, specifically in hard anodized AAO.[15, 16] They proposed that repulsive forces between oxide cells under high electric field strength, associated with high mechanical stress at the metal/oxide interface due to volume expansion, are the main driving force for the well developed self-organized formation of ordered hexagonal pore arrays.

The selection of proper electrolyte is important and oxygen element containing acids are generally under consideration for porous type AAO formation. Depending

upon pore dimension and morphology, frequently utilized electrolytes are sulfuric acid, oxalic acid, phosphoric acid and the mixed solution of these.[22] Other electrolytes such as malonic acid and citric acid were also reported.[15]

Electrolyte temperature controls not only oxide growth rate (kinetics) but also influences uniform oxide formation (morphology). As temperature decreases, growth rate decreases but more uniform oxide layer forms. To reduce Joule heating owing to large current evolution specifically under hard anodization, negative temperature below 0℃ with ethanol addition in aqueous electrolyte is often used for efficient heat dissipation, since the freezing point of ethanol is lower than that of water so that aqueous electrolyte can be cooled down somewhat below 0℃. Moreover, latent heat dissipation occurred when ethanol evaporates further preventing or minimizing local event which otherwise would be often encountered in HA. Therefore, it is important to determine the appropriate anodizing temperature window range to balance the growth rate and the quality of oxide film.

The porosity in AAO, generally considered as constant (10% porosity rule) in mild anodization condition regardless of electrolyte and anodizing voltage,[23] can be a factor in modified anodizing conditions in the course of releasing mechanical stress accumulated due to fast oxide growth. Moreover, stirring of the electrolyte helps AAO to be better ordered since the concentration profile along pore axis is influenced by electrolyte agitation.[24]

Also, an addition of Al-containing salts or aging of electrolyte prior to the main anodization steps might be a factor in certain process conditions as demonstrated by Chu et al. although its effectiveness is still being debated.[16, 25]

On the other hand, the effect of alloying element in pure Al is of interest for economic point of view since Al alloy is easier to obtain and cheaper than pure Al in industrial point of view. For some applications, Al alloys with other physical or chemical properties are preferred to pure Al. In these aspects, anodization of Al alloys should be also investigated further for spontaneous self-ordered AAO formation.

2.1.2 Guided AAO self-assembly

In addition to self-organized AAO template, numerous research approaches regarding anodization on periodically corrugated Al surface have been explored to achieve ideal pore arrangement, which is referred to as guided or directed anodization. Towards this end, various technological means have been utilized to create certain pre-patterns directly on bulk Al or resist-coated Al surface. Depending upon the pre-patterning mechanism utilized, patterns can be formed one by one (serial) or all at once (parallel). As would be expected, parallel patterning has some advantages over serial patterning process in terms of high throughtput and cost-effectiveness. In this chapter, nanoimprint lithography (NIL)-assisted guided assembly will be focused.

2.1.2.1 Serial guiding process

Conventional patterning techniques to utilize electron, ion, and photon beams have been extensively utilized along with the development of silicon technology. Depending upon the desired pattern dimension, each of these beams can be utilized to engrave desired patterns on the substrate involved.

For the purpose of guided anodization, various experimental demonstrations of guided anodization have been made. In addition to e-beam guided AAO as shown in

Figure 2.4(a), Liu et al. used focused ion beam to create a hexagonally close-packed lattice of concaves on a polished Al surface (Figure 2.4(b)).[26] Masuda et al. demonstrated guided AAO using nano-indentation of scanning probe microscope tip although patterned area is rather small, just a few micrometers in width (Figure 2.4(c)).[27] Sun et al. demonstrated that Al film on holographically patterned silica substrate in 1D and 2D can be guided over the anodizing process (Figure 2.4(d)).[11] However, these are generally much more expensive and complex processes compared to the self-ordering AAO method.

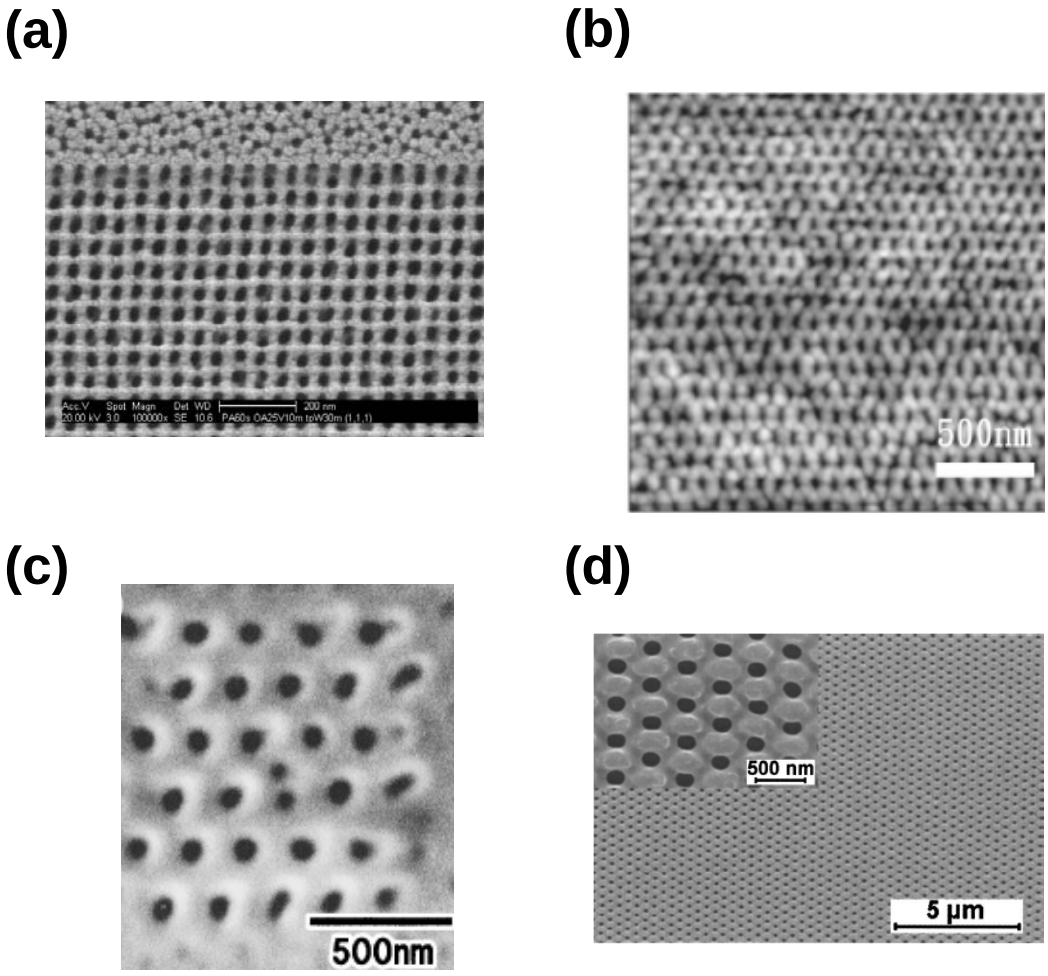


Figure 2.4 Representative SEM micrographs of serially guided anodization: (a) e-beam lithography-assisted AAO, (this work) (b) AFM image of FIB-guided AAO,[26] (c) indentation of SPM-guided AAO,[27] and (d) holographic lithography-induced AAO.[11]

2.1.2.2 Parallel guiding process

In contrast to the serial patterning technique, parallel patterning is a relatively fast, inexpensive and efficient process. Nanoimprint lithography (NIL) has been paid a particular attention by virtue of Chou's pioneering work.[28-30] As an efficient way of pre-patterning on Al surface, NIL-assisted guided anodization was first demonstrated by

Masuda et al. (Figure 2.5(a)).[31, 32] In addition, the self-repair phenomenon which repairs pores that were not only faithfully guided by pre-patterns was demonstrated, with newly formed pores at defect sites introduced upon NIL pre-patterning have been reported as shown in Figure 2.6(a).[33] Further, ordered mosaic nanocomposites were demonstrated as shown in Figure 2.6(b).[34]

In line with Masuda et al., Choi et al. reported pattern multiplication that a smaller interpore distance of AAO compared to the lattice constant of NIL mold was obtained as shown in Figure 2.5(b), which would be significant in a sense that it can lead to a useful technique to further scale down AAO pore array dimension with the same master mold used.[35, 37] If the resulting AAO array made from NIL-guided anodization can be utilized for NIL mold fabrication, the repeated imprinting and anodizing process can result in a nanotemplate with successively reduced dimensions.

In contrast to most guided anodization techniques demonstrated on bulk Al foil, pattern fabrication on Al thin film is of great interest in terms of taking advantages of mature Si technology. However, with the limited Al film thickness, spontaneous self-ordered AAO approach is not always optimized since substantial amount of Al material should be sacrificed before pores are laterally ordered, which can not be the case in the thin film processing. Therefore, a guided AAO type self-assembly should be more advantageous for the case of thin film Al. However, Al film surface roughness could negatively influence faithful pattern transfer especially when the pore size is made smaller for higher pattern density. To resolve this issue, we investigated how the thin film surface roughness could be controlled, for example, using the substrate temperature effect during the film deposition, which will be discussed in Chapter 3.

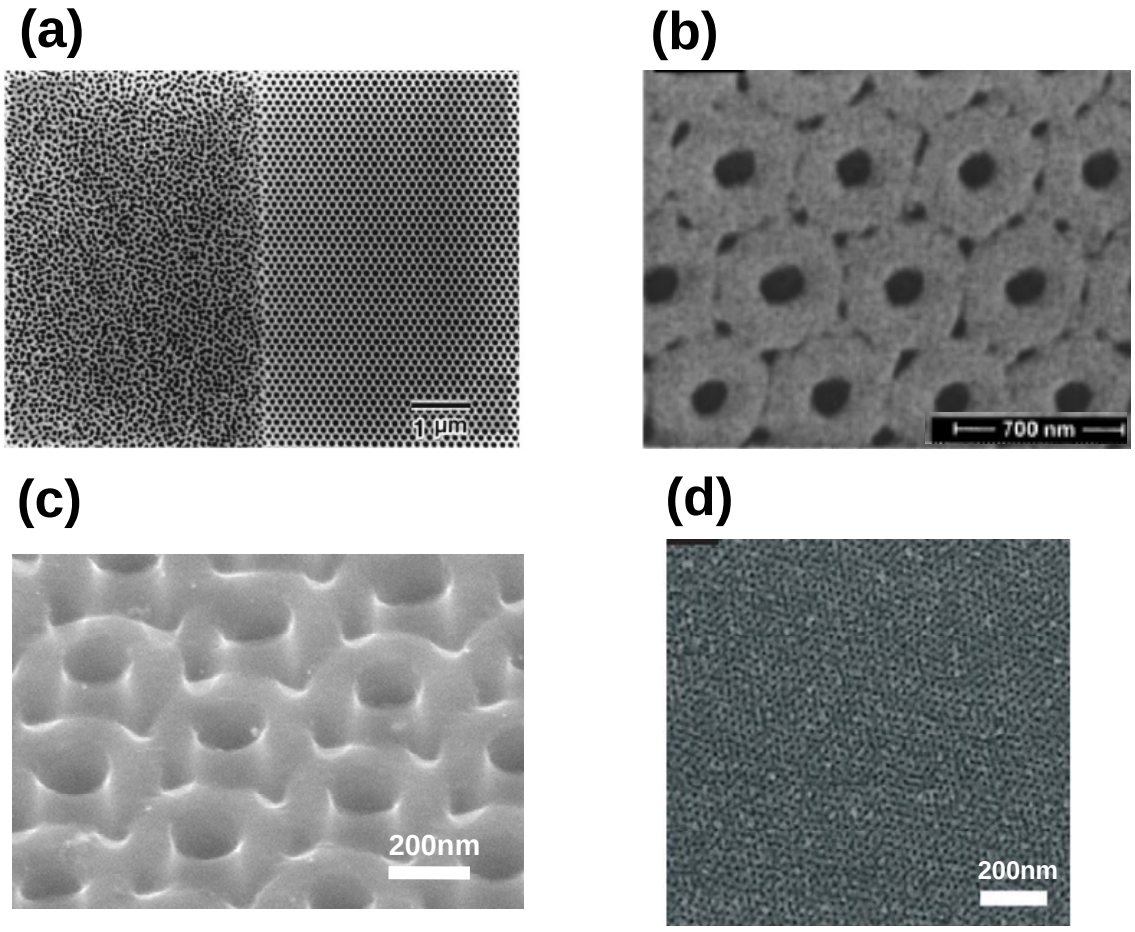


Figure 2.5: Representative SEM micrographs of parallel guided anodization: (a) self-ordered (left) and NIL-assisted AAO (right),[31] (b) NIL-assisted AAO pattern multiplication on Al foil,[35] (c) on Al thin film, (this work) and (d) NIL-assisted AAO patternPS-*b*-P4VP BCP-guided AAO.[36]

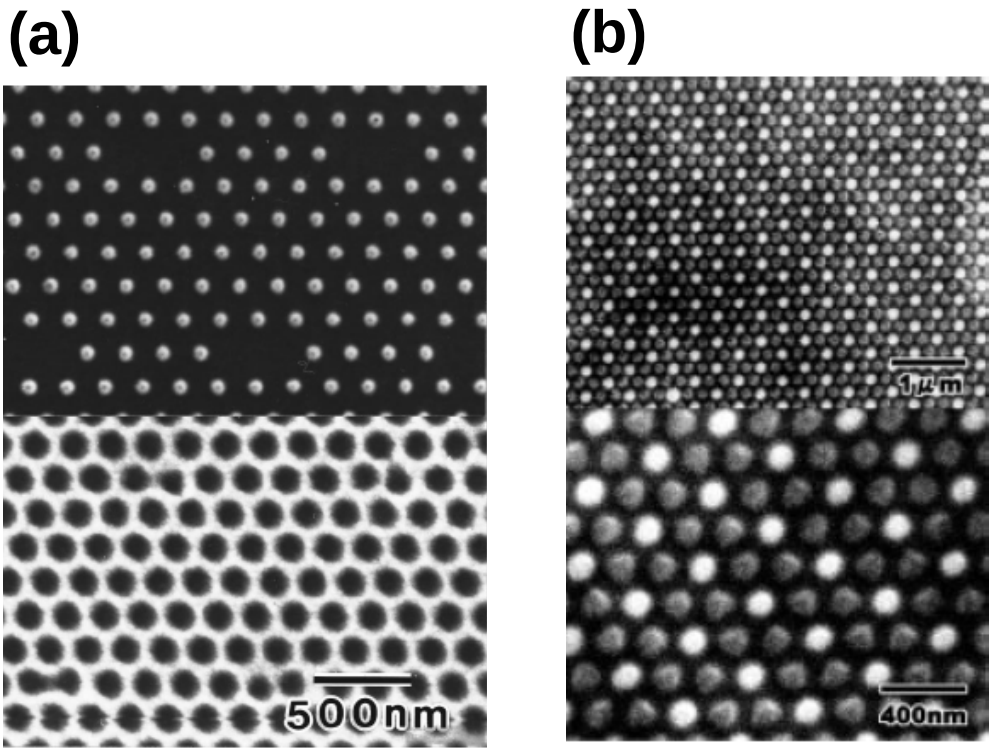


Figure 2.6: Self-repair of the pattern with periodic deficiencies: (a) SiC master mold (top) and guided AAO (bottom)[33], and (b) the mosaic composite composed of gold (bright dots) and nickel (dark dots).[34]

Another good example of parallel patterning is to use self-assembled block copolymer (BCP)[38, 39] in which two or more homopolymer subunits are linked by covalent bond to the end. Russell group demonstrated polystyrene-block-poly(4-vinylpyridine) (S4VP)-guided AAO nanopores (Figure 2.5(d))[36] and this technique can be further extended for AAO patterning if ideally ordered BCP by guided assembly is combined.

2.1.2.3 Emerging guiding process

In spite of various advantages of parallel processes mentioned above, the master mold fabrication for NIL process has been mostly made by time-consuming serial

lithographic methods, within its resolution limit. It is, therefore, highly required to develop alternative techniques to obtain the master mold. For this purpose, a single domain nanoporous AAO array is a promising route for convenient NIL daughter stamp fabrication having the reduced lattice distance resulting from pattern multiplication, which cannot be obtained from standard pattern transfer method.

On the other hand, recently developed emerging patterning techniques such as multi probe (millipede) AFM lithography[40] and parallel dip pen lithography (DPN) [41, 42] can open new parallel patterning approach to overcome drawbacks arising from inherently serial lithographic method. Successful demonstration of cutting-edge techniques will stimulate much research in both academic and practical aspects.

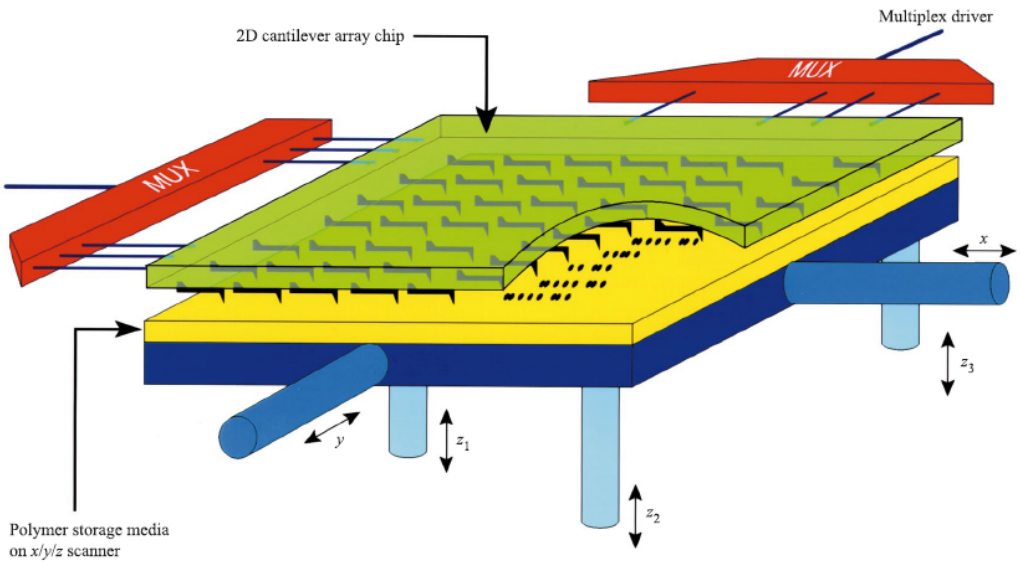


Figure 2.7: Schematic illustration of “Millipede” concept for future 2D AFM cantilever array.[40]

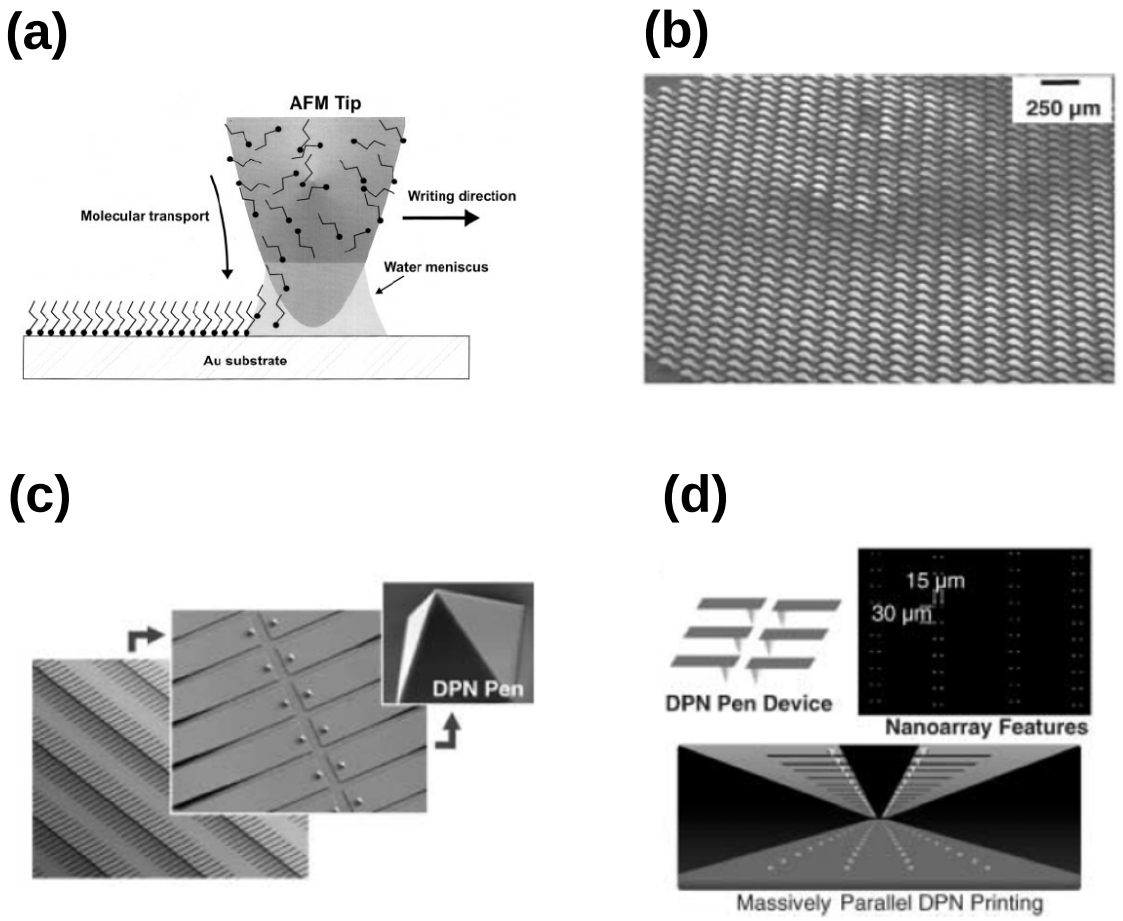


Figure 2.8: Dip-pen lithography (DPN) : (a) single DPN [41] and (b,c,d) parallel-probe DPN[42]: (b) SEM image of a high-density, 2D array of passive DPN probes, (c) SEM images of a commercial "Massively Parallel Pen" (MPP) array and (d) fluorescence micrograph of spots written with the MPP array.

2.1.3 Hard anodization

Conventional anodization, referred to as mild anodization (MA), is the anodizing process under moderate current or voltage conditions and therefore, stable anodic layer is formed over an entire anodizing process.

On the other hands, hard anodization (HA), mainly considered for corrosion-resistant coating in industrial application, has been paid little attention in nanofabrication research until highly ordered porous AAO was demonstrated by Lee et al. out of self-ordering regime[16] In general, high current evolution (and hence heat generation) during anodization readily leads to dielectric breakdown or burning[43] due to localized current flow and therefore undesirable oxide thickening in local area as discussed above. However, they successfully demonstrated highly ordered AAO under HA condition. To suppress dielectric breakdown tendency, a thin oxide layer was formed under MA condition and the subsequent HA could be carried out to enable uniform oxide film growth as shown in Figure 2.9(a). In contrast to slow and linear AAO growth rate observed in MA, significantly fast and nonlinear growth characteristics (Figure 2.9(b)) arising from nonlinear current flow (Figure 2.9(c)) during HA were observed. In addition, voltage dependence of interpore distance (D_{int}), pore diameter (D_p), and porosity (P) is rather weaker than that in MA as shown in Figure 2.9(d). These observations distinguished newly found HA from conventional MA and expanded self-ordered window regime as shown in Figure 2.3(c). The characteristic values of MA vs. HA are summarized in Table 2.1.

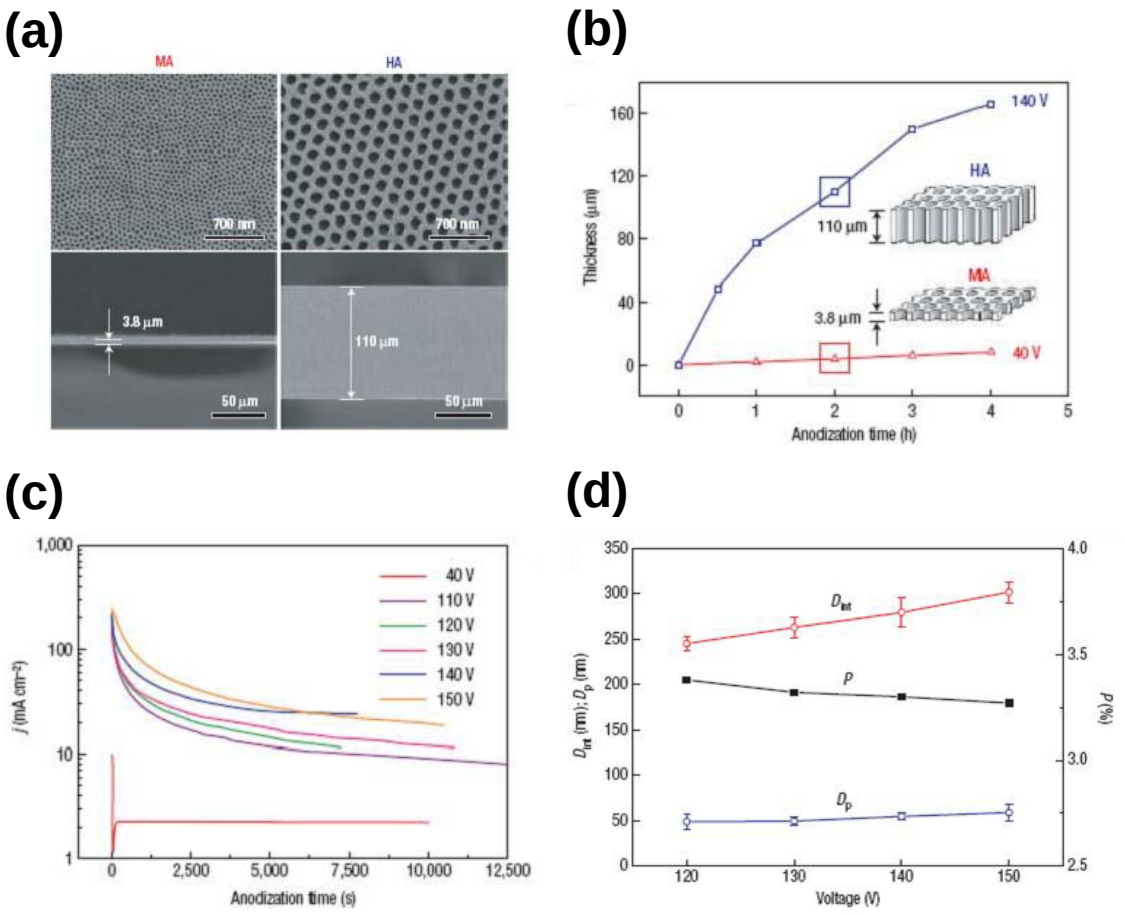


Figure 2.9: Hard anodization vs. mild anodization[16]: (a) Film thickness as a function of anodizing time of HA (blue line) and MA (red line) and (b) SEM micrographs of the corresponding AAO samples formed by MA (left column) and HA (right column) for 2 hr, respectively, (c) current-time transients during HA in 0.3M oxalic acid at 1℃ with reference transient during MA (denoted as 40V) in the same condition, and (b) the evolution of interpore distance (D_{int}), pore diameter (D_p) and porosity (P) as a function of the HA voltage.

Table 2.1: Characteristics of mild anodization vs. hard anodization in 0.3M oxalic acid ($C_2H_4O_2$) at 1℃.[16]

	MA	HA
Voltage (V)	40	110 ~ 150
Current density (mA/cm^2)	5	30 ~ 250
Film growth rate (μm/h)	2.0 (linear)	30 ~ 250 (nonlinear)
Porosity (P; %)	10	3.3 ~ 3.4
Interpore distance (D_{int} ; nm)	100	220 ~ 300
Pore diameter (D_p ; nm)	40	49 ~ 59
Pore density (ρ ; pore/cm^2)	1.0×10^{10}	$1.3 \sim 1.9 \times 10^9$
Proportionality constant (k ; nm/V)	2.5	2.0
Water content (wt%)	0.3 ~ 0.4	0.1
Carbon content (wt%)	2.4	1.8
Density (g/cm^3)	2.8	3.1

Interestingly, alternative MA and HA anodization in a different electrolyte on pre-textured Al foil lead to a composite AAO membrane with periodically modulated diameters of nanopores arising from the corresponding porosity change in MA and HA, respectively, as discussed above. Furthermore, newly derived pulsed anodization composed of relatively long MA pulse (60 ~ 180s) followed by short HA pulse (~ < 1s) in the same electrolyte was suggested not only to provide continuous structural engineering of nanoporous AAO but also to tailor pore structure and chemical composition of AAO along the pore axes as shown in Figure 2.10.[17, 18] Moreover,

periodic oscillation of pore wall thickness arising from corresponding spontaneous current oscillation was observed when bulk Al is hard anodized in sulfuric acid[19] and in oxalic acid (Figure 2.11(a)).[44]

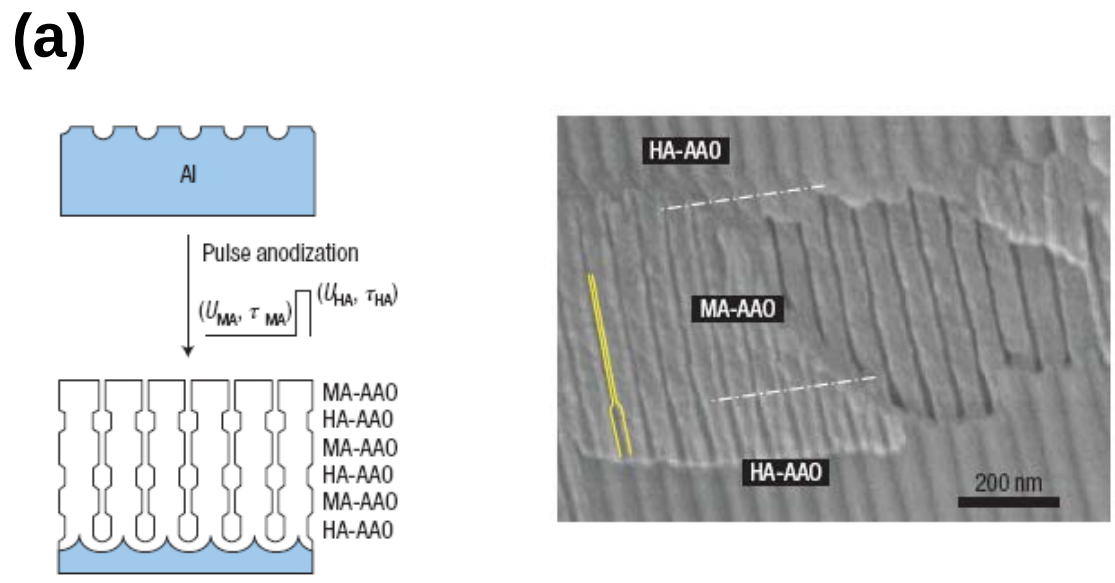


Figure 2.10: Modulation of pore diameter by pulsed anodization: (a) scheme for the fabrication of AAO with modulated pore diameters and (b) SEM micrograph representing the cross-sectional view of an as-anodized AAO.[17]

2.1.4 Modified AAO nanostructures

Shown in Figure 2.11 are the representative SEM micrographs of various structural modifications of AAO membranes. Thanks to pioneering works of Gösele group, various unique AAO nanostructures have been demonstrated and each of them opens up new opportunities for advanced device applications.

Li et al. demonstrated serrated AAO nanochannels (Figure 2.11(b))[45, 46] arising from the evolution of oxygen bubbles[47, 48] known as the origin of void creation in barrier layer. Since branched nanowires can be made cost-effectively via electrodeposition into serrated AAO pores, potential applications using unique branched nanowires can be contemplated.

In addition, Losic et al. demonstrated periodically perforated pore structure by current-controlled cyclic anodization (Figure 2.11(b)), which also led to pore wall thickness modulation and, therefore, chemical etching in diluted phosphoric acid led to the perforation of the pore side wall.[49]

On the other hand, Zhao et al. reported bimodal pore distribution characterized by six-membered ring symmetry in current-controlled condition (Figure 2.11(d)).[50] When AAO was chemically etched in the mixed $HCl/CuCl_2$ solution, generally used as selective Al etchant against AAO, six small pores located around a large pore at the center are selectively open and thus leading to unique symmetry of AAO pores.

Recently, Li et al. reported micrometer spaced anodic oxide structure obtained under ultra-high voltage HA, which has not been explored before. This is shown in Figure 2.11(e).[51] For the reason forAAO side wall thickness variation, they interpreted that $Al(OH)_3$ rapidly formed at the metal oxide interface is gathered in-between AAO cell boundary and shrink along the side surfaces when it decomposes, which results in a periodically perforated pore wall structure analogous to the morphology from current controlled cyclic anodization[49] or pulsed anodization[17]

Of particular interesting is alumina nanotube configuration reported by several groups.[17, 18, 25, 52-54] Mechanisms for nanotubular AAO formation have been extensively investigated.[17, 25, 50, 55-59] In contrast to the case of MA in which

oxygen bubbles are liberated from the AAO, some bubbles are trapped in-between pore walls so that voids are often observed at the triple cell junctions especially after the hard anodization in which high current flows over the entire anodizing duration. Accumulated pressure in the voids are large due to their nanoscopic sizes[60] and act as repulsive force to separate AAO cells away from each other and, thus, the existence of voids along cell boundaries plays an important role in separation of neighboring AAO nanotubes when mechanical force is applied. In addition, interconnected void channels along AAO cell boundaries allow chemical etching solution e.g. diluted phosphoric acid or mixed $CuCl_2$/HCl to wet the boundary area which makes it possible to further separate AAO cell, thus leading to vertically aligned AAO nanotubes as shown in Figure 2.11(f).

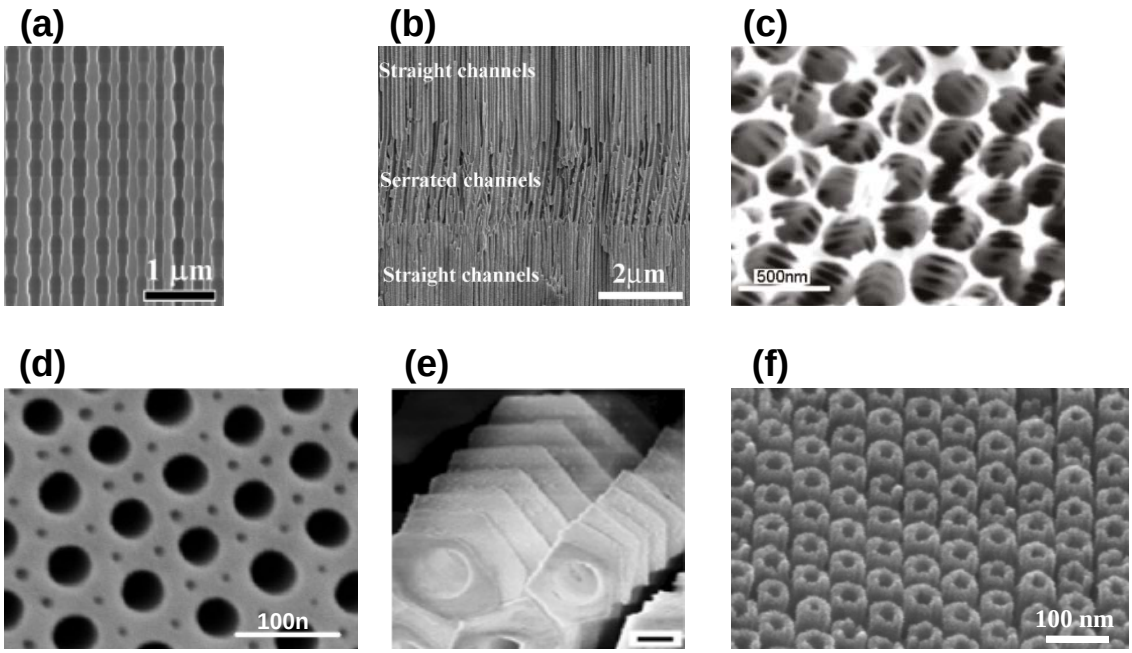


Figure 2.11: Various nanostructures derived from modified anodization techniques. (a) pore wall oscillation by spontaneous current oscillation,[44] (b) serrated pore channel,[45] (c) perforated pore wall by cyclic anodization,[49] (d) bimodal pore distribution by constant current anodization,[50] (e) hollow structured pore arrangement by ultra-high voltage anodization,[51] and (f) arrayed AAO nanotubes by constant voltage anodization (this work).

2.2 Block copolymer

Block copolymers (BCPs) comprise two or more homopolymer subunits linked by covalent bonds. The most important applications of block copolymers are based on the thermoplastic elasticity created by microphase separation in triblocks and multiblocks and the surfactant-like behavior of diblocks and graft blocks when blended with homopolymers.

The phase behavior of BCP is primarily determined by the following parameters: the overall degree of polymerization *N,* the magnitude of the Flory-Huggins

segment-segment interaction parameter χ, the volume fraction of type-A repeat units f, and combined parameter χN, which controls the degree of segregation.[61]

Order-disorder transition occurs depending upon χN product, as shown in Figure 2.12.[62] For χN <<10, entropic factors dominate and diblock copolymers exist in a spatially homogeneous state.[63] Increasing N or χ shifts the free energy balance and leads to the development of local composition fluctuations[64] as depicted in Figure 2.12. When χN = 10, a delicate balance exists between entropic and energetic effects. Increasing this parameter further induces a first-order transition to an ordered state.[63, 64] In the limit χN >>10, energetic factors dominate and the ordered microstructures are characterized by narrow interfaces and nearly flat composition profiles.

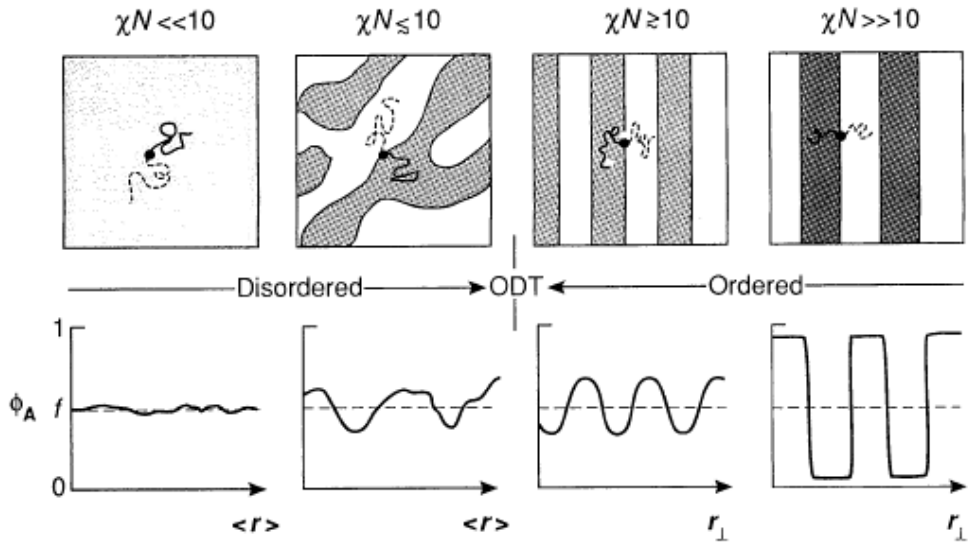


Figure 2.12: Evolution of structure with the combined parameter χN for a symmetric, di-block copolymer with f = 0.5. When χN ~ 10, small variations in system entropy (~ N^{-1}) or energy (~χ) leads to ordered ($\chi N \geq 10$) or disordered ($\chi N \leq 10$) states. A homogeneous composition profile (Φ_A vs r) results when entropic factors dominate (χN << 10), whereas a strongly microphase segregated pattern characterizes the limit where energetic factors prevail (χN >> 10).[62]

2.2.1 Self-organized BCP

For the fabrication of devices on the nanometer scale, self-organized macromolecular materials can provide an alternative pathway to conventional lithography. When necessary conditions for ordered phase segregation are met, BCPs spontaneously phase segregate and self-assemble into microphase-separated, nanometer-sized domains that exhibit ordered morphologies at equilibrium.[61, 62] The relative chain lengths of the blocks determine the corresponding BCP morphology and commonly encountered ordered morphologies in bulk samples are periodic arrangements of lamellae, cylinders, and spheres. The chains can self-assemble to form micrometer-scale domains whose size and geometry depend on the molecular weights of the types of polymer and their interaction.

One of the advantageous features of the BCP thin films is that they spontaneously form nanometer-scale patterns over a large area (albeit with some microdomain boundaries unless guiding and anchoring mechanisms are utilized), which is desirable for the applications requiring high throughput manufacturing.

2.2.2 Directed BCP

The self-ordered BCP film provides highly ordered pore arrays; however, micrometer-sized domain boundaries are present, which is not desirable for applications such as patterned magnetic media where perfectly arranged patterns are required to function properly. In this regard, considerable attention has been paid to lithographically directed BCP self-assembly for the realization of long-range ordered nano arrays. These directed processing offers several advantages such as cost-effectiveness, large area coverage and high throughput that stems from the inherent

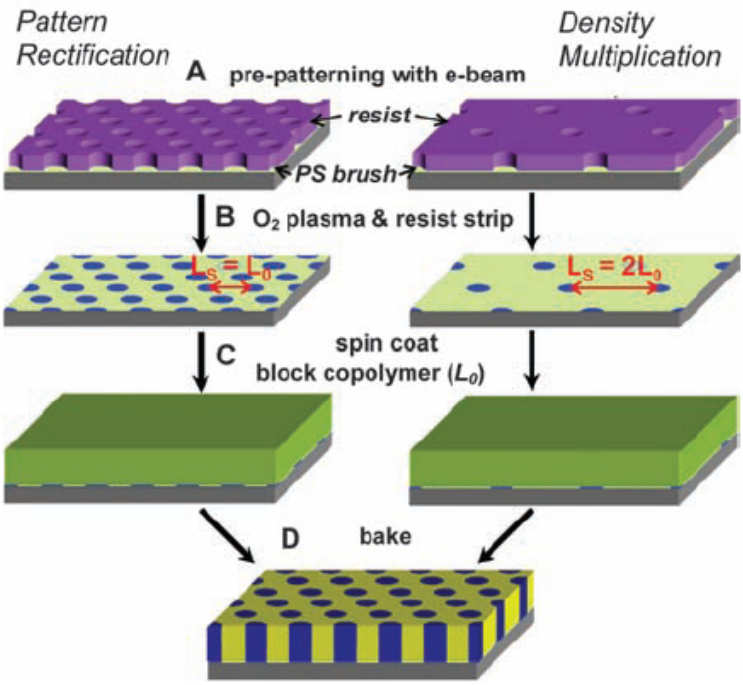
parallel patterning nature of self-assembly in addition to its compatibility with pre-established top-down patterning technologies. Nevertheless, the pre-patterning method is an extra step that introduces a lithographic step, nominally at the same feature density as that achieved by the block copolymer.

Recently, Ruiz et al. reported successful demonstration of directed BCP self-assembly with advantageous features of both pattern rectification and multiplication on substrate pre-patterned by e-beam lithography as shown in Figure 2.13.[65] They claimed that nonuniform e-beam patterns could be further improved in terms of pattern uniformity as shown in Figure 2.13(b) (E, G) and, furthermore, sparsely defined e-beam patterns acted as anchors for the subsequent BCP pattern orientation, thus leading to increased pattern density and dimensional uniformity over large area.

On the other hand, Park et al. found macroscopic ordering of PS-b-PEO self-assembly on a faceted sapphire substrate as shown in Figure 2.14.[66] They used surface reconstructed sapphire single crystal as a substrate formed upon heating and the successive cooling. Perfectly aligned BCP thin films were formed in a relatively various M_n values, which is advantageous for tailoring of the pattern density.

Chapter 2, in full, has been prepared for review publication in NANO written by Kunbae Noh, Karla Brammer, Tae-Yeon Seong, and Sungho Jin.

(a)



(b)

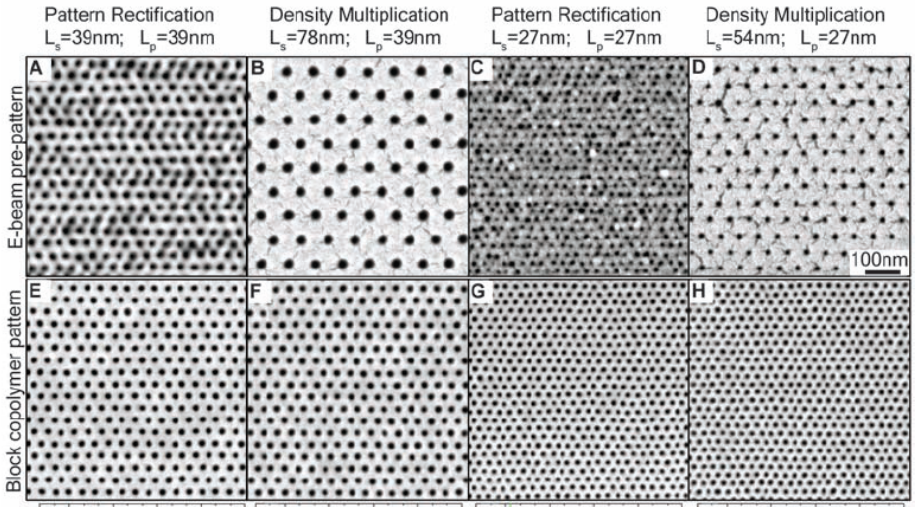


Figure 2.13: Representative guided BCP array of PS-*b*-PMMA on an e-beam patterned PS/SiO_x substrate: (a) schematic fabrication process (A-D) and SEM images of e-beam pre-patterns (E) and BCP patterns by means of density multiplication (F), and (b) SEM images of developed e-beam resist (A-D) and the block copolymer film (E-H) on top of the prepattern defined by the corresponding e-beam pattern above.[65]

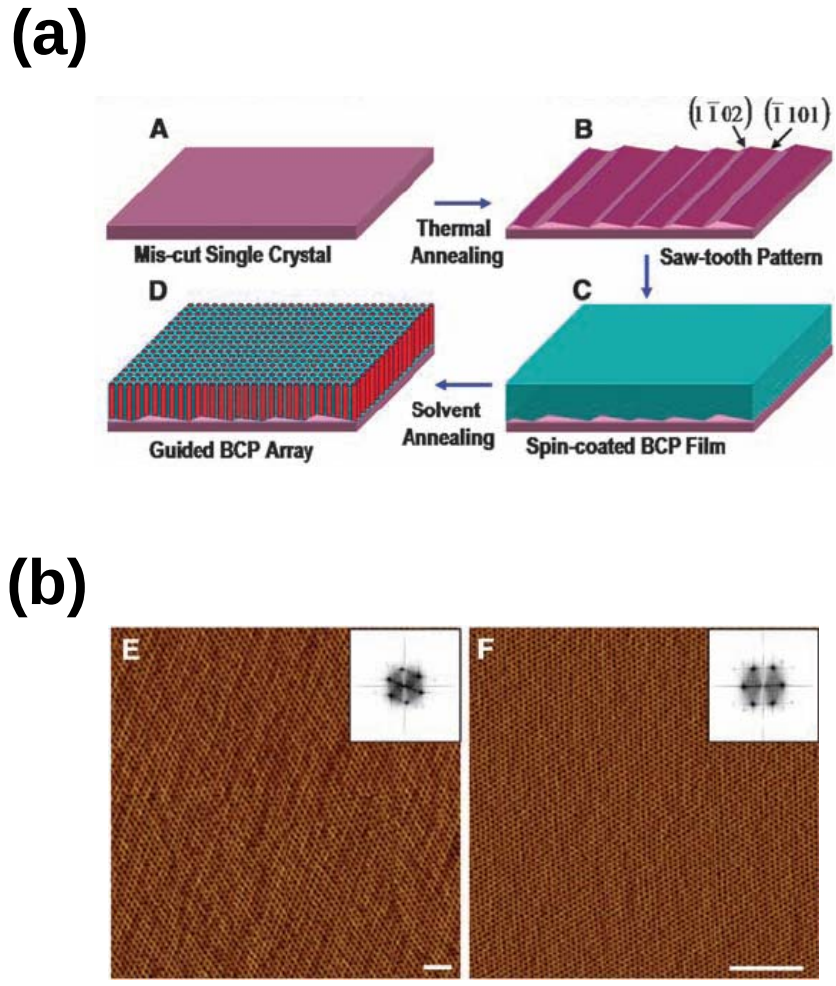


Figure 2.14: Representative guided BCP array of PS-*b*-PEO on highly oriented crystalline facets on a single crystal sapphire: (a) schematic fabrication process (A-D) and (b) AFM phase images of BCP having different M_n, (E) 25.4kg/mol and (F) 7.0kg/mol.[66]

CHAPTER 3:
Nanoimprint-guided AAO on Al thin film

3.1 Introduction

Since the discovery of Masuda and Fukuda's self-ordered anodization in 1995,[6] anodic aluminum oxide (AAO) has become one of the most popular periodic templates to create more or less periodic nanodots,[32, 67-69] nanowires[70-72] and nanobarcodes[73-75] for magnetic and electronic devices as well as for biological application such as DNA patterning.[76] In addition to self-ordered AAO template, many researches regarding anodization on pre-treated Al surface, referred to as guided anodization, has been explored to achieve ideal pore arrangement via various surface pre-patterning techniques such as focused ion-beam lithography,[26] scanning probe microscopic lithography,[27] and holographically patterned lithography.[11] These are generally expensive and complex processes compared to the self-ordering AAO method. By virtue of the invention of nanoimprint lithography (NIL),[28-30] NIL-based guided anodization on Al foil has been paid particular attention due to its relatively fast, inexpensive and efficient process, for example, demonstrated by Masuda *et al.*.[31, 77] They also found the self-repair phenomenon that missing pores can be created at defect sites and kept in harmony with guided pores, and the process was utilized to obtain ordered mosaic nanocomposites.[33, 34]

Extending this concept, Choi *et al.* reported that the interpore distance of AAO can be made smaller than the lattice constant of imprint mold, which is significant in a sense that it makes possible to scale down interpore distance of the master mold.[35, 37] Most of these reports, however, deal with bulk foil aluminum materials, and very little

guided anodization research has been conducted on Al thin films on technologically important Si substrates.[16] One of the frequently encountered issues in thin film Al deposition on a flat substrate is the formation of rough surface Al layer with substantial variation in height, which is not desirable for performing precise nano-imprinting for guided anodization. Motivation behind this study, therefore, also includes a design of experimental deposition processes for sub-nanometer-smooth Al layer. The overall aim of this study is to create a large-area, long-range ordered "periodic nano-arrays" on Si substrate by means of guided anodization together with nanoimprint technology, and to engineer nano surface morphology by controlling the chemical processes involved.

3.2 Experimental procedures

3.2.1 Al thin film deposition

Al thin films were sputter-deposited on Si substrate at a base pressure of 2×10^{-7} torr by using Nor-Cal sputter system equipped with temperature controlled stage. Argon gas pressure was maintained at 3mTorr with 24sccm gas flow rate during Al sputtering. 100W plasma power was applied and Al film deposition rate was ~1.6Å/s. For study of surface roughness control of the deposited aluminum films, the temperature of the Si substrate was varied from room temperature to cryogenic temperatures of -70℃, -90℃ and -115℃ using a cold stage within the sputtering chamber cooled by liquid nitrogen.

3.2.2 Master mold fabrication

Nanoimprint molds in this study (both hexagonal array and triangular array) were fabricated by lithography processes including deep ultraviolet (DUV)-patterning

(see Figure 3.1), Si oxidation and chemical etching or reactive ion etching (RIE), with the size of the imprint mold (stamp) selected to be 0.6cm × 0.6cm area, which contains more than ~200 million, periodically spaced, protruding sharp pillar tips of Si. The tips are either ~210 nm or ~380 nm spaced apart from the adjacent tips, with a very sharp tip end diameter of less than several nanometers, which allows an easy indentation into PMMA layer as well as a direct indentation imprinting onto Al thin film itself without PMMA resist layer coating. Nanoimprint molds as represented in Figure 3.2 were designed particularly for two different approaches: self-healing and pattern tripling as schematically shown in Figure 3.3.

3.2.3 Nanoimprint

In order to make pre-patterns on Al thin film surface, nanoimprint lithography machine (NIL: KIMM, ANT-2) was utilized to press against a spin-coated layer of poly(methyl methacrylate) (PMMA) resist on top of Al film or directly against Al film surface. The PMMA layer thickness was about 250nm. The nano-imprinting pressure was experimentally optimized to the regime of ≤ 1.3 kN/cm^2.

3.2.4 Pattern transfer

The pattern transfer from the imprinted PMMA onto underlying Al film surface was carried out by RIE using Oxford, Plasmalab 80 RIE; Trion, RIE/ICP Dry Etch. CF_4/O_2 gases and BCl_3 gas were utilized for PMMA and Al etching, respectively. For residual PMMA removal, Technics, PEIIB Planar Etch apparatus was used.

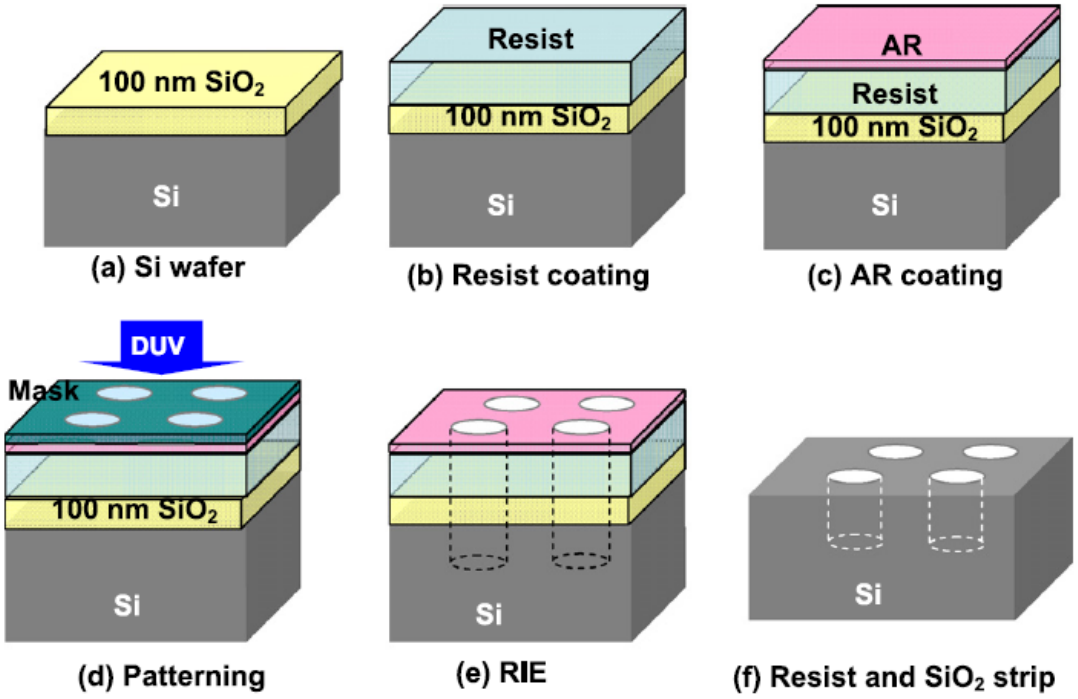


Figure 3.1: Schematic illustration of the Si nanotemplate fabrication process using DUV lithography.[78]

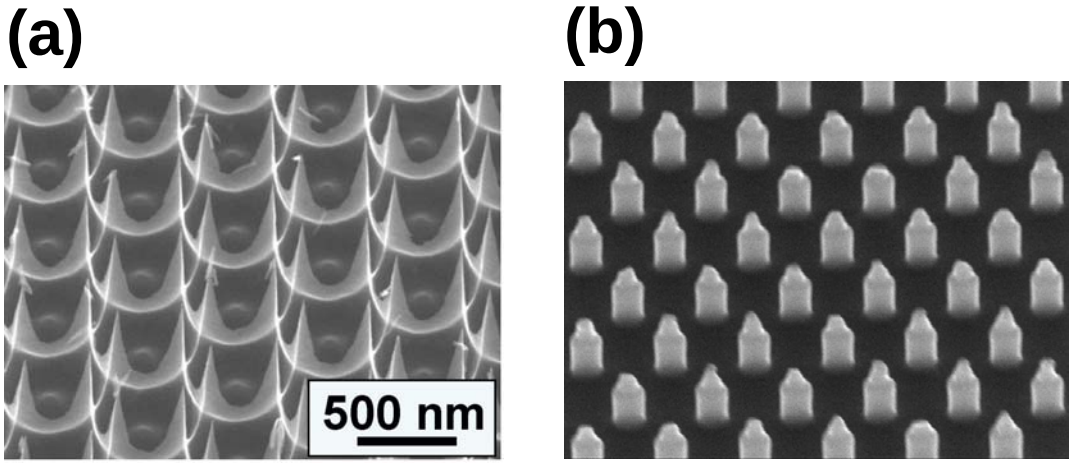


Figure 3.2: SEM micrographs of NIL stamps: (a) hexagonally arranged Si tip and (b) triangularly arranged Si tip.

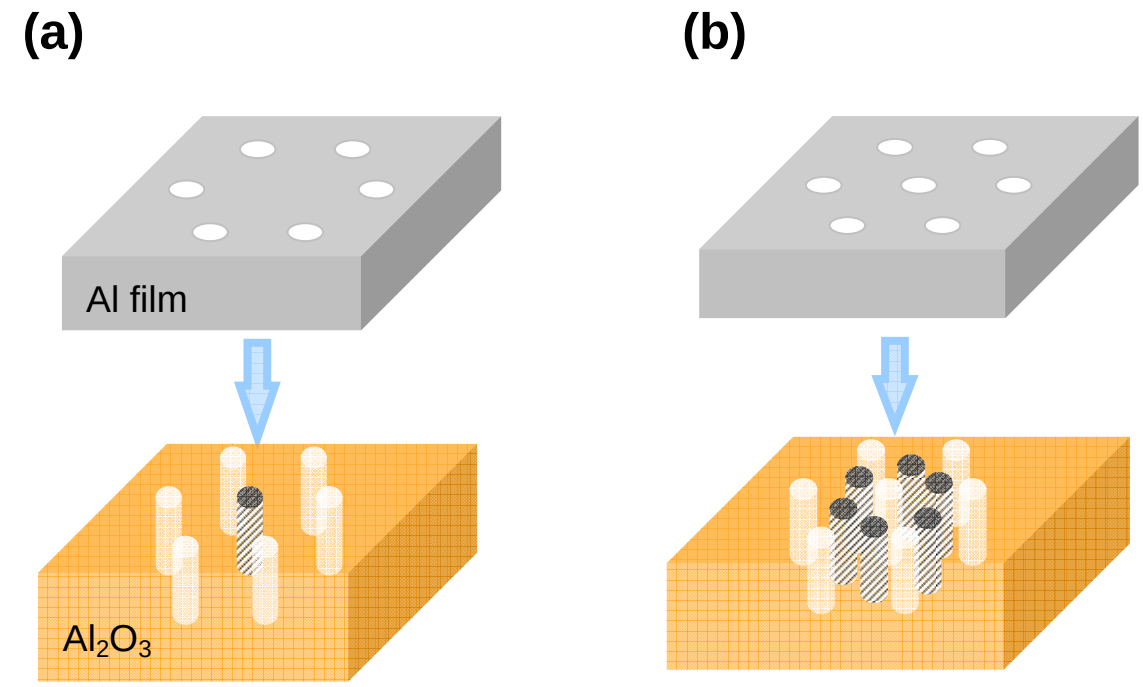


Figure 3.3: Two strategies for pattern multiplication: (a) self-healing and (b) pattern tripling.

3.2.5 Anodization

Anodization of Al thin films containing such pre-patterned surface nanocrater arrays was then conducted at 120~130V in 0.04M oxalic acid or 0.17M phosphoric acid solution with magnetic stirring (~300 rpm) at 1℃ using a DC power supply (GwINSTEK, GPR-30H100). Pore widening was applied in 5wt% phosphoric acid solution at 20℃ for several tens of minutes if needed. Overall experimental processes are schematically illustrated in Figure 3.4.

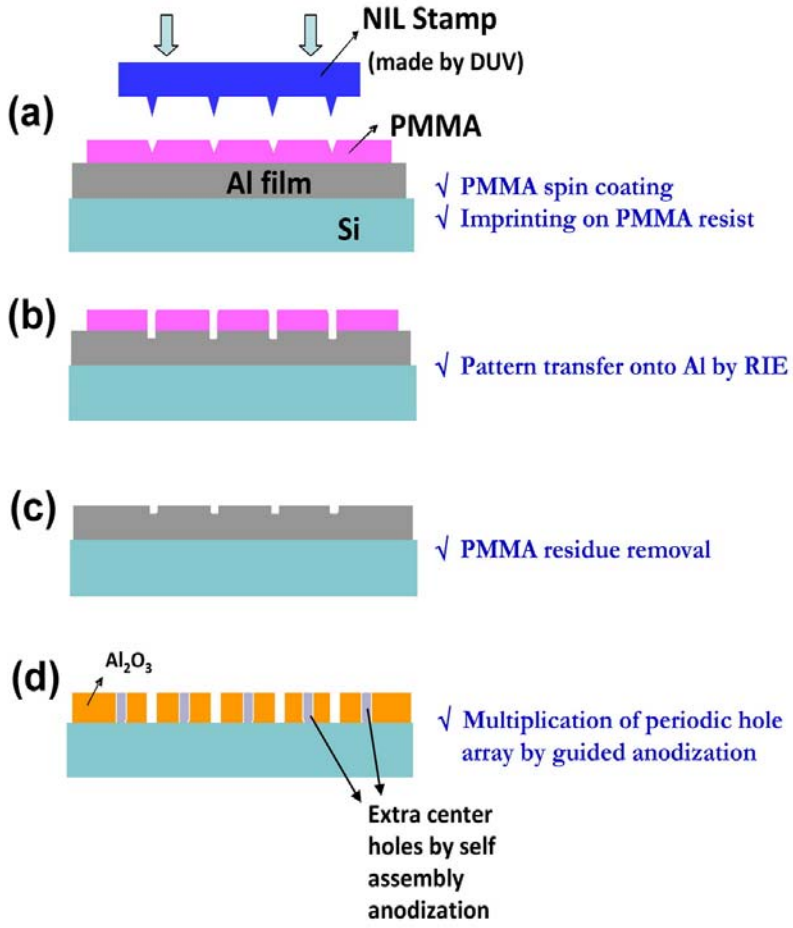


Figure 3.4: Schematic illustration of guided anodization procedures: (a) Nano-indentation imprinting on spin coated PMMA layer, (b) RIE process for pattern transfer to underlying Al film layer, (c) PMMA removal, and (d) anodization using the nano-indented array as nucleation sites.

3.2.6 Characterization

Microstructures of the specimens were analyzed by field emission scanning electron microscope (FE-SEM: Phillips, XL30 ESEM) and the surface roughness of the as-deposited Al film was measured by atomic force microscope (AFM: VEECO, Dimension 3100).

Table 3.1: Number of periodic pores in a single hexagonal cell before and after anodization in each case.

	Number of pores in a single hexagonal cell		
	Before anodization	After anodization	
	NIL-created pores	Newly formed pores	Total pores
Self-healing	2	1 (50%)	3 (150%)
Pattern tripling	3	6 (200%)	9 (300%)

3.3 Results and discussion

3.3.1 Al thin film roughness control

For successful fabrication on Si and other semiconductor substrates and devices, especially nano-imprint lithography process, a very flat substrate surface is essential. In order to perform nano-imprinting with a few to several nanometer regime dimensional accuracy, a large surface roughness of e.g., more than a few nanometers, is unacceptable as the nano-imprint mold pattern would not be transferred consistently in depth or would be confined at localized area according to degree of surface roughness which would hinder the desired long-range ordering. Sputter or evaporation deposited Al thin films often introduce rough surfaces. Thin film metallurgy of Al metallization on semiconductor devices has been studied much in the past few decades. Aluminum

atoms in thin films can diffuse leading to coarsening of surface structure, either during film deposition or over time at room temperature.

In order to reduce the surface roughness, we have employed a low temperature thin film deposition approach. Figure 3.5 shows the trend of the surface roughness of sputter deposited Al film prepared at various temperatures and for different film thicknesses. It is clearly seen that the root mean square (RMS) value of the surface roughness is improved significantly as both the Al film thickness is reduced and the substrate temperature is lowered. For example, for the case of 500 nm thick Al film, the low temperature deposition at -115℃ significantly reduced the surface roughness from ~3.0 nm to ~0.9 nm (measured over 10 μm x 10 μm area). The corresponding AFM images are shown in Figure 3.5(b) and (c). For the case of 1.5 μm thick Al film, a cryogenic temperature deposition produced significantly reduced surface roughness from ~3.2 nm for room temperature (25℃) deposition to 2.8 nm for -70℃ and 1.6 nm for -115℃ deposition. It is, however, worthwhile to mention that Al film can be peeled off from Si substrate while being deposited at extremely low temperature or heated back up to room temperature after film deposition. Therefore the Al film deposition temperature should be optimized depending on Al film thickness and roughness needed. With such a substantially reduced roughness of the starting Al film, it is anticipated that nano-imprinting can be applied with more reliable and reproducible results, and hence a special surface smoothing processing such as the chemical mechanical polishing (CMP) could be omitted.

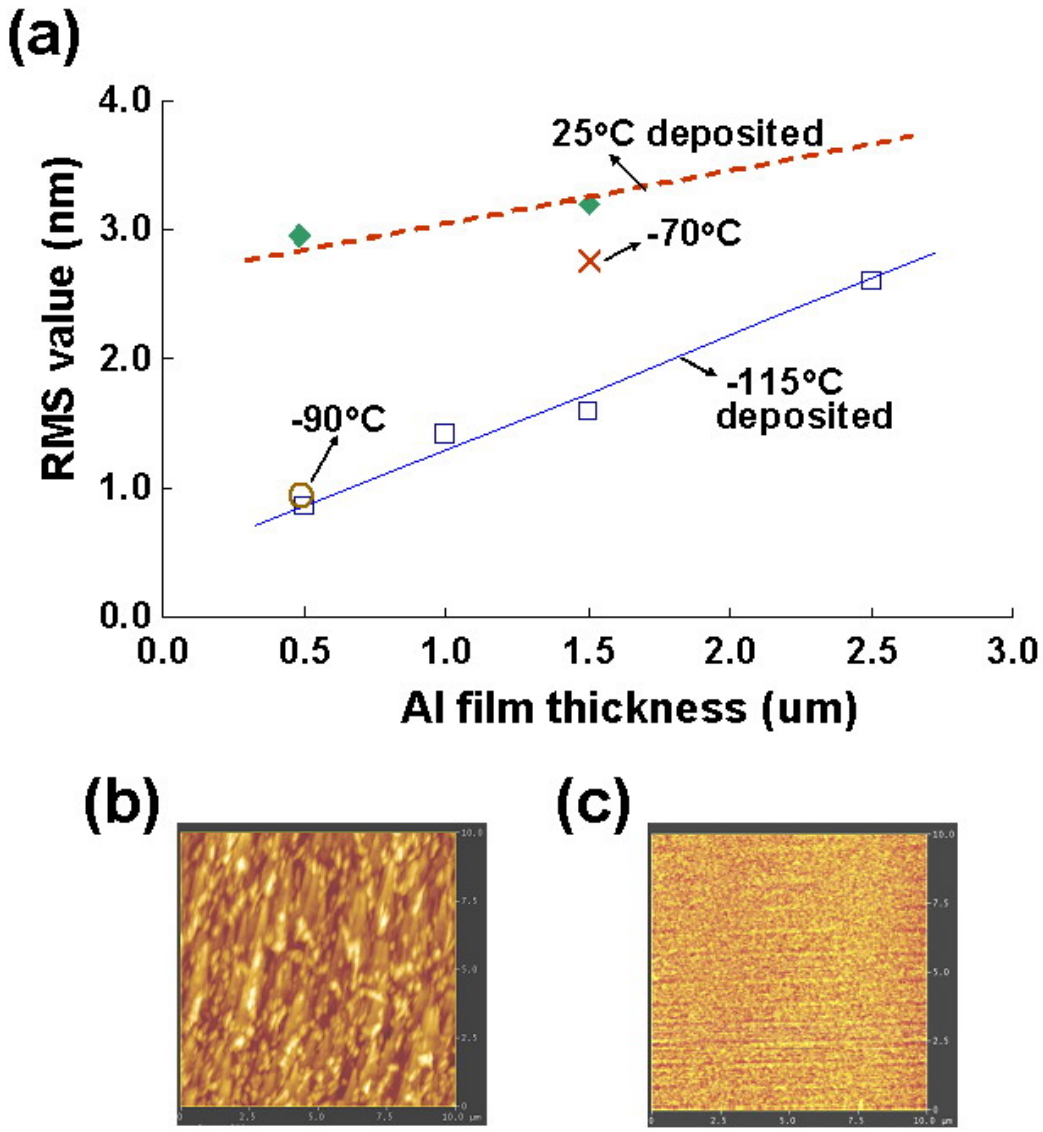


Figure 3.5: (a) Surface roughness of Al films sputter deposited on Si substrate at various temperatures and at different overall Al film thicknesses and representative AFM images of 500nm-thick Al films deposited at (b) 25℃ and (c) -90℃.

3.3.2 Guided anodization

For guided anodization, nano-indentation of the spin coated PMMA resist layer was performed using a Si based nano-imprint mold (stamp), followed by RIE pattern transfer of the indentation marks to the underlying Al film surface, resist removal, and anodization as described in the Experimental section. The specifics of anodization process such as the applied voltage significantly influences the morphology of the resulting nanostructure, and a rich variety of structures can thus be designed. We have conducted a study of anodized Al_2O_3 nanopores or associated morphologies on our directly nano-indented thin film Al material. Anodization was conducted under the same electrolyte species but with optimized concentration depending on the level of applied voltage. As is clearly shown in Figure 3.6, a different magnitude of the applied voltage during anodization of the indented Al films produces a variety of microstructural and pore morphologies, ranging from disordered porous structures (top left) to ordered nanotube-like structures. This unique tubular pillar structure formed by indentation especially in a long-range periodic fashion has not been reported before. At low voltages of 20 ~ 90 volts, a generally disordered AAO pore structures are observed, while at a higher voltage of 120 volts, more periodic nanotubular array structures with central pores are obtained as shown in the right side of Figure 3.6. The average slope of interpore distance to applied voltage curve was close to 1.6nm/V in contrast to the case of self-ordering regime: 2.5nm/V for mild anodization and 2.0nm/V for hard anodization in oxalic acid.[16]

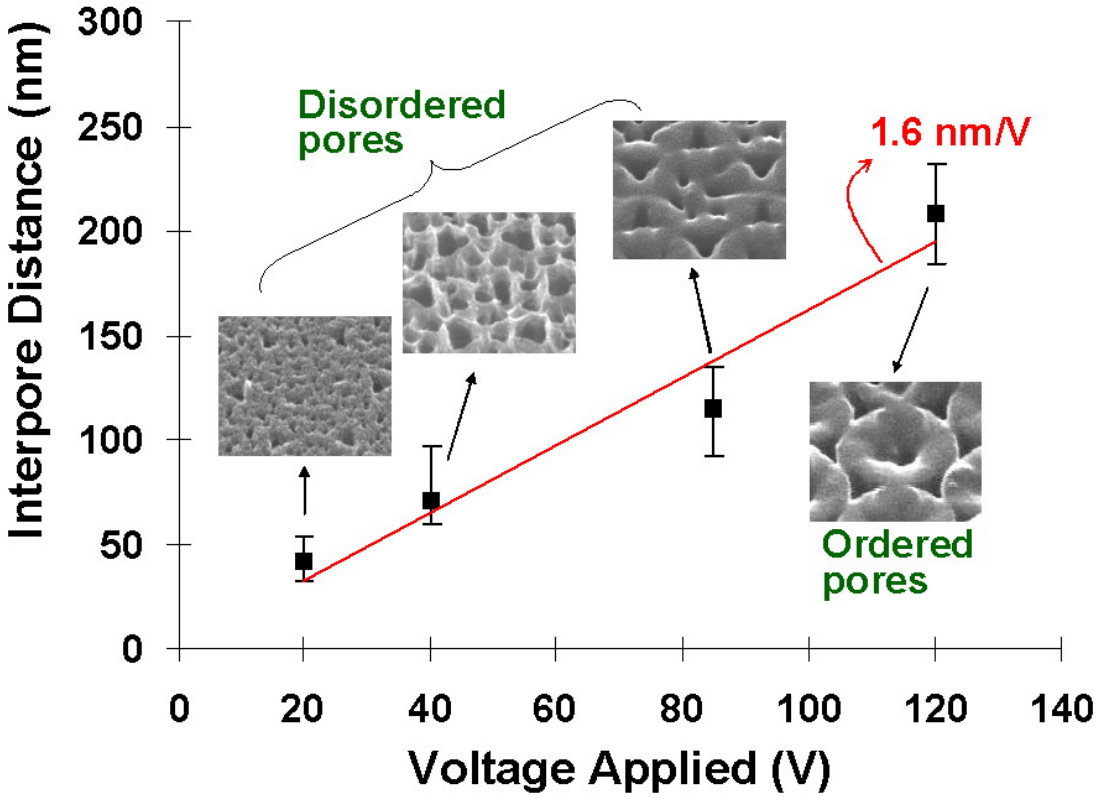


Figure 3.6: Anodized Al_2O_3 morphology and interpore distance on indentation-implanted Al film samples as a function of applied anodization voltage.

SEM micrographs of the Al films after the PMMA assisted anodization process using optimized anodizing voltage determined by Figure 3.6 type experiments are given in Figure 3.7. The pre-patterned Al film surface after removing left-over PMMA, Figure 3.7(a), shows the nano-indented spots (triangular shaped) in hexagonal arrays precisely replicating the nano-indenter stamp structure. After anodization in 0.17M phosphoric acid at 130V, a periodically arranged nanotube array structure is obtained as seen in Figure 3.7(b). In addition to the originally indented triangular spots in hexagonal array, new sets of pores are formed by self assembly anodization in the exact center of every

pseudo hexagon consisting of six previously indented crater spots. The number of overall pores (including the indented holes and self-assembly anodized holes) is thus increased exactly by 50%. This periodic pattern is long-range in nature, spanning 0.6 cm x 0.6 cm area identical to the total area of the nanoimprint stamp, with an example lower magnification SEM picture shown in Figure 3.7(c). A quantitative analysis such as by using Fast Fourier Transform (FFT) analysis for the ordered arrays can better demonstrate the periodicity over large area. Such an analysis can be employed in the future for larger-area samples. An accomplishment of such a long-range ordering in anodized aluminum oxide material is technologically and scientifically important as one of the limitations/drawbacks of the AAO process is the presence of domain boundaries with the AAO ordered pore orientation often confined within each of the micrometer regime domain size. Such a long-range, periodic Al_2O_3 structure demonstrated here can be useful for obtaining a large area device arrays with predictable positioning of nanodevices or nanostructures.

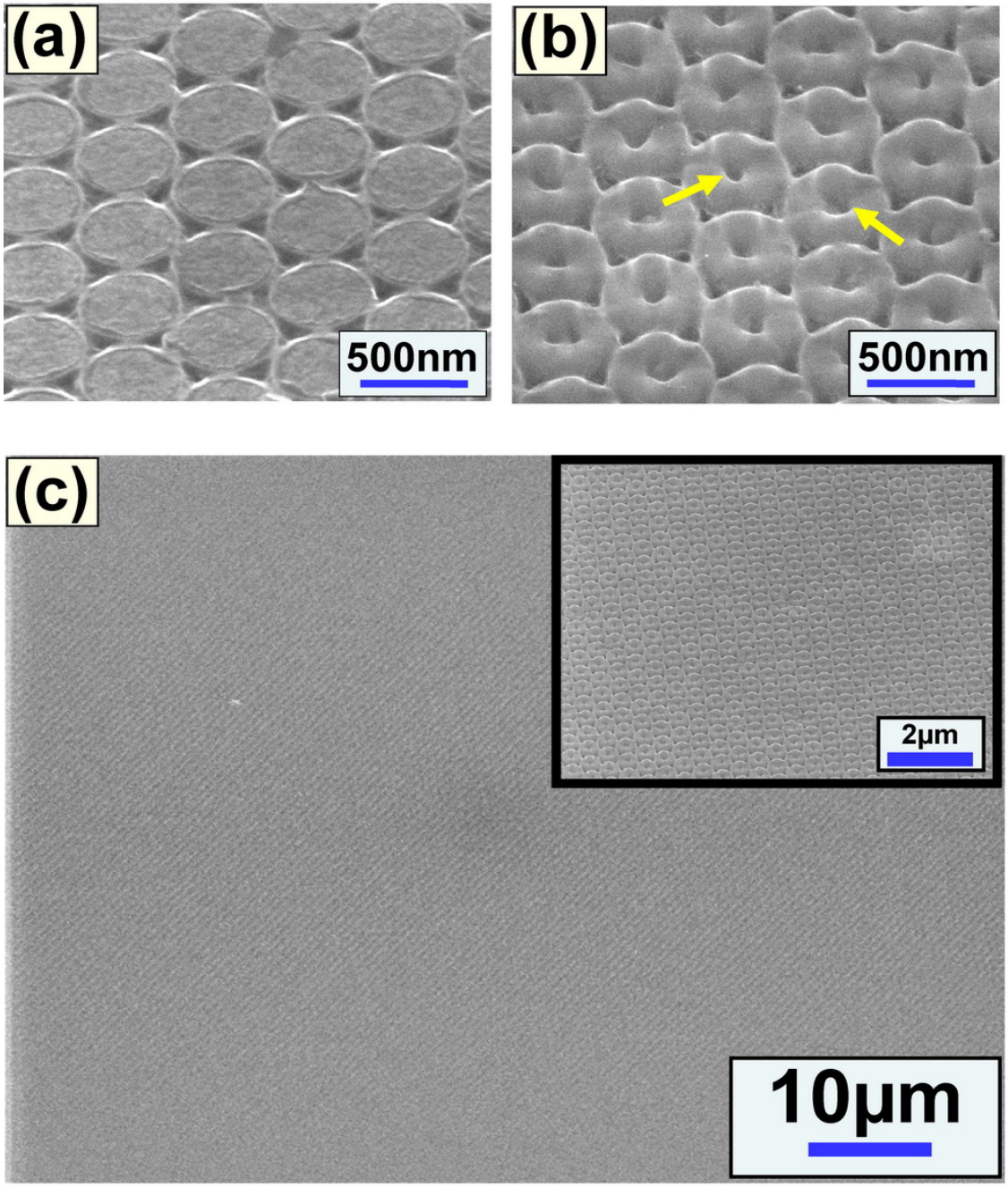


Figure 3.7: SEM micrographs of PMMA assisted process: (a) pre-patterned Al film surface after removing PMMA residue after patterns transfer, (b) the resulting AAO surface viewed at an angle, and (c) low magnification image representing highly long-range ordered AAO structures, which is evident pores were guided at the dimples location and newly formed at the center of six pre-patterns surrounding. The arrows in (b) show newly created pores in the center of pseudo hexagon during anodization. The sample was anodized in 0.17M phosphoric acid at 130V.

3.3.3 Al thin film surface engineering

Shown in Figure 3.8 are SEM images of AAO surface modification engineered by PMMA layer deposition on Al layer, nanoindentation-prepatterned then RIE dry etched prior to guided anodization. These samples were patterned by the the same hexagonally arrayed nanoimprint stamp shown in Figure 3.2(a). Figure 3.8(a-c) are top-view images while Figure 3.8(d-f) are tilted-view SEM images. A periodic nanopore array is evident at short dry etching time (Figure 3.8(a),(d)). Upon additional dry etching, nano-donut array is evolved (Figure 3.8(b),(e)) and upon further dry etching nanotube array structure is observed (Figure 3.8(c),(f)).

For comparison purpose, we have also applied a direct indentation on the Al film surface without using the PMMA resist. Shown in Figure 3.9 are SEM photographs of the sample directly indented on Al film, with the pre-patterned Al film surface after nano-indentation process (Figure 3.9(a)). The resultant Al_2O_3 nanotube array after anodization in 0.04M oxalic acid at 120V, represents a long-range periodically ordered structure as shown in Figure 3.9(b). Shown in Figure 3.9(c) is a lower magnification SEM micrograph and Figure 3.9(d) represents the cross-sectional micrograph which clearly shows the tubular nature of the Al_2O_3 nanotube array. The direct nano-indentation has an advantage in that the process is simpler and faster than using PMMA resist indentation and pattern transfer to Al film. However, the reproducibility and robustness of the long-range nanotube structure array appears to be better with the PMMA approach since some of the sharp tips on the nano-imprinter stamp (nano-indenter) tend to get damaged after several repeated imprinting operations if the process is not carefully handled. The PMMA layer is mechanically much softer than Al metal layer, therefore the nano-indentation tip array is more durable on PMMA layer. If we

utilize a nano-indentation stamp with a triangular pattern, rather than a hexagonal pattern, a different self-assembly anodization phenomenon is observed. In this case, a new hole is generated by anodization per each triangle bounded by nano-indented spots, thus the pattern is tripled instead of 50% increased hole numbers for the hexagonal pattern case. This process and associated SEM micrographs are presented in Figure 3.10. If the degree of pore widening is extended, eventually the structure turns into a nanotube array structure similarly as in Figure 3.9(d). These results indicate the versatility of nano-imprint process for reducing the AAO inter-pore distance and increasing the overall density of the nanopores through pattern-tripling.

The lack of long-range, periodic ordering of nanostructures has been a major bottleneck for practical applications of nanostructures for many electronic, photonic, and magnetic device applications, and our results described above, especially as a technologically useful thin film structure on Si substrates, contributes to facile fabrication and understanding of long-range ordered nanomaterials. The guided anodization approach described in this paper can be expanded by combining with pore filling methods such as electrodeposition[76] to fabricate precisely positioned nanowire arrays in large areas, or novel materials having bimodal diameter nanowire structures. The periodic nanotube arrayed structures can be useful for fabrication of a nano-patterned substrate for predictable positioning of arrayed electronic devices. Nanotube structures have been shown to be effective in enhanced biological reactions such as accelerated bone growth or stem cell differentiation[79, 80] and hence the large-area Al_2O_3 nanotube array structures reported here can be explored for biomedical applications as well. Our technique can also be utilized to produce large-area nano-

imprint stamps for creation of nanotube structures on many other materials such as silicon or titanium.

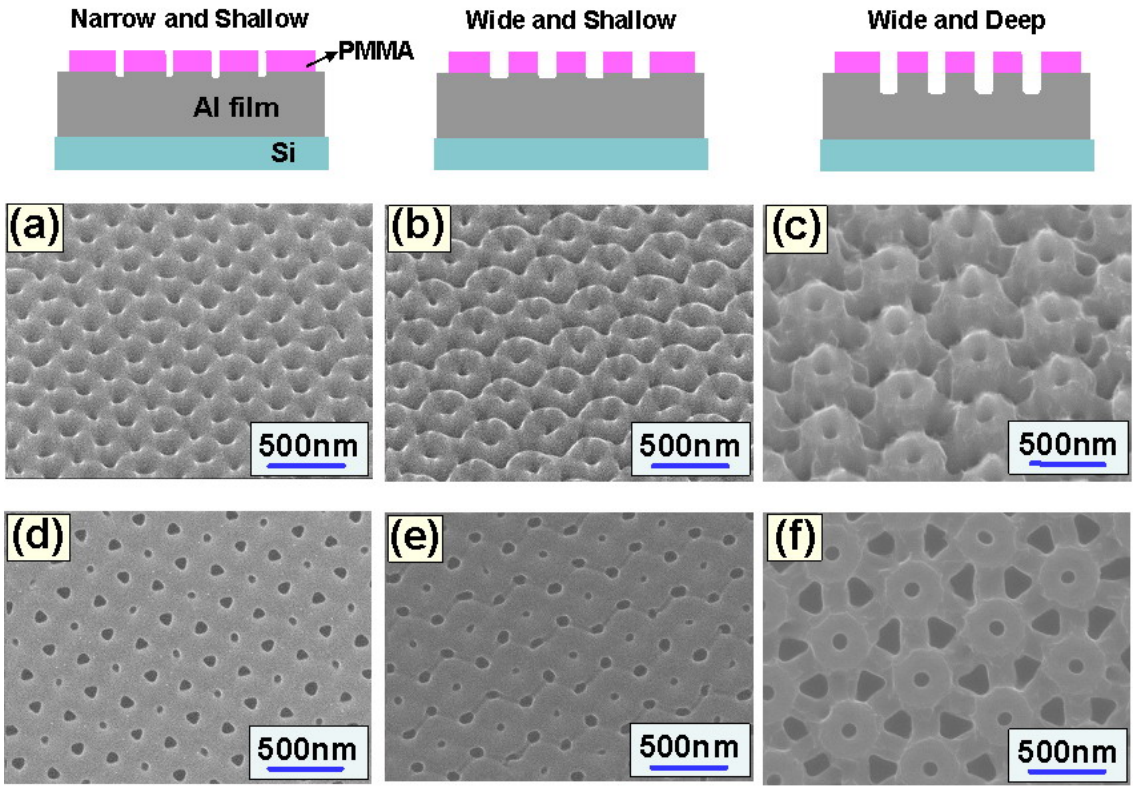


Figure 3.8: Top-view ((a),(b),(c)) and tilted-view ((d),(e),(f)) SEM images of AAO surface modification engineered by dry etching (RIE) of nano-indented PMMA prior to guided anodization: (a,d) a periodic nanopores, (b,e) a nano-donut, and (c,f) a nanotube array structure (pore widening for 70 minutes). Two consecutive dry etching recipes for PMMA first and then for Al underlayer were used for pattern replication. RIE etching time for PMMA and Al, respectively, was (90s, 60s) in (a,d), (120s, 60s) in (b,e), and (150s, 90s) in (c,f). The corresponding surface structures after RIE and guided anodization are schematically illustrated in the top panel. The subsequent anodization was conducted in 0.17M phosphoric acid at 130V.

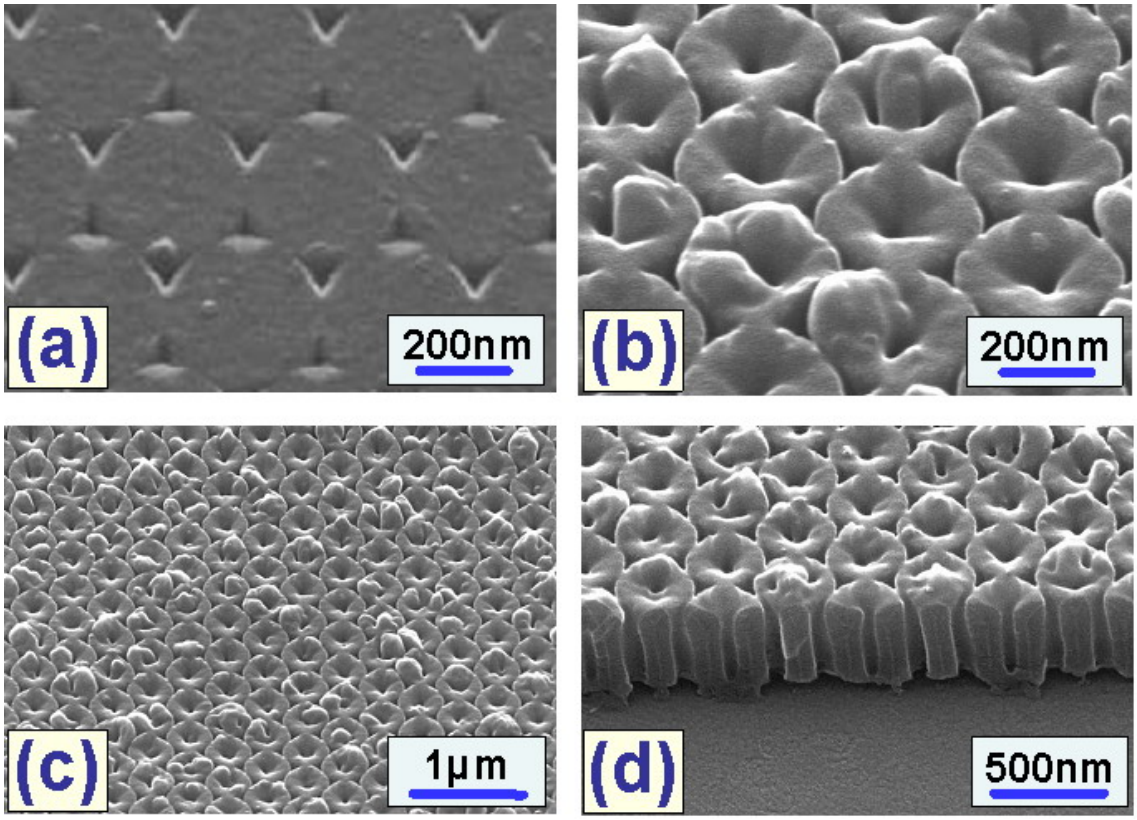


Figure 3.9: SEM photographs of the sample directly imprinted on Al film: (a) pre-patterned Al film surface after nanoimprint process, (b) the resulting AAO surface ensuring ordered fashion of the result AAO, (c) image at an angle, and (d) the cross-sectional image representing pores were vertically grown to Si substrate. The sample was anodized in 0.04M oxalic acid at 120V and pores were widened for 30 minutes. Note that the bottom of pre-patterned pores has no barrier layer while that of the newly created ones surrounded by pre-patterns has yet hemispherical barrier layer representing pores at the dimples reached Si substrate faster than the newly formed pores which might result from time delay due to pore initiation at the center of each hexagon.

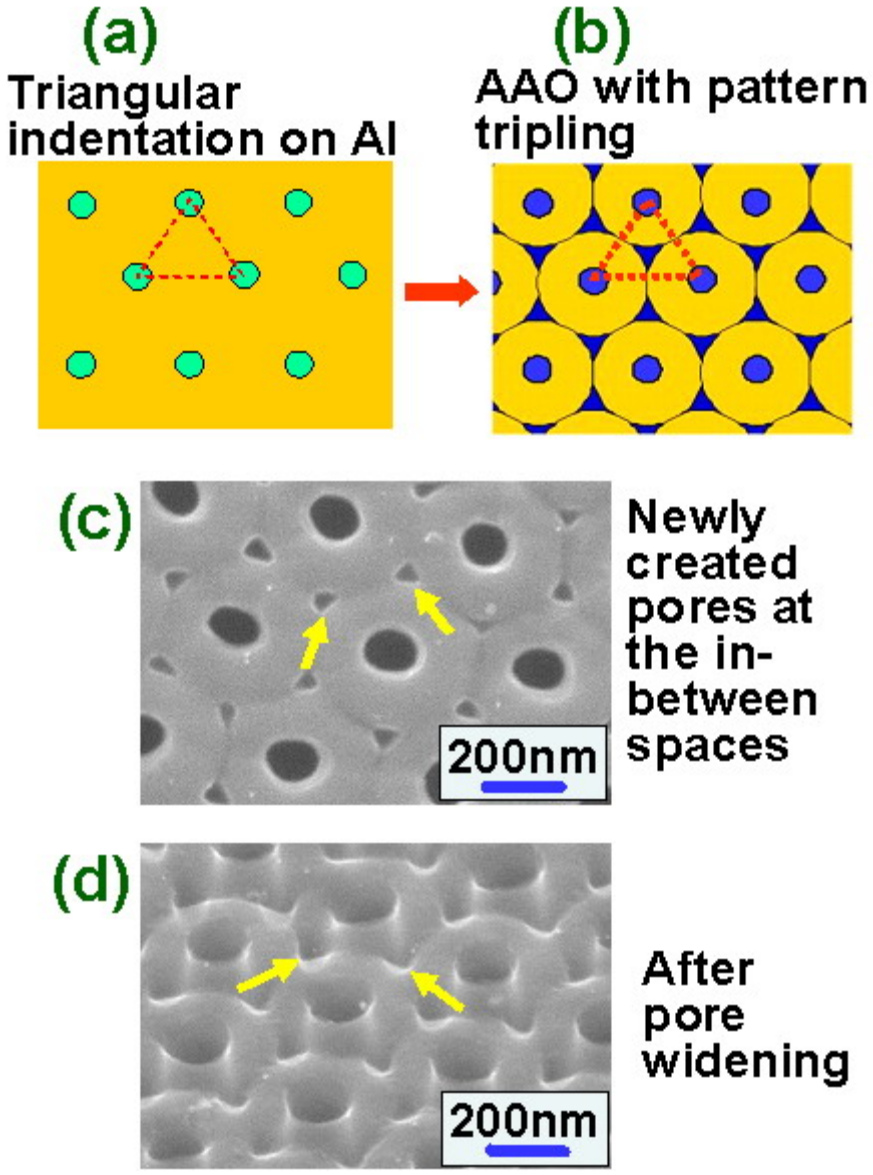


Figure 3.10: Triangular patterned Al nano-indentation on Al film and guided anodization for pattern tripling: (a) schematics for triangular indentation, (b) pattern tripling by self assembly anodization, (c) SEM micrograph of anodized AAO structure, and (d) microstructure after pore widening for 60 minutes. The arrows in (c) and (d) show newly created pores at the in-between spaces during anodization.

3.4 Summary

In summary, we have fabricated long-range, ordered AAO arrays consisting of periodically modulated pores or nanotubes through guided anodization method. Nanoimprint processes, either on spin-coated PMMA and RIE process or direct indentation on Al thin films allowed a faithful pattern transfer onto thin film Al layer underneath. Subsequent anodization process created a pattern tripling as well as long-range (0.6 cm x 0.6 cm area), periodic array of Al_2O_3 nanotube structure on Si substrates, with the patterning area limited only by the size of the nano-imprint stamp. A low-temperature deposition technique to produce sub-nanometer flatness in the Al film was also devised for improved indentation pattern transfer and anodization. The guided anodization process led to the creation of unique 3-dimensional tubular arrays, which can be used as a template to produce singular or bimodal nanowire arrays.

Such a periodic nanotube arrayed structure could be useful for fabrication of a large-area substrate for predictable positioning of arrayed electronic, magnetic or photonic devices, for enhanced biomedical applications, or for preparation of nanotube-shaped imprint stamps.

3.5 Future work

NIL has become one of the versatile lithographic techniques to create nanometer sized features due to its large area capability for pattern transfer to a substrate. However, despite the benefit of relatively easy and fast process, some difficulty still exists especially in inexpensive creation of well-defined master stamp having sub 100 nm pore/hole patterns. This hinders the NIL progress toward practical applications since the preparation of NIL stamps by an e-beam lithography is too costly. In order to make

NIL approach more viable for industrial applications, alternative methods for large area stamp fabrication would be desirable.

Towards this end successful demonstration of hexagonally ordered monodomain Si daughter stamps utilizing NIL-patterned anodized aluminum oxide (AAO) template as an etch mask is desirable to pursue. Using pattern multiplication approach discussed above, guided anodization of Al film can be utilized to fabricate Si daughter stamp as schematically shown in Figure 3.11.

Chapter 3, in full, is a reprint of the material as it appears in Journal of Vacuum Science and Technology B, 28(6), C6M88 (2010) written by Kunbae Noh, Chulmin Choi, Jin-Yeol Kim, Young Oh, Karla Brammer, Mariana Loya, and Sungho Jin. The dissertation author was the primary investigator and author of this work.

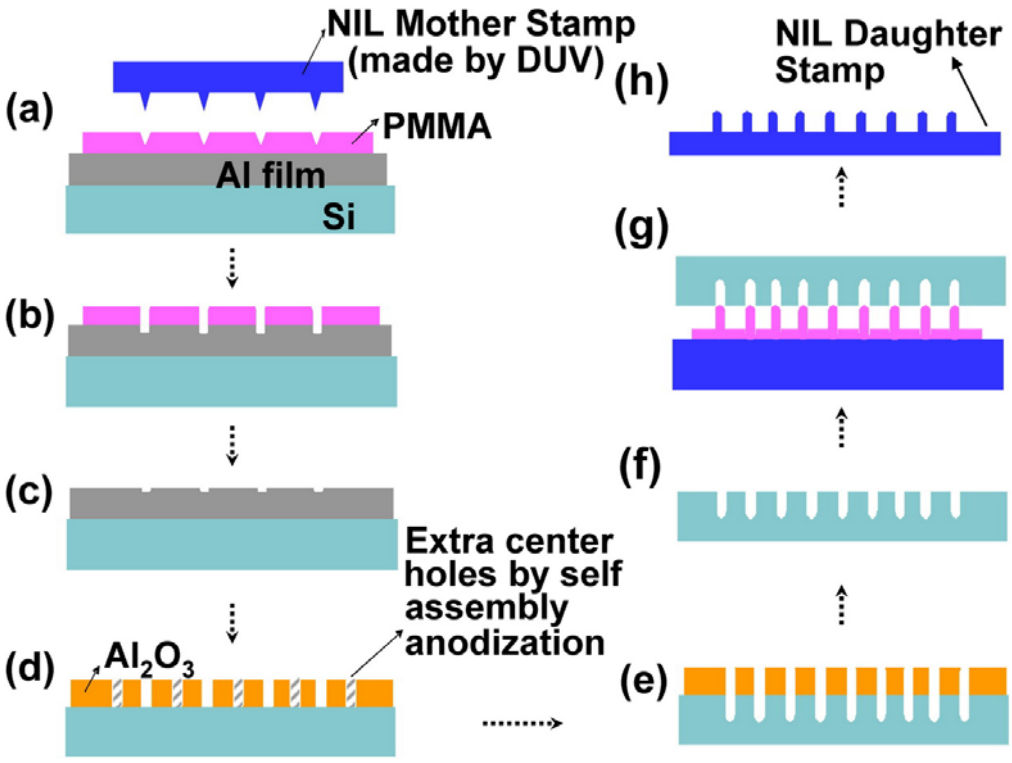


Figure 3.11: Schematic daughter stamp fabrication procedures: (a) nanoimprinting on PMMA resist, (b) pattern transfer into Al film surface by RIE, (c) PMMA removal, (d) guided anodization, (e) pattern transfer into Si substrate by RIE, (f) AAO removal, (g) nanoimprinting on PMMA resist, and (h) pattern transfer into Si daughter stamp by RIE.

CHAPTER 4:
Fabrication and applications of self-assembled S4VP directed AAO template

4.1 Introduction

Although conventional lithographic methods can provide precisely located nanoarrays, the size of the area that can be patterned is often limited to the micrometer scales due to its intrinsic time-consuming nature of serial processing in addition to the limited processing resolution.

As an alternative, self-assembly nanoarrays have been extensively investigated, such as BCP, AAO or DNA assembled structures. One of the most fascinating properties of self-ordered nanoarrays lies in the readiness of its fabrication on length scales that are difficult to obtain by standard semiconductor lithography technique.[81] Along the same line, block copolymer micelle nanolithography (BCML) was developed which is suitable for obtaining hexagonally ordered metal, metal oxide, and SiO_2 nanoclusters.[82-84]

In this chapter, we discuss the fabrication of self-assembled poly(styrene-*b*-4-vinylpyridine) (S4VP) nanotemplate and demonstrate two potential applications: (1) RIE shadow mask for antidot patterned Co/Pd magnetic multilayer and (2) S4VP-guided Al thin film anodization and magnetic nanowires synthesis.

4.1.1 Magnetic multilayer for bit patterned media (BPM)

Metal multilayer has been intensively investigated as a model system for bit patterned media (BPM) application due to its high perpendicular magnetic

anisotropy.[85] Co/Pd multilayer has been one of the most frequently studied materials due to its increased resistance to oxidation as well as the high perpendicular anisotropy in the as-deposited condition, together with the ability to tailor magnetic properties by changing the film thickness and layer thicknesses. For BPM applications, magnetic island or hole arrays are considered as potential candidates since they exhibit high magnetic anisotropy due to the selection of materials such as $L1_0$ phase or layered magnetic structure in addition to the engineered nanostructures. The dots/anti-dots serve as defects to hinder magnetic domain wall motion and thus leading to magnetic hardening effect.[86-89] The anti-dot pattern with enhanced magnetic anisotropy and higher coercivity can be useful for conventional media such as perpendicular recording media. The anti-dot pattern, strictly speaking, may not be viewed as a bit-patterned-media structure since the magnetic material is laterally somewhat connected. However, it may be possible to construct viable recording media as the high-coercivity magnetic material regions among three adjacent holes (e.g., in hexagonally arranged hole arrays) are only partly connected to the neighboring magnetic regions, and may also be utilized as individual information storage bits, in a sense like a pseudo bit-patterned-media.

One promising way to fabricate such magnetic dot/anti-dot structures by nanopatterning is to utilize di-block copolymer (DBCP) having vertically aligned nanoporous templates. Such nanotemplate materials can be useful for high density storage media applications since they can offer not only relatively inexpensive processing but also provide highly ordered island or hole arrays directly applicable to various types of substrates including Si.[90-93] In the first section of the results, magnetic properties of anti-dot structured Co/Pd multilayer fabricated by S4VP block copolymer will be presented.

4.1.2 S4VP-guided Al thin film anodization and magnetic nanowires synthesis

Despite some benefits arising from chemically patterned block copolymer (BCP), thermal stability and structural rigidity of BCP is considered as the main drawbacks due to ultrathin BCP thickness in the regime of a few tens nanometers in addition to the inherent degraded polymeric nature during post treatment, for example, during reactive ion etch (RIE) process, which makes it difficult to be applied for high aspect ratio nanostructure applications, i.e. nanowires. In addition to some previous efforts using nanoporous BCP as an RIE shadow mask for pattern transfer onto underlying substrate,[94-97] advanced techniques by emerging two different type of self-assembly such as AAO and BCP, or directed-BCP assembly for pattern multiplication are highly desirable for faithful pattern formation as well as for high density pattern applications.

Taking advantages of robust structure of metal oxide nanotemplate against thermal, mechanical and/or chemical stresses, AAO can be a good candidate for broad applications. Analogous to NIL-assisted Al thin film anodization discussed in Chapter 3, BCP-guided (e.g., S4VP) aluminum anodization offers a good way to form hexagonally arranged pre-patterns on Al surface to make guided anodization happen. Due to the smaller interpore distance in S4VP, high density pore arrays which cannot be obtained from self-ordered anodization can be obtained, which can lead to a facile route to achieve high density nanoarrays. An exemplary Ni nanowires (NiNWs) array was electrochemically deposited into AAO holes guided by self-assembled S4VP template.

In the latter part of this Chapter, fabrication and magnetic properties of such Ni nanowires are discussed.

4.2 Experimental procedures

4.2.1 Si substrate pre-treatment

(100) Si substrate was cut into ~1cm×1cm size and cleaned in acetone, isopropyl alcohol, and methanol successively with ultrasonication followed by D.I. water rinse. Then, specimens were immersed in piranha solution comprised of (7:3 (v/v) = H_2SO_4 : 30% H_2O_2) for 20 min at 80 ℃ followed by copious D.I. water rinse.

4.2.2 Thin film deposition

Prior to Al thin film deposition, 50nm thick Au film was evaporated with 20nm thick Ti adhesion layer between Si substrate and Au film layer. Al thin film was sputter-deposited at ~-50℃ to compromise surface roughness and residual film stress as described in Chapter 3.3.1.

4.2.3 BCP film fabrication

The patterned structure was made by di-block copolymer self assembly followed by reactive ion etch (RIE) process. Poly(styrene-b-4-vinylpyridine) (S4VP) (number-average molecular weight, $M_{n,\ PS}$ = 41.5 kg mol^{-1}, $M_{n,\ P4VP}$ = 17.5 kg mol^{-1}, M_w/M_n = 1.07, where M_w is the average molecular weight) was purchased from Polymer Source (Montreal, Canada) and used without further purification. A 0.5wt% S4VP copolymer solution dissolved in toluene was spin-coated at 2000 rpm for 60 seconds on a cleaned

Si substrate. This film was then exposed to tetrahydrofuran (THF) vapor in a closed glass vessel for 1~3 hr to induce mobility and allow the phase separation to occur. The film was then immersed in pure ethanol for the P4VP phase to swell and thus leading to a porous structure.

4.2.4 Pattern transfer

4.2.4.1 Si wafer

To resist reactive ion etch (RIE) plasma while patterns were being transferred to the Si substrate underneath, 5 nm-thick Cr thin film was vacuum-deposited at an angle (with the substrate rotation) to ensure that the Cr film covered the whole PS-b-P4VP layer surface except the pore bottoms. The deposition angle used for deposition was ~60° off the vertical axis. Without the angled deposition, the Cr coating partially covering the bottom surface of the pores hinders RIE gas etching of residual P4VP present at the pore bottom. For pattern transfer, two consecutive RIE conditions were utilized. One was for etching DBCP residue at the hole locations using 50 mTorr of the mixed CF_4 and O_2 gases under 65 W, RF plasma power (Oxford Plasmalab 80 RIE) for 30 s, which was fixed throughout all the experiments. The other was for etching the Si substrate below exposed by the previous RIE step. For the latter, 15 mTorr of the mixed C_4F_8 and SF_6 gas at 30 W of RF plasma power with 1200 W of inductively coupled plasma (ICP) power (Oxford Plasmalab 100 RIE/ICP) was utilized to enhance the etching directionality. Commercial Cr etchant (Type 1020, Transene Company, Inc) and oxygen plasma were used to remove Cr and residual S4VP film, respectively, after the RIE process.

4.2.4.2 Al thin film

Analogous to pattern transfer onto Si, two consecutive RIE processes were applied. Since a shallow indentation is sufficient, no additional Cr deposition was applied prior to RIE process. The first RIE etching is for P4VP residual layer removal located at the bottom of holes. RIE process parameters were further optimized by using CF_4 gas (Oxford Plasmalab 80 RIE) for different time interval. The latter was to etch Al film exposed to the air formed at the previous RIE step. For the latter, BCl_3 gas was utilized to create shallow pre-patterns on Al thin film.

4.2.5 Guided anodization

Pre-textured Al thin film was anodized under constant voltage in 2.5M sulfuric acid at 5℃. Anodizing time was experimentally determined until noticeable changes in electric current occur, for example, an abrupt drop to 0 mA or a sharp increase arising from Au underlayer exposure to electrolyte. For the purpose of barrier thinning to expose the pore bottom and enable the initiation of electroplating of metal nanowires, additional anodization was applied under constant current condition ($1mA/cm^2$). Finally, barrier layer was completely removed by chemical etching in 5wt% phosphoric acid. When necessary to produce and expose electroplated bare metal wire arrays, the as-anodized AAO membrane matrix was selectively removed by using 1M NaOH aqueous solution followed by thorough D.I. water rinse.

4.2.6 Co/Pd magnetic multilayer deposition

Co and Pd layer was alternately sputter-deposited on the pre-patterned substrate, controlled by a computer program (visual basic software). 4 nm-Ta was pre-deposited

as an adhesion layer followed by 3 nm Pd layer. Then, four layers of alternating Co/Pd (0.27 nm and 0.8 nm in thickness, respectively) were deposited so that the final film structure can be described as $Si/Ta_{4nm}/Pd_{3nm}/[Co_{0.27nm}/Pd_{0.8nm}]\times 4$. The overall process of Co/Pd multilayer on hole-patterned Si substrate was schematically illustrated in Figure 4.1.

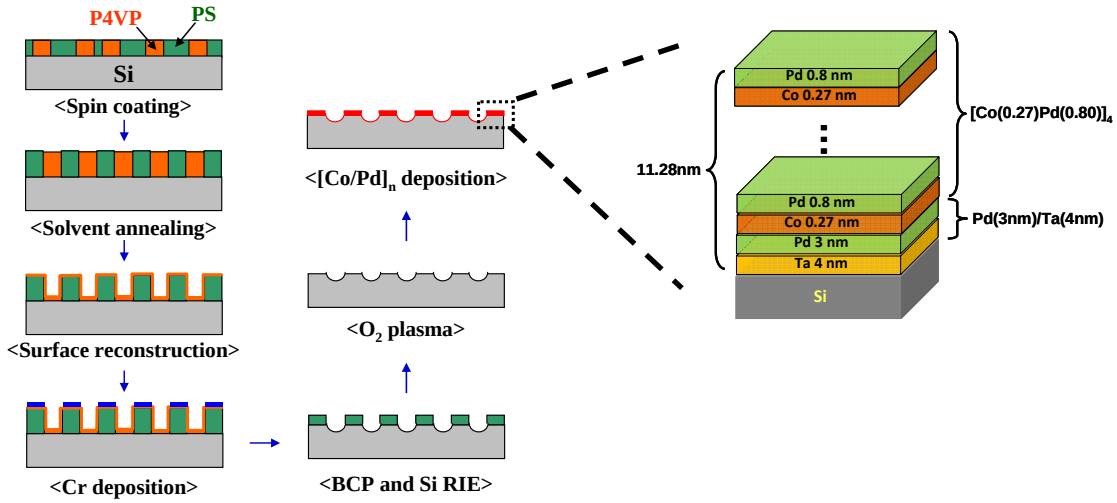


Figure 4.1: Schematics of overall anti-dots array fabrication and Co/Pd multilayer structure.

4.2.7 NiNWs Electrodeposition

Ni nanowires (NiNWs) were synthesized via electrochemical deposition into S4VP-guided, periodic AAO nanopores by pulse power supply (Dynatronix).

Electrolyte is composed of 300g $NiSO_4 \cdot 6H_2O$, 45g $NiCl_2 \cdot 6H_2O$, 45g H_3BO_3 in 1 liter D.I. water (Watt bath). For uniform deposition over the whole sample area, pulsed electrodeposition was applied and each pulse consists of 5ms "on" followed by 5ms "off" under constant current condition during electrodeposition process. The bath temperature was maintained at 20℃ and electrolyte was gently stirred. Deposition process was terminated before the voltage decreased due to overgrown NiNWs. The overall process of S4VP-guided anodization and NiNWs synthesis are schematically illustrated in Figure 4.2.

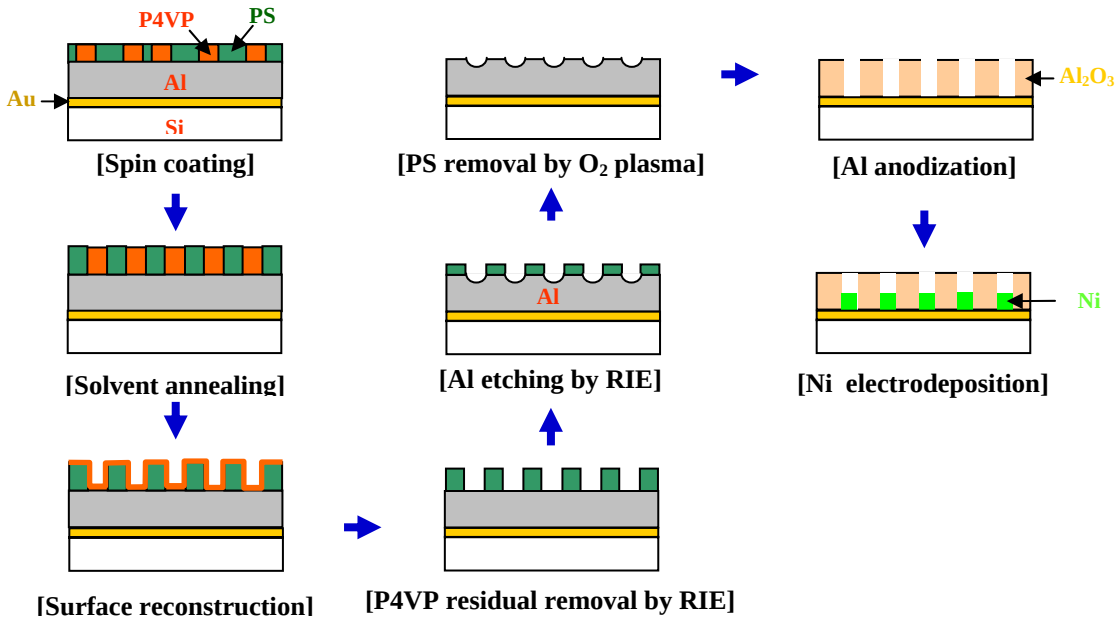


Figure 4.2: Schematic illustration of the overall NiNWs synthesis using S4VP-guided AAO template.

4.2.8 Characterization

The sample microstructure was characterized by ultra high resolution scanning electron microscopy (UHR SEM; FEI XL30) and the magnetic properties were evaluated by alternating gradient magnetometer (AGM; Micromag 2900) and superconducting quantum interference devices (SQUID; MPMS SQUID VSM, Quantum Design).

4.3 Results and discussion

4.3.1 Structural evolution of S4VP self-assembly

It has been reported that a S4VP di-block copolymer thin film can be further ordered by THF vapor annealing treatment and thus leading to improved close-packed cylindrical P4VP microdomains[92, 98]. Depending upon annealing time in THF vapor, microstructural ordering is enhanced as annealing time increases. When the solvent-annealed film is immersed in ethanol, the S4VP film reconstruction occurs due to its solvating power difference on PS and P4VP, which induces a nanoporous film as shown in Figure 4.3. However, upon further being exposed to THF vapor, S4VP film starts to be detached from the substrate as marked in Figure 4.4. Therefore, precautious processing is highly required to obtain more ordered S4VP thin film, which can be directly used as an RIE mask in order to transfer hole patterns onto an underlying substrate such as Si or glass.

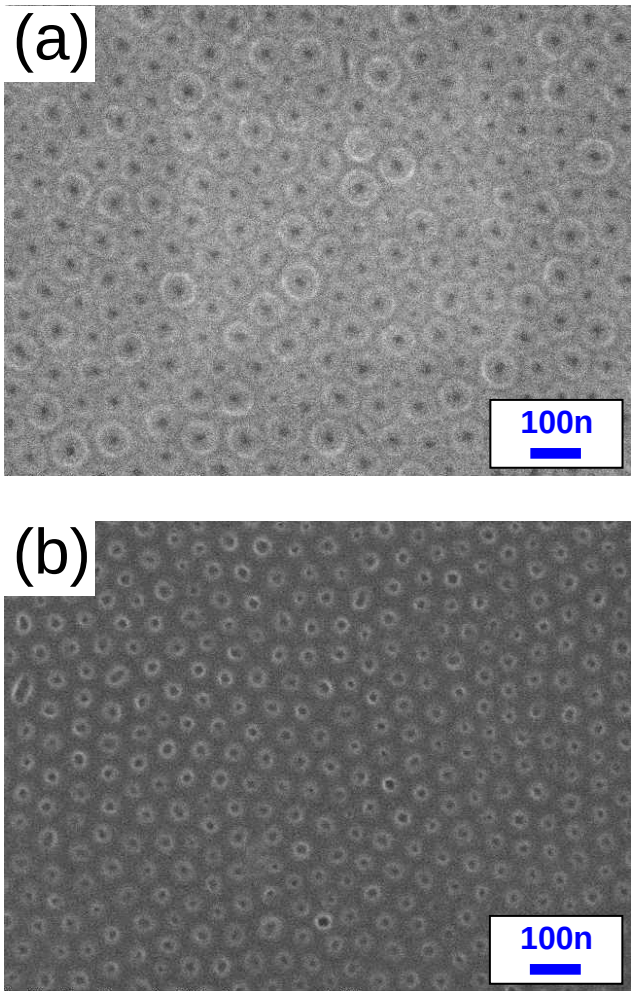


Figure 4.3: SEM micrographs of S4VP film on a Si substrate: (a) as-spun and (b) after THF-annealing for 1.5 hr. Note that images were taken after samples were immersed in ethanol during 30 min for the P4VP phase to swell so as to form a porous structure.

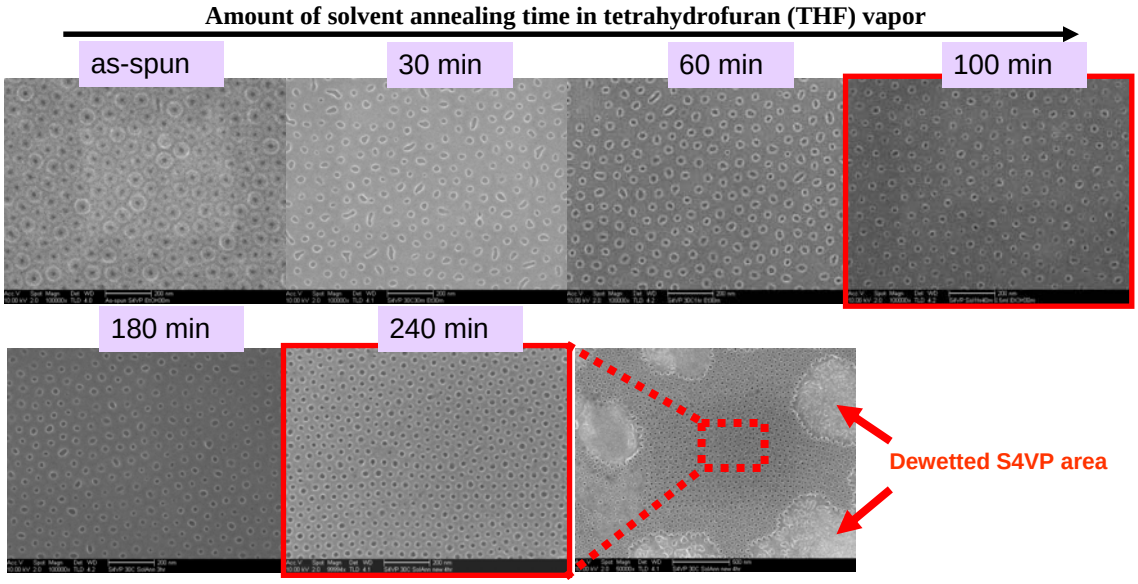


Figure 4.4: Structural evolution of S4VP thin film with respect to annealing time in THF vapor.

4.3.2 Pattern transfer

To resist against potential damages by RIE plasma during Si etching process, a thin Cr film was vacuum-deposited at an angle to coat most of the patterned S4VP surface except the bottom of pores so as to etch Si selectively. Revealed in Figure 4.5(a) are Si hole patterns with partially removed Cr-coated S4VP film to highlight that Si hole patterns are successfully and rapidly created by using the S4VP etch mask. Depending on dry etching time, hole depth can be varied as shown in Figure 4.5(b). As the RIE time for Si etching increases, however, the sidewall of holes are also gradually etched in addition to mostly vertically anisotropic Si RIE etching, thus leading to an undercut Si hole structure with lower region getting etched more than the top region. Represented in Figure 4.6 are the SEM images of Si hole patterns as a function of

increasing RIE time from (a) to (c). Pores were enlarged laterally in addition to directional vertical etching so that some material of flat Si surfaces in-between pores was eroded (Figure 4.6(b)) or damaged to less well-defined structure (Figure 4.6(c)) due to partial RIE mask removal during extended RIE time and to sidewall necking resulting from isotropic Si undercut profile. No nanopatterns were obvious on further extended RIE time due to essentially complete etching of Si surface regions.

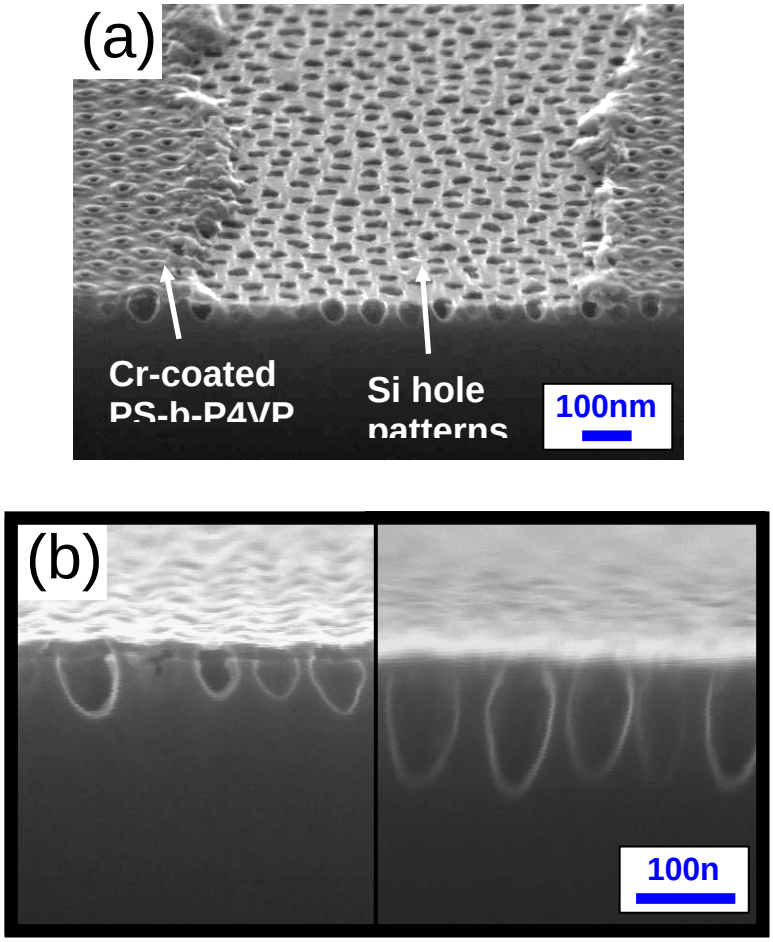


Figure 4.5: SEM micrographs of S4VP assisted Si nanopore formation: (a) tilted view after partially removing Cr coated S4VP film to reveal the Si layer (b) cross-sectional view of Si hole depth for two different RIE times, 1 minute (left image) and 2 minutes (right image).

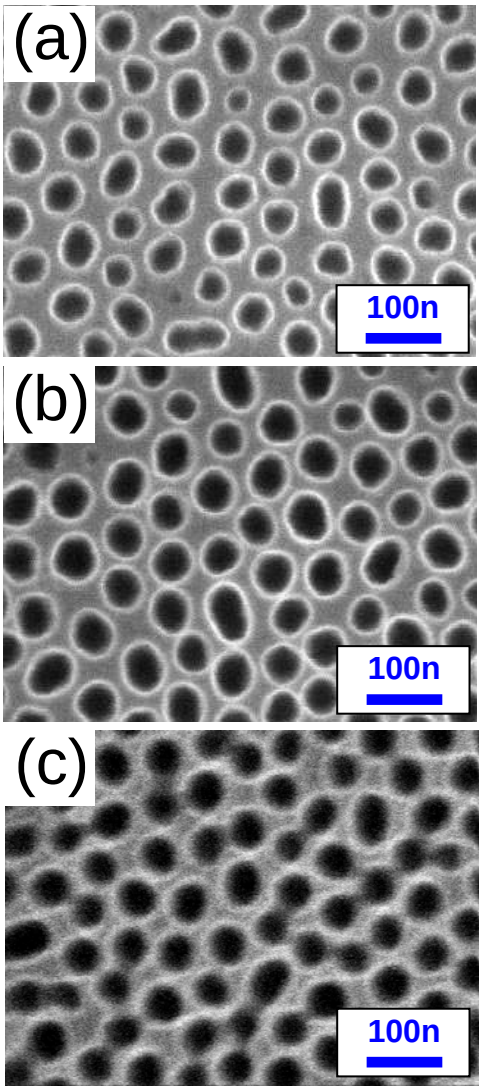


Figure 4.6: SEM micrographs of pattern transferred Si nanoholes vs RIE time: (a) 1 min, (b) 2 min, and (c) 3 min. Each pore is enlarged and eventually meets with adjacent pores as RIE time is increased. Contrast difference near interpore areas in (c) corresponds to height difference from the original Si surface due to extended RIE time which leads to an undercut profile of pore geometry and Si erosion.

For S4VP pattern formation on Al film, UV-ozone cleaner was applied for 1hr with 3mTorr oxygen gas flowing prior to S4VP spin-coating in order to enhance wettability of S4VP film on Al thin film. The representative SEM images before and after solvent annealing treatment are seen in Figure 4.7, which shows that highly self-ordered S4VP film is developed on Al thin film. The interpore (pore-to-pore) distance, an important parameter to determine the applied voltage for anodization, is 48.3nm ± 2.7nm based on SEM micrograph analysis.

In contrast to NIL-assisted Al pre-texturing demonstrated in Chapter 3, the Al RIE condition needs to be further optimized since not only those patterns to be transferred are much smaller (20 ~ 30nm) in diameter but also the S4VP film thickness which serves as RIE etch mask is thin (20 ~ 30nm). Shown in Figure 4.8 are SEM images after RIE processes. When residual S4VP layer is removed, Al film located at the bottom of pores is exposed to the air and, in turn, it is etched in the second RIE process as shown in Figure 4.8(b).

Prior to the S4VP-guided anodization, the S4VP film was completely removed by oxygen plasma. Anodizing voltage is determined on the basis of linear relationship of interpore distance to applied voltage ($D_{int} = 2.5V_{app}$) and other parameters such as species and concentration of electrolyte and temperature, which are empirically determined. Represented in Figure 4.9 are SEM images of S4VP-guided AAO. The arrangement and dimension of pores are well-matched with those of S4VP film, confirming AAO pore dimensions and placements were guided well by S4VP pre-patterns (Figure 4.9(a)). The pores are vertically well aligned (Figure 4.9(b)).

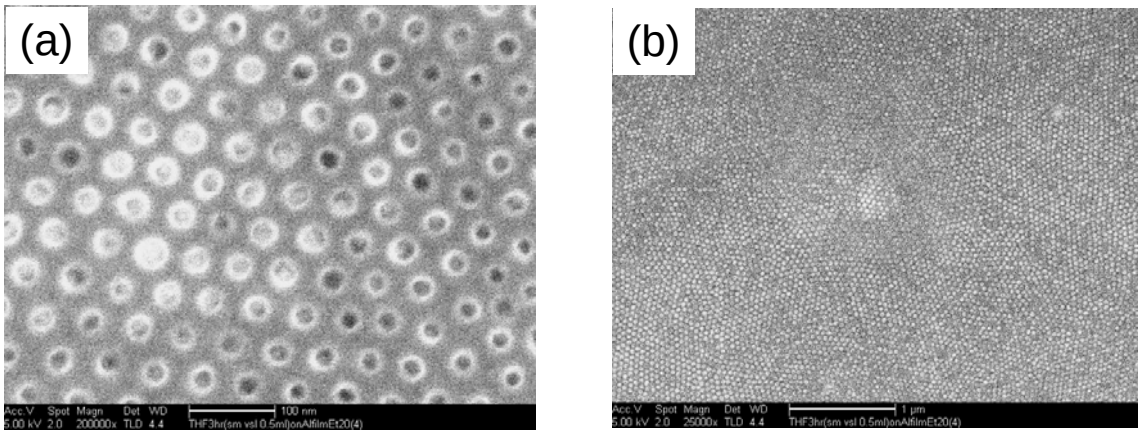


Figure 4.7: THF-annealed nanoporous S4VP film on Al thin film. The sample was immersed into ethanol for 20 min to develop the porous structure.

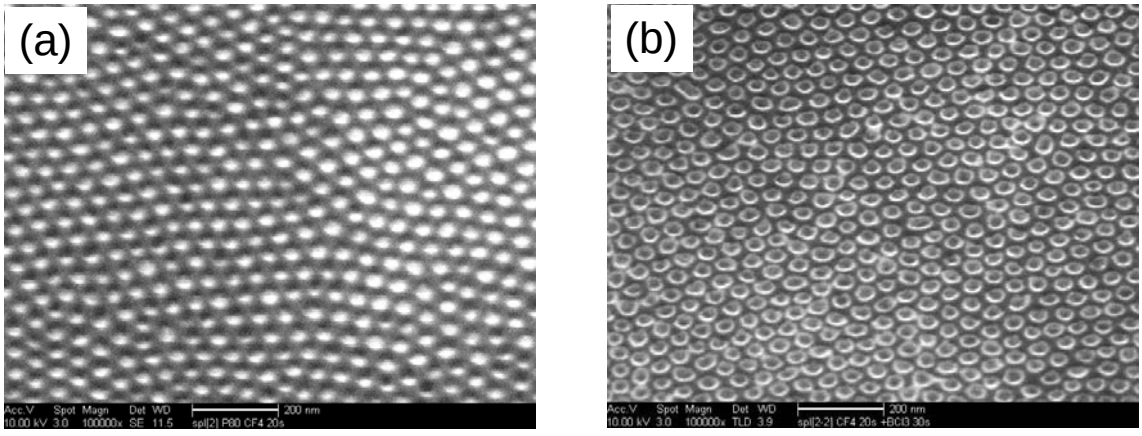


Figure 4.8: SEM micrographs of S4VP film after RIE process: (a) RIE I: Residual P4VP etching located bottom of the pores. Bright spots reveal Al underneath porous S4VP film (b) RIE II: Selective Al etching exposed to the surface. Dark spots inside bright rims reveal bare Al indents created by RIE process.

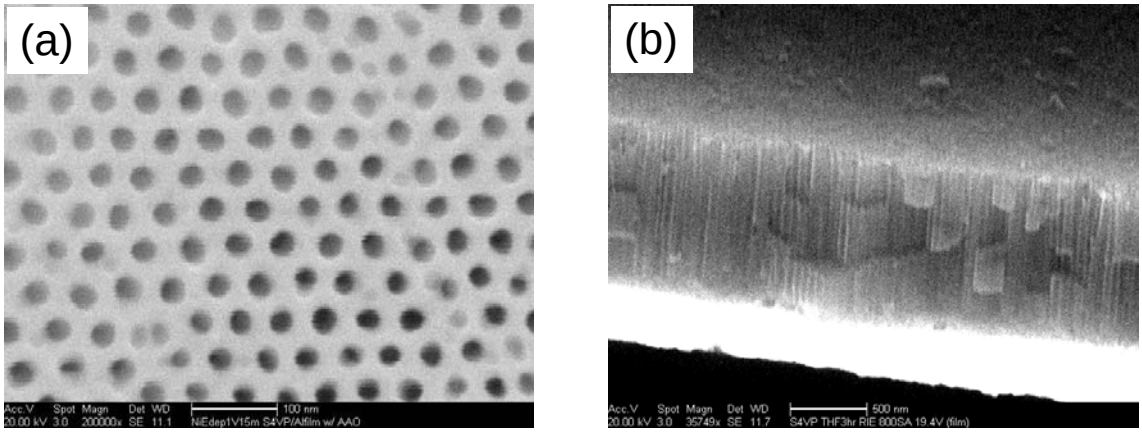


Figure 4.9: SEM micrographs of S4VP-guided AAO: (a) top and (b) tilted view. A specimen was anodized in 2.5M sulfuric acid under constant voltage of 19.4V.

4.3.3 Templates for magnetic materials synthesis

4.3.3.1 Alternative Co/Pd multilayer

To study magnetic recording media properties on the DBCP-guided, anti-dot nanostructured Si, a $[Co/Pd]_4$ multilayer was sputter-deposited on top of each nanopatterned substrate as well as on a flat Si substrate as a control sample. As shown in Figure 4.10, most of the Co/Pd multilayer materials were well deposited on the Si surface except the nanoholes location, giving rise to magnetic anti-dot structure corresponding to the original PS-b-P4VP template nanopattern dimension. Cross-sectional SEM images reveal that the pore depth was increased until certain time but decreased afterwards due to Si erosion and hole necking, leading to a less well-defined

nanopatterns as can be seen in Figure 4.6. Represented in Figure 4.11(a) and (b) are magnetic hysteresis curves of the $[Co/Pd]_4$ magnetic anti-dot structure measured normal to and parallel to the substrate, respectively. In contrast to the continuous $[Co/Pd]_4$ multilayer film on a flat Si substrate ($H_c \sim 1{,}100$ Oe), the identically deposited $[Co/Pd]_4$ films on a nanohole patterned Si substrate exhibit much higher coercive force values ($H_c \sim 3{,}400$Oe), which is more desirable for the bit patterned recording media application. The curve, C however, exhibits a lower H_c as discussed below. The significantly increased coercivity with strong perpendicular magnetic anisotropy in the anti-dot magnetic structure is attributed to the impeded domain wall motion due to the presence of nonmagnetic nanoholes.

It should be pointed out that a small amount of the Co/Pd materials were also deposited within Si nanoholes in addition to the Si surface since Co/Pd materials were directly deposited without mask. Consequently, the Co/Pd multilayered anti-dot patterns provide a mixture of two M-H loop curves consisting of a square-loop, high anisotropy material with increased coercive force (obviously from the top $[Co/Pd]_4$ multilayer) and a slightly skewed, lower coercivity loop with reduced anisotropy, most likely from some of the Co/Pd materials deposited within the pores. As discussed earlier, as the RIE time is increased, the Si anti-dot structure gets partially eroded, and hence the portion of the high anisotropy material from the well-defined $[Co/Pd]_4$ multilayer located on the flat surface portion of the Si gets reduced. As a result, the magnetic hysteresis loop is altered to become magnetically softer as shown in curve C of Figure 4.11(a) representing lower coercivity than that of continuous flat Co/Pd multilayer. The anti-dot $[Co/Pd]_4$ multilayer created here is highly vertically anisotropic as is desired for the bit patterned media. The overall in-plane magnetic anisotropy (measured parallel to the

sample surface) seems to be rather small as indicated by very low coercive force and negligible remanent induction, as shown in Figure 4.11(b).

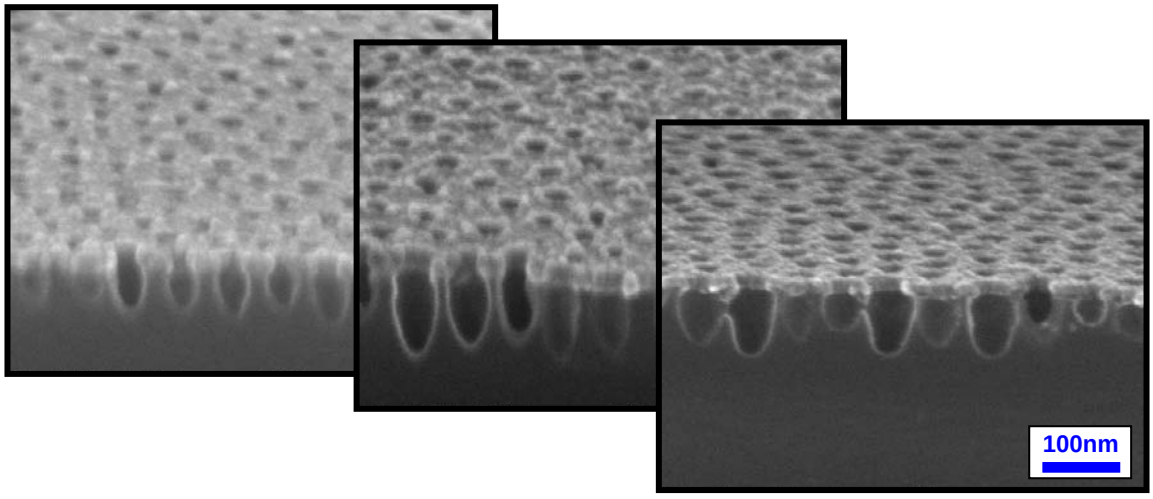


Figure 4.10: Cross-sectional images of $(Co/Pd)_4$ magnetic multilayer deposited on Si nanohole arrays corresponding to Figure 4.6 (a), (b) and (c), respectively (1, 2, and 3 minutes RIE from left to right), showing that most of the magnetic materials are well-deposited on Si surface.

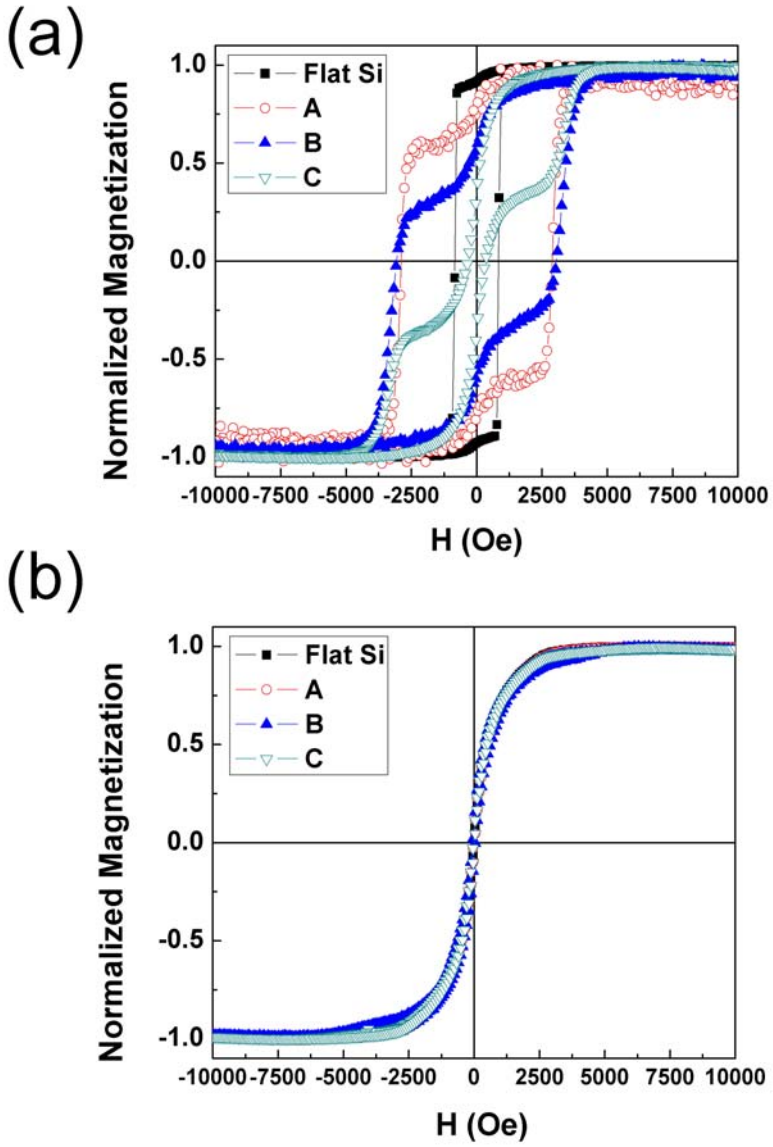


Figure 4.11: Magnetic hysteresis data measured (a) normal to and (b) parallel to the sample surface. A, B, and C correspond to samples shown in Figure 4.10 (1, 2, and 3 minutes RIE from left to right), respectively.

4.3.3.2 NiNWs

In contrast to laterally ordered BCP template having relatively small height (e.g., ~100 nm regime), vertically aligned and laterally ordered AAO nanotemplate has an advantage of having very high aspect ration, which is ideal for synthesis of long 1-D nanowires. However, direct integration of AAO onto other substrates such as Si and glass is not always easy to control. Furthermore, poor lateral ordering of pore arrangement when a thin Al film is used as a starting material hinders further advanced application of AAO in combination with mature Si technology. While some efforts via lithographic techniques to form pre-patterns on Al film surface enable to create guided AAO nanopores, however, this has been possible in only relatively small sized areas as discussed earlier. In this aspect, BCP-guided AAO patterns, particularly if the AAO layer is directly adhered to a Si substrate, would be of great technical interest by virtue of the following reasons:

(1) It offers highly ordered, vertically aligned AAO pores over a large area, directly attached onto Si, which has not been demonstrated before,

(2) The dimensions of the pores so created are relatively small i.e. higher density in the number of pores per unit area compared to the typical self-ordered AAO pores, and

(3) No extra Al materials need to be consumed except the almost exact target amount of aluminum thickness. If such a guided anodization is not used, a few tens of micrometers thick Al materials should be sacrificed due to the need to do the so-called "two step anodization" to obtain relatively uniform AAO pore arrays. Therefore, it is difficult to obtain well ordered AAO pores via sole self-ordering process alone from the deposited thin film aluminum layer. In this work, highly dense, ordered nanoporous

AAO membrane on Si substrate was successfully achieved by using two self-ordering materials in combination, i.e., di-block copolymer and AAO. Such a process may enable a low cost, high throughput nanotemplate fabrication.

Similarly as the previous $(Co/Pd)_n$ type magnetic applications, we have demonstrated a vertically aligned 1-D magnetic NiNWs array to show the versatility of the (DBCP + AAO) derived nanotemplates as a 1-D nanomaterial array synthesis. Represented in Figure 4.12 are NiNWs electrodeposited into AAO membrane. As seen in the cross-sectional SEM image of Figure 4.12(a), NiNWs having an average diameter of ~30 nm and average height of ~ 1 μm are filled into almost every AAO pore. To elucidate its dimension, AAO membrane was selectively etched in 1M NaOH solution followed by D.I. water rinse and air drying. Figure 4.12(b) represents a NiNWs array released from AAO membrane. Highly uniform NiNWs were electrochemically synthesized and the vertical alignment was assured. Since NiNWs length spans more than 1μm, local agglomeration was observed probably due to van der Waals force or magnetic interactions between neighboring NiNWs while wet etching and the successive air drying. The neighboring Ni nanowires can be separated from each other by using supercritical CO_2 drying or freeze drying processes.

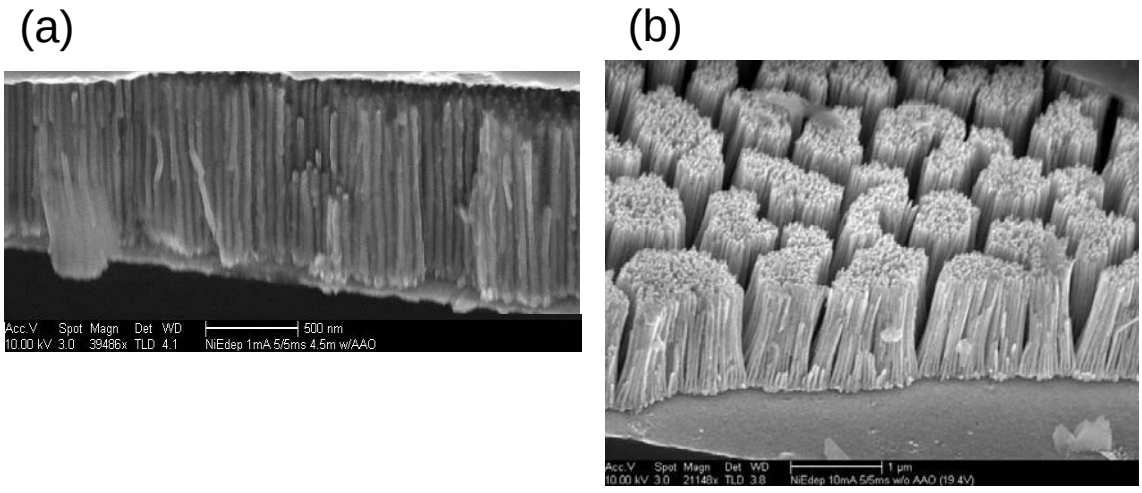


Figure 4.12: Electrodeposited ~30 nm diameter, 1 μm tall NiNWs (a) confined into AAO nanopores (cross-sectional view on fracture surface) and (b) liberated nanowires from AAO template which was removed by selective chemical etch in 1M NaOH (aq.).

The magnetic properties of the Ni nanowires were measured using Alternating Gradient Magnetometer (AGM). As shown in Figure 4.13, magnetic hysteresis curves were measured along the out-of-plane vs in-plane direction. To prevent magnetic noise arising from slanted NiNWs after selective AAO removal, magnetic data were collected from a NiNWs array confined into AAO pores as seen in Figure 4.12(a). Due to the elongated geometry of as-deposited NiNWs, the coercive force Hc, the intensity of the applied magnetic field required to reduce the magnetization to zero after the magnetization has been driven to saturation, is higher along the out-of-plane direction (along the vertical direction) than the in-plane direction, indicating that the magnetic easy axes is located along the NiNWs long axes as is anticipated. A relatively high magnetic field is required to reverse magnetic moment direction, caused by the magnetic shape anisotropy. As the shape anisotropy is often much smaller than the

crystal anisotropy in high Hc magnets such as rare earth magnets or hexaferrite magnets, the vertical M-H loop becomes somewhat skewed presumably due to the demagnetizing factor of closely spaced yet relatively short Ni nanowires.

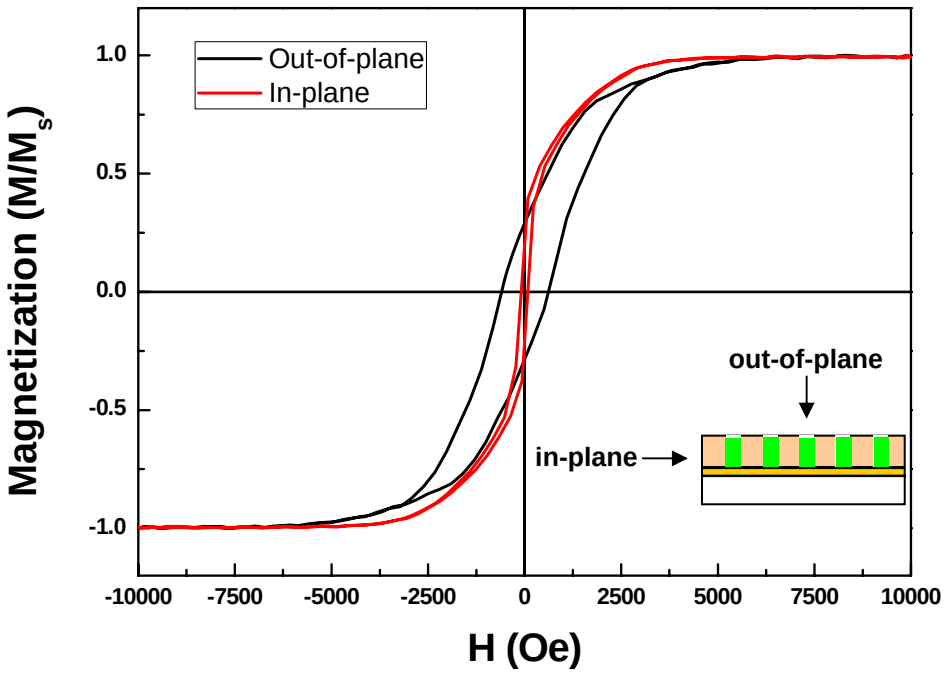


Figure 4.13: Magnetic hysteresis loop measured out-of-plane (normal to the sample surface) and in-plane (parallel to the sample surface) direction, respectively.

4.4 Summary

A $[Co/Pd]_n$ multilayer patterned magnetic recording media with an anti-dot structure and vertically aligned Ni nanowires have been created on a hole-patterned Si substrate and into an AAO membrane on a Si substrate, respectively. On the one hand, the anti-dot magnetic media was fabricated by dry etching using a self-assembled di-block co-polymer pattern as an effective RIE etch mask. We demonstrated that the magnetic properties of Co/Pd multilayer can be altered and improved by nanostructuring Co/Pd multilayer using a phase-decomposed di-block co-polymer template. Due to anti-dot structure, coercive force was significantly increased from 1100 Oe to 3400 Oe with strong perpendicular magnetic anisotropy. The in-plane magnetic anisotropy appears to be negligible. The improved coercive force is attributed to the impeded domain wall motion due to the presence of nonmagnetic nanoholes in the anti-dot magnetic structure.

Extremely fine (~30 nm diameter), vertically aligned NiNWs were successfully fabricated by electrodeposition into a BCP-guided AAO template on a Si substrate. Analogous to Co/Pd multilayer, perpendicular magnetic anisotropy is also observed due to shape anisotropy of vertically aligned NiNWs. An efficient way to synthesize highly ordered 1-D nanowires array was demonstrated. Further research will be necessary to appreciate the versatilities of guided AAO templates and associated potential 1-D nanowire fabrication and applications.

4.5 Future work on BCP-guided AAO

In order to obtain more controlled magnetic antidot structures confined only to the top surface and to elucidate their magnetic behavior, the sidewall of Si pores should be blocked from Co/Pd multilayer codeposition by using some clever masking effect. As schematically shown in Figure 4.14, chemically driven metal nanodots derived at the bottom of P4VP phase can also serve as deposition masks during magnetic multilayer deposition. Upon lifted-off of the BCP from the substrate, magnetic multilayer anti-dots will be left behind. In addition to such anti-dot structures, fabrication and magnetic properties of Co/Pd multilayer dots (islands) are of great interest, which will be one of the future tasks to be investigated with the template-assisted processing.

In regards to ordered AAO template fabrication onto Si substrate, directed BCP arrays introduced in Chapter 2.2 is of importance to develop a facile route to achieve high density nanowire or nanoisland arrays. Moreover, the confinement of BCP into AAO showed interesting nanostructures depending upon the AAO hole size as well as on different BCP properties such as molecular weight and type of each chain element.[99-103] Therefore, it is of interest to investigate the geometrical effect of BCP on advanced AAO nanostructures.

Chapter 4, in full, is a reprint of the material as it was submitted for publication in IEEE Transactions on Magnetics written by Kunbae Noh, Chulmin Choi, Hyunsu Kim, Young Oh, Jin-Yeol Kim, Daehoon Hong, Li-Han Chen and Sungho Jin; and, in part, has been prepared for publication in Journal of Vacuum Science and Technology B written by Kunbae Noh, Chulmin Choi, Hyunsu Kim, Young Oh, Jin-Yeol Kim, Se-Yeon Jung, Tae-Yeon Seong and Sungho Jin. The dissertation author was the primary investigator and author of both these papers.

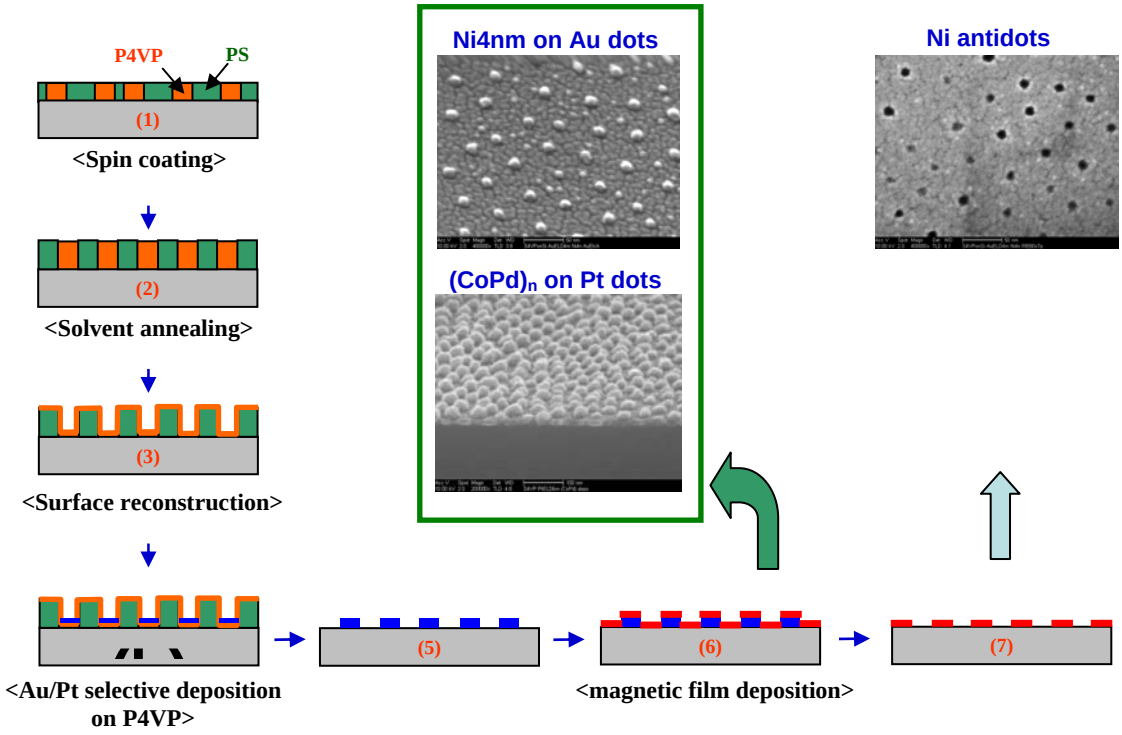


Figure 4.14: Scheme of magnetic anti-dot structure fabrication using chemically driven metal nanodots, e.g. Au or Pt, and the representative preliminary data.

CHAPTER 5:
Novel nanotubular AAO nanostructures and its biomedical applications

5.1 Introduction

Since the discovery of self-ordered porous alumina in 1995,[6] anodized aluminum oxide (AAO) has become one of the most popular periodic templates to create low dimensional materials such as nanodots, nanowires and nanotubes for various nanotechnology applications.[10, 104] More recently, some efforts have been made to utilize AAO as a material for implant surface coatings on Ti-based substrates for enhanced bone in growth,[105] stent coating,[106] and drug delivery[107] due to its pored structures together with the bio-compatible properties of aluminum oxide.

In addition to regular porous AAO[6, 12, 13, 15-19], various novel AAO nanostructures were reported in the literature[16, 44, 45, 49, 50] by utilizing modified anodizing parameters. These enhanced nanostructures could open up new opportunities for advanced device applications. Among these, alumina in a nanotube configuration is of particular interest due to its unique structure and outstanding materials properties.

In this chapter, we demonstrate that nanotubular AAO is obtained by a combination of HA technique and subsequent chemical etching process; individual separation of AAO nanotubes is achieved by chemical etching; and that selective opening and closing of the nanotube entrance can be accomplished with novel self-assembly processing.

In the aspect of biomedical application, it was reported that Al would stimulate iron-induced lipid peroxidation referred to as the oxidative degradation of lipids.[108]

Oxidative stress often cited as pathogenesis of Alzheimer's disease[109] made Al or Al containing materials less popular in biomedical applications although the biochemical mechanism and the relevance of Al effects are still controversial.

Aside from some of the controversial aspects, the research on various biomedical applications of porous alumina in a chemically more stable oxide form has increased tremendously in the past few years such as skin wound repair,[110] implant surface coatings on Ti alloys for bone cell growth,[105, 111] membranes for hemodialysis,[112] biofiltration,[113] cardiovascular stent applications,[106, 114] encapsulating enzymes,[115] drug delivery[116-118] and more. In regards to implant applications, AAO films can be seen as promising coatings for orthopedic implants due to nanoporous nature of AAO to mimic the dimensions and structural components of natural bone.[117] In terms of topographic effects on osteoblast cell or bone forming cell behavior, it has been shown that ceramics, such as nanoporous alumina, exhibit enhanced effects on cell growth rates and bone forming ability.[105, 119, 120]

As exemplary potential biomedical applications of periodically spaced-apart aluminum oxide nanotubes, we also demonstrate (1) enhanced osteoblast cell adhesion and spreading on nanotube configured AAO surfaces and (2) potential candidate for drug loading and controlled release vehicles particularly for orthopedic implant application.

5.2 Experimental procedures

5.2.1 Al foil pre-treatment

A 0.5mm thick annealed Al foil purchased from Alfar aesar (99.99%) was used as the starting material. The Al foil was successively degreased by acetone and isopropyl alcohol with ultrasonication followed by deionized (D.I.) water rinse and nitrogen gas blow. Double-side conducting Cu tape was then attached to the Al sample and insulating electroless lacquer (Miccroshield) was brush-painted over all the area to be immersed into anodizing electrolyte except the area to be anodized. The Al foil was slightly etched in 1M NaOH aqueous solution to remove any possible surface contaminations prior to electropolishing process conducted at 20V in a solution of perchloric acid (70%) and ethanol (99.9%) (1:4 volume ratio) at 5℃, using Pt counter electrode. A representative current vs. time evolution is shown in Figure 5.1 with a photograph.

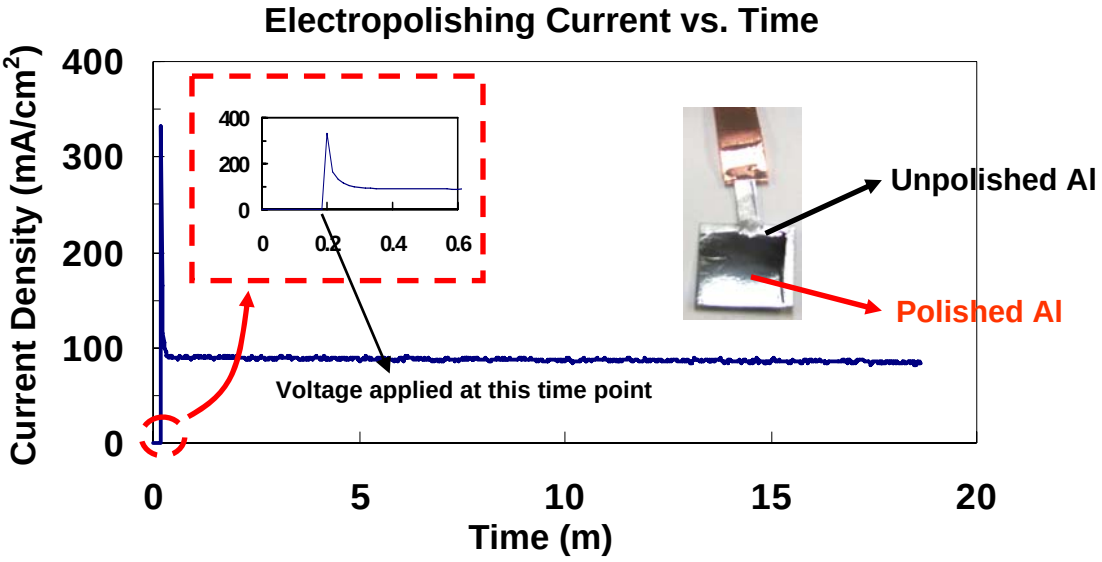


Figure 5.1: Typical current evolution with respect to electropolishing time. Inset shows current evolution at the initial reaction stage. A representative photograph clearly shows the mirror-like Al surface is achieved after process.

5.2.2 Anodization

To prevent non-uniform oxide growth during hard anodization, porous AAO (1~2μm thick) layer was formed first at 25V in 0.3M sulfuric acid, and then the concentration of electrolyte was diluted to 0.06M (for 35V anodization) and 0.01M (for 40V anodization), and the voltage was slowly increased from 25V to target voltage (V_T), and then was maintained at V_T with vigorous stirring to dissipate heat evolution arising from high current evolution until the anodization process was completed. The electrolyte temperature was maintained at 1℃ during both mild and hard anodization processes using a powerful refrigeration bath (RTE7, Thermo Scientific) in which the coolant circulates double-wall glass chamber. Power supply (Agilent; E3612A) was connected to a digital multimeter (Keithley; 2100) to monitor and record voltage/current evolutions.

5.2.3 Substrate transfer

After the anodization process, the top side of AAO layer was glued onto Si substrate using thermoplastic adhesive (crystalbond, Electron Microscopy Sciences) for ease of handling. The Al substrate that supported the AAO layer was then selectively etched and removed using a mixed HCl and $CuCl_2$ solution for a few tens of minutes until the reaction ended. The AAO barrier layer near the bottom of the anodized pores (now the top surface as the sample was mounted upside down on Si substrate) was then removed by pore widening chemical etch solution (5 wt% phosphoric acid). The microstructure was then examined under Scanning Electron Microscope (SEM; Phillips XL30 ESEM). Overall fabrication processes are schematically illustrated in Figure 5.2.

The Cr sputter deposition was performed using DC sputtering for a nominal thickness of ~5 nm.

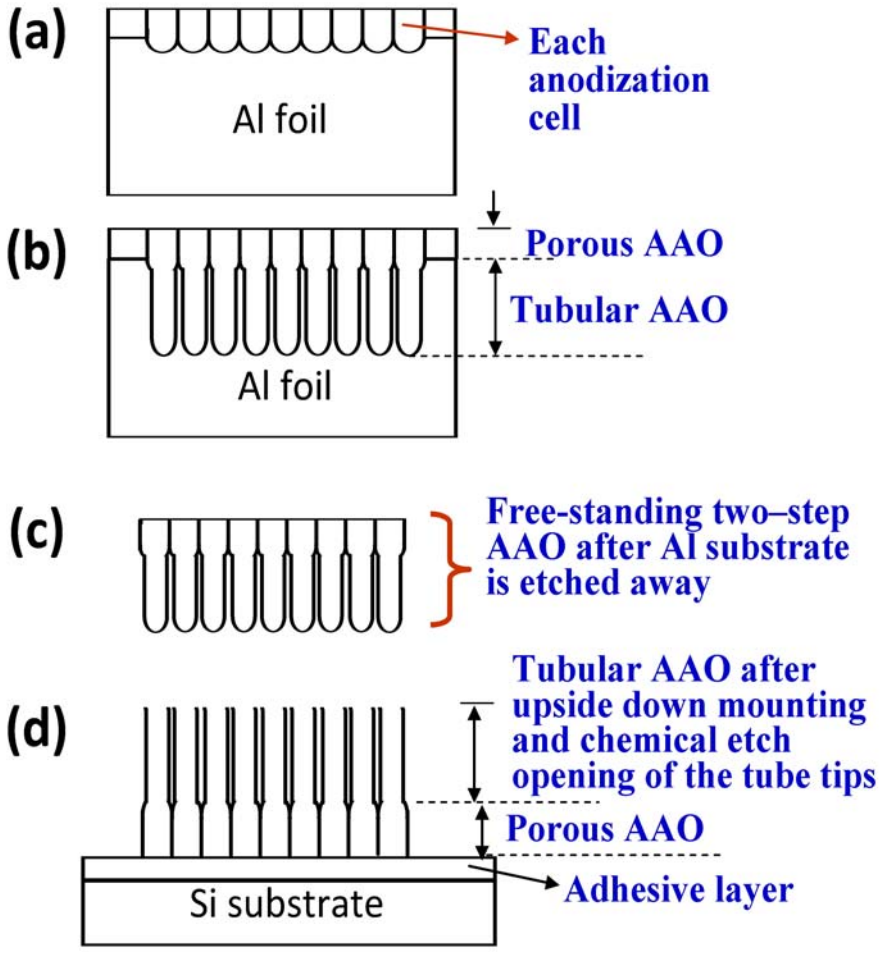


Figure 5.2: Schematic illustration of nanotubular AAO fabrication. (a) mild anodization to form porous AAO layer in 0.3M sulfuric acid, (b) hard anodization to form tubular AAO layer, (c) selective aluminum removal by etching in ($CuCl_2$+HCl) solution, and (d) attaching AAO upside-down on Si substrate and pore widening etch in 5wt% phosphoric acid.

5.2.4 Porosity and surface area calculation

In order to characterize the AAO nanotube film structure, a porosity and surface area calculation was carried out. A theoretical porosity can be computed geometrically based on structural parameters such as pore size and inter pore distance assuming ideal hexagonal arrangement. The following equation, (5-1), was used to approximate the porosity, *P*, of the samples,

$$P = \frac{2\pi}{\sqrt{3}}\left(\frac{r}{D_{\text{int}}}\right)^2 \tag{5-1}$$

where r is the inner pore radius and D_{int} is the inter pore distance. To determine the surface area of the samples with an area of 1cm^2, first the nanotube density was established based on SEM images by counting the number of nanotubes per field for a given area. The nanotube density, N, was $\sim 2.19\times10^{10}$ (nanotubes/cm^2). The following equation, (5-2), was used to approximate the surface area, *SA*, of the samples

$$SA = \left(2\pi\left(R^2 - r^2\right) + 2\pi h\left(R + r\right)\right) * N \tag{5-2}$$

where R is the outer tube radius, r is the inner pore radius, and h is the height or length of the film. This equation is based on the surface area of a tube multiplied by the number of tubes in the sample area. This is a theoretical estimation. It may be that the voids located around the center pore are not completely void the length of the tube,

nonetheless *SA* is dramatically increased based on the introduction of tubes on the surface.

5.2.5 Cell culture assay for adhesion and viability

For cell culture studies, MC3T3-E1 mouse osteoblast (CRL-2593, sub-clone 4, ATCC, USA) bone cells were used. Cell growth media consisted of alpha minimum essential medium (a-MEM; Invitrogen, USA) in the presence of 10% fetal bovine serum (FBS; Cellgro, USA) and 1% penicillin-streptomycin (PS; Invitrogen, USA). The cells were incubated under the standard 37℃, 5% CO_2 environment. When the concentration of the MC3T3-E1 osteoblastic cells reached ~ 3×10^5 cells/ml, they were seeded onto the substrate of interest (electropolished flat Al vs. AAO nanotube surface), which were placed individually in a 12-well polystyrene plate, and stored in a CO_2 incubator for 24 hours. The concentration of the cells seeded onto the specimen substrate was ~5×10^4 cells/well. Next, to observe cell adhesion, spreading, morphology, and viability of the attached cells, a fluoroscein diacetate (FDA) (Sigma) staining was conducted. The cells on the substrates were washed with 1XPBS (phosphate buffered solution pH 7.4, Invitrogen) and incubated for approximately 5 minutes with FDA stock (5 mg dissolved in 1 ml acetone) dissolved in 1XPBS (10μl/10ml), and washed once more. The samples were then inverted onto cover-slips, mounted, visualized and photographed using a green filter by a fluorescence microscope. (DM IRB, Leica Co., USA).

5.2.6 Antibiotic loading, release, and collection

Insertion of liquid into AAO nanotubes is not always easy as the surface tension of the liquid has to be overcome. At room temperature (25°C), the nanotube samples were placed in a vacuum (~0.1 mTorr) for approximately 5~10 minutes to rid nanopores of any trapped air. Approximately 1ml of 1% amoxicillin (Sigma) in PBS was loaded onto each sample placed individually in separate wells of a 12-well plate (Nunc). To ensure dissolution of the amoxicillin prior to loading, a few microliters of 1N HCl was added until the solution became clear. The samples were incubated overnight under vacuum to allow sufficient time for the drug to fully penetrate into the nanotube structure. The drug-loaded nanotube samples were washed 3X with ice cold PBS (to restrict diffusion from the reservoir). Next, the samples were individually placed in new wells (Nunc, 12-wells) incubated in a humidified 95% air/5% v/v CO_2 incubator at 37℃ in 1ml fresh simulated body fluid (PBS was used in this study). The solution was collected at hourly time points initially (hours 1~6) and daily time points thereafter (up to day 35 or 5 weeks) and 1ml fresh PBS was added after each collection. Drug concentration was determined by measuring the absorbance of the fluid using a UV-VIS spectrophotometer at λ = 230nm (Biomate_3, Thermo Electron, Madison, WI). The assay was calibrated by use of PBS blanks and a standard curve was determined up to 2mg/ml amoxicillin. Three replicates per experimental sample for each time point were measured and the average values ± standard error (SE) was graphed to obtain release profiles, release rate, accumulation, and release kinetics.

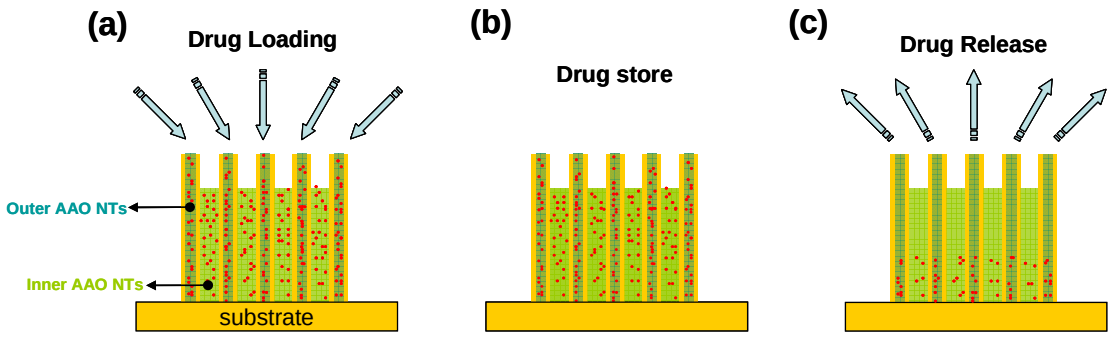


Figure 5.3: Schematic concept of drug loading and release. (a) drug loading, (b) drug store and (c) drug release. Drug can be stored for certain amount of time or released immediately when necessary.

5.3 Results and discussion

5.3.1 Nanostructure evolution

Conventional mild anodization (MA) for AAO formation is associated with a relatively low current density over the entire anodizing period, but there is an initial current jump followed by a rapid drop within a few tens of seconds at the beginning stage. In the case of hard anodization (HA), however, large amount of current flows at the beginning and it is slowly decreased over the anodizing time span as shown in Figure 5.4. High current during HA process ensures not only fast AAO film growth but also highly ordered AAO cells, as will be discussed later. However, it is worthwhile to mention that samples should be pre-anodized in MA condition to produce a certain thickness of porous AAO film layer prior to HA. Otherwise, undesirable local oxide thickening or dielectric breakdown can readily occur during hard anodization.

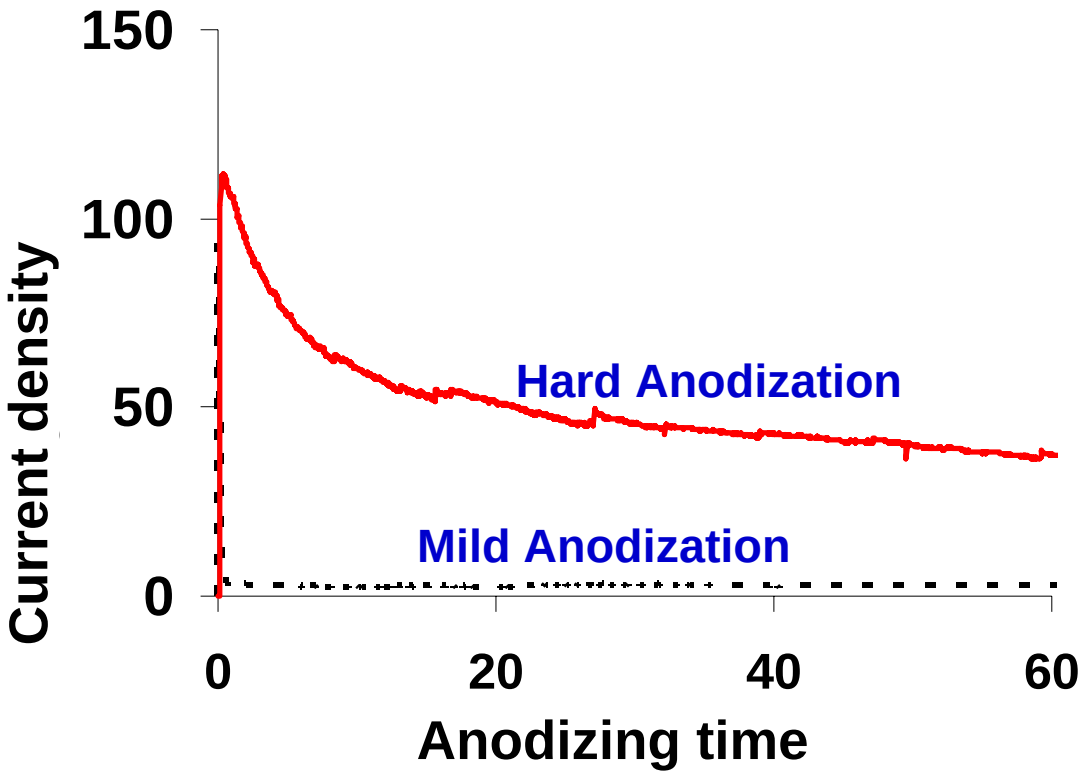


Figure 5.4: Representative anodic current changes during anodization experiments. Mild anodization (black dot line) was conducted at 25V in 0.3M sulfuric acid at 1℃, and hard anodization (red solid line) was conducted at 40V in 0.01M sulfuric acid. Mild anodization for 30 minutes led to the porous AAO structure which was used as the basis to start the subsequent hard anodization.

The SEM micrographs in Figure 5.5 compare conventional porous AAO and newly obtained nanotubular AAO by hard anodization and nanotube tip etching. In the case of conventional porous AAO, hexagonally ordered AAO pores are vertically grown in the underlying Al substrate under the well-known self-assembly condition. The pore channels are straight and parallel to each other, and the bottom of each vertical pore is closed with hemispherical end that forms continuous oxide layer over the whole

anodized area, which is known as a barrier layer[1] as indicated in Figure 5.5(a). The SEM image in Figure 5.5(b) represents the top view of upside down barrier layer for the porous AAO sample after mild anodization with 0.3M sulfuric acid at 25V. The porous AAO structure after the barrier layer is removed is given in Figure 5.5(b).

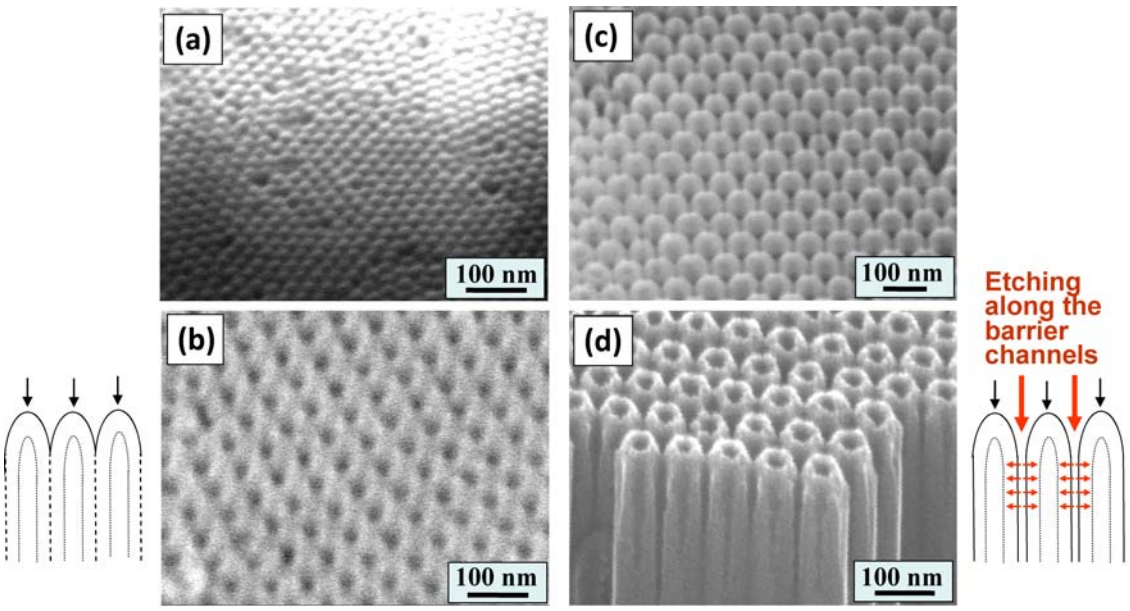


Figure 5.5: SEM images showing; (a) Top view of upside down barrier layer for the porous AAO after mild anodization with 0.3M sulfuric acid at 25V, (b) Porous structure after the barrier layer is removed, (c) Top view of upside down tubular AAO right after hard anodized at 0.01M sulfuric acid 40V. (d) Top view SEM after the nanotube tip is etched away and the tubular geometry is realized. The schematics for porous AAO formation mechanism is presented on the left of image (b) while the mechanism of nanotube formation is illustrated by the schematics on the right side of image (d).

In the case of hard anodization, the barrier layer exposed after the Al substrate removal contains a significant depth of recessed voids, which were formed at between-cell triple junctions as shown in Figure 5.5(c). The image of Figure 5.5(c) was obtained by hard anodized at 0.01M sulfuric acid 40V. The SEM image in Figure 5.5(d) is obtained after the nanotube tip is etched away and the tubular geometry is realized. The mechanisms of microstructural formation for porous AAO vs. alumina nanotubes are schematically illustrated on the left of image (b) and on the right side of image (d), respectively.

The void structure in Figure 5.5(c) appears to play a significant role in the separation of neighboring AAO nanotubes from each other during pore-widening chemical etching as is seen in Figure 5.5(c) and (d). Voids were often observed at the triple cell junctions especially after the hard anodization. Possible mechanisms for void formation were proposed by several groups,[17, 25, 50, 55-59] which can be summarized as follows: (1) electrochemically unfavorable oxygen gas formation and their entrapment along cell boundaries during fast AAO growth, (2) compositional difference between inner and outer pore wall which can lead to different dissolution rate in pore widening solution, (3) lower density at triple cell junction due to repulsive force arising from volume expansion during hard anodization, and (4) accumulated compressive stress along the cell boundaries, and combination of the above. We presume that our nanotube structure formation is based on one or more of these mechanisms. By virtue of the existence of void channels, pore widening solution could now penetrate through void channels and, therefore, could etch the outer pore walls helping to completely separate the nanotubes from each other. The etching of inner wall of the AAO cell was retarded due to the closed configuration of barrier layer at the

beginning of pore widening treatment. Later when the nanotube tip is dissolved away, the etching solution could wet inner pore walls and start etching the walls. (see the schematic illustrations in Figure 5.5).

Our well-separated nanotube array structure could be attributed to different dissolution rates of inner vs. outer pore walls due to their compositional difference. In addition, the presence of the barrier layer covering the nanotube-tip (after removing the Al substrate material) delays the inner wall etching while outer pore walls are continuously being etched through void channels at the triple junctions from the very beginning of the chemical etching, which makes it possible to obtain a good nanotube separation from each other.

Highly ordered AAO nanotube formation as reported in this paper could be associated with high current evolution, directly related to high electric field across barrier layer near the pore bottom. The current density during anodization is dependent on various parameters and the applied electric field, i.e.,

$$j = j_0 \exp(\beta E) \tag{5-3}$$

where both j_0 and β are temperature- and material-dependent parameters and E is the effective electric field.[20]

Another interesting observation regarding AAO nanotubes obtained in this paper is that we can obtain high aspect ratio (diameter to length) AAO nanotubes of greater than ~1,000. Some of the loose nanotubes in Figure 5.6 and Figure 5.7 indicate that the AAO nanotubes can have robust mechanical properties as individual nanotubes can be seen bent or curved without fracture. Because of the dielectric nature of Al_2O_3

nanotubes, there is some electron charging effect during SEM examination, which makes the image slightly blurry at high magnification, Figure 5.6(b). The sample was anodized at 40V using 0.01M sulfuric acid, followed by chemical etching by immersing in the mixed $CuCl_2$ + HCl solution for 4h at 20℃ for removal of Al substrate. A pore widening etching treatment removes the barrier layer and reveals the nanotube geometry. Figure 5.7 shows the low and high magnification SEM images of the AAO nanotubes, respectively.

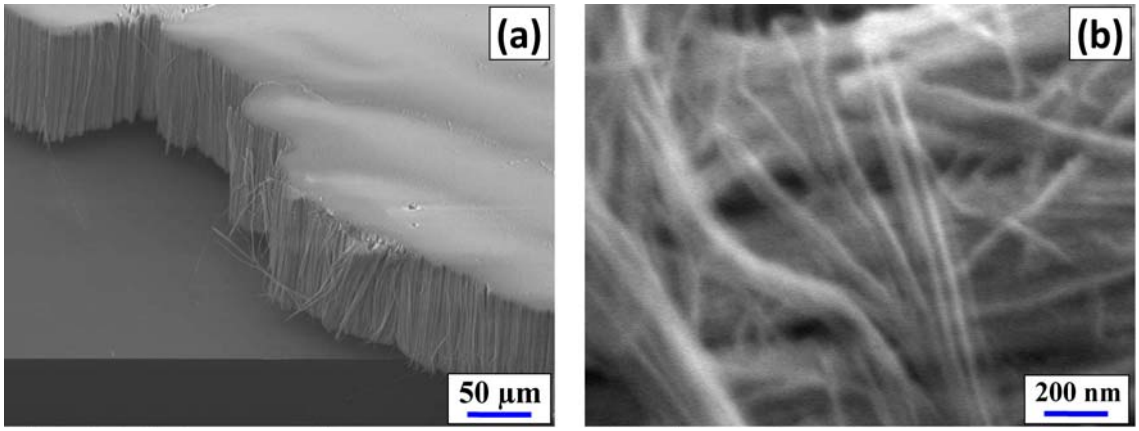


Figure 5.6: SEM image of free standing AAO nanotubes placed on Si substrate (after removal of Al substrate), (a) low and (b) high magnification, respectively. Some of the loose nanotubes indicate mechanical robustness as they can be bent without fracture.

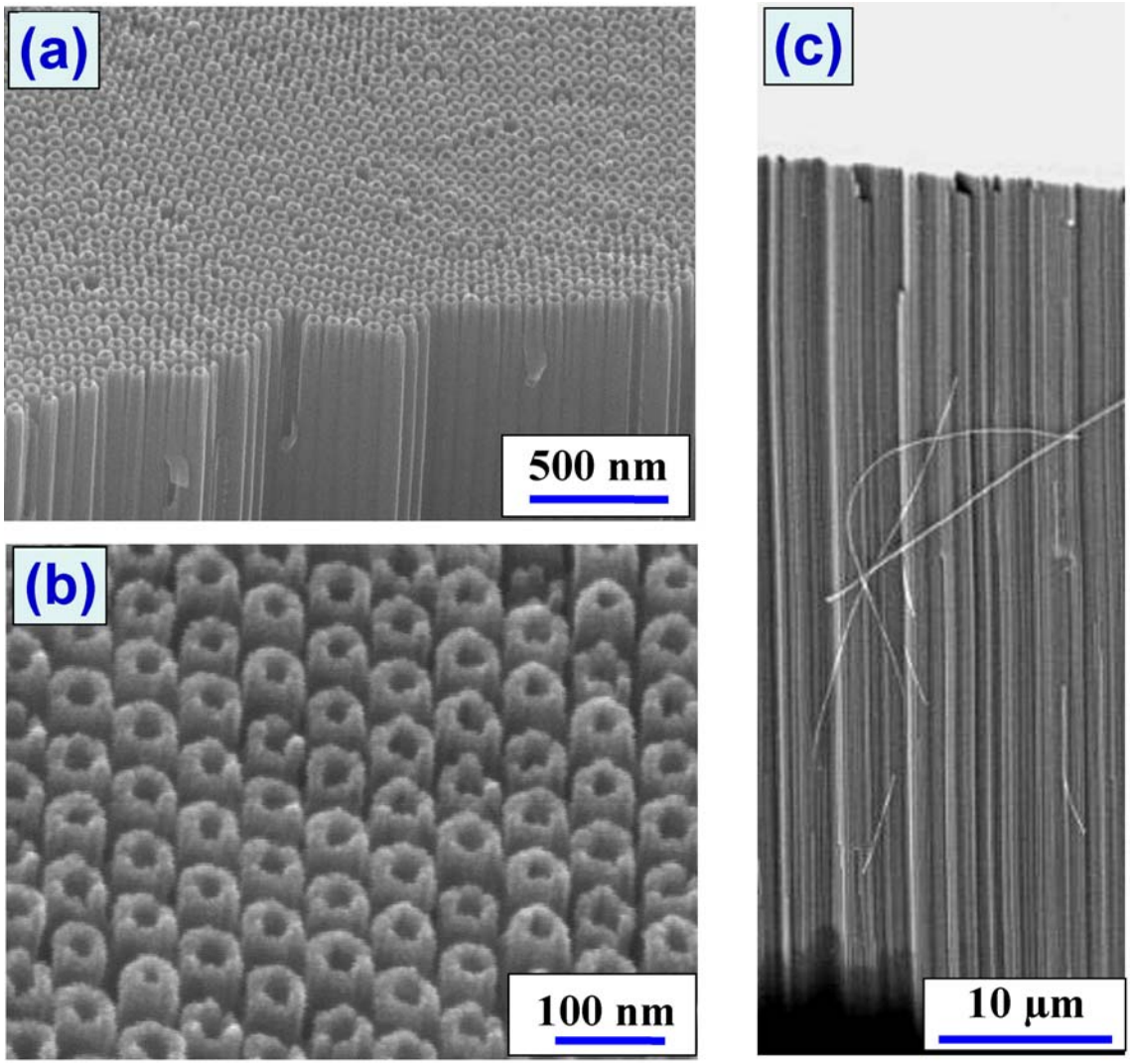


Figure 5.7: Oblique view SEM image of vertically aligned periodic AAO nanotubes. (a) Low magnification image, (b) high magnification image showing the nanotube and hole dimension, (c) cross-sectional SEM showing the aligned nature of the AAO nanotubes and an example bent (mechanically flexible) behavior of a separated individual alumina nanotube. Highly ordered hexagonal arrangement was obtained by hard anodization (at 40V with 0.01M sulfuric acid), followed by chemical etching in 5 wt% phosphoric acid.

In previous research described in the literature, various attempts have been made to obtain individual Al_2O_3 nanotubes, for example, by using atomic layer deposition of aluminum oxide material on organic nanowires,[121] partial chemical dissolution and ultrasonic vibration of porous AAO,[122] and hydrothermal synthesis.[123] However, these methods to obtain isolated AAO nanotubes are somewhat complicated and have various processing and structural limitations when high aspect ratio nanotubes are needed. Our hard anodization based approach is a convenient technique for fabrication of alumina nanotubes having uniform tube diameter and tailored tube length. It would be interesting to take these individual Al_2O_3 nanotubes for mechanical property evaluations and related nanomechanics studies.

The Al_2O_3 nanotube arrays that we have fabricated exhibit a uniform and reproducible dimensions, and a quite high aspect ratio (diameter of ~80 nm, height of ~100 μm, aspect ratio >~1000). The SEM micrographs in Figure 5.7(c) clearly indicate the high aspect ratio. It is also seen that the Al_2O_3 ceramic nanotubes, if individually separated, can be mechanically flexible. Such a flexible nature can be useful for utilizing the Al_2O_3 nanotube array as a component of tactile shear sensors for robotics, air of fluid flow sensors and security sensors similarly as with carbon nanotube shear sensors.[124, 125] These aligned Al_2O_3 nanotubes can be surface metalized with highly conductive metals or magnetic materials, e.g., by sputter deposition or atomic layer deposition, for various other applications such as electron field emitters, electrical interconnects, and sensors and actuators.

Such high-aspect-ratio nanotubes provide a very large surface area, especially since both the inside and outside diameter surfaces can be utilized, which is not the case for simple AAO pore structures. The large surface area can be exploited for enhanced

catalytic reactions (if surface-coated with a very thin catalyst material such as Pt), and can assist in increasing the amount of drug molecules adsorbed on the surface. Together with the large empty space within the nanotube pores as well as the space between the nanotubes in the high-aspect-nanotube bundles, this can be useful for storage of drugs and other chemicals for controlled slow release, similarly as for the vertically aligned Si nanowire array structure.[126]

5.3.2 Cell culture assay for adhesion and viability

In terms of topographic effects on bone cell (osteoblast) behavior, it has been shown that ceramics, such alumina, with textures on the nanoscale, created by AAO, exhibit enhanced effects on growth rates and bone forming ability.[105, 119, 120] For cell growth and proliferation for various biomedical applications such as tissue engineering, bone growth, stem cell differentiation control, an important first step is for the cells adhere strongly on the substrate. Such strongly adhered/anchored cells are likely to function more actively and proliferate better. Nanostructured architecture of this nature can be used in various biological applications, such as implant surface coatings for enhanced cell activities. It is well known that the oxide layer on metallic implants is responsible for the bone bonding and natural bone integrating characteristics of orthopedic implants.[127] Therefore new research aims have recently been geared toward optimizing these properties to promote enhanced osseointegration [128] by modifying and improving this oxide layer. Oxide nanostructures such as vertically aligned nanotubes can provide significantly enhanced osteoblast cell adhesion and bone growth, for example, TiO_2 nanotubes near the dimension of 80 ~ 100 nm diameter.[79, 129] Therefore, we have also investigated the potential use of our alumina nanotube

array structure as an implant surface coating by employing an *in vitro* cell adhesion assay. Shown in Figure 5.8 are comparative osteoblast (bone) cell adhesion images for flat Al_2O_3 control substrate (Figure 5.8(a)) vs. Al_2O_3 nanotube arrays (Figure 5.8(b)). A fluorescein di-acetate (FDA) viability marker was used to stain the cytoplasm of osteoblast cells cultured on the different surfaces.

Osteoblast (bone) cell adhesion after 24 hours of culture time is much more pronounced on the Al_2O_3 nanotube substrate compared to a flat Al_2O_3 control substrate, and it is evident that the cell adhesion and spreading is significantly enhanced on the nanotube surface. These primary studies suggest that the AAO nanotube surface used as a possible orthopedic implant surface is an attractive template for improving the osteoblast response. The AAO nanotube surface, with a wide array of configurations, sizes, and shapes, can be useful for parallel experiments looking further into osteoblast response, functionality, and matrix production for improved osseointegration. The oblique-view SEM image of vertically aligned, highly periodic AAO nanotubes used for the osteoblast cell culture is shown in Figure 5.8(c). The nanotube sample was anodized at 35V using 0.06M sulfuric acid. The pore widening treatment was conducted with 5 wt% phosphoric acid at 20℃.

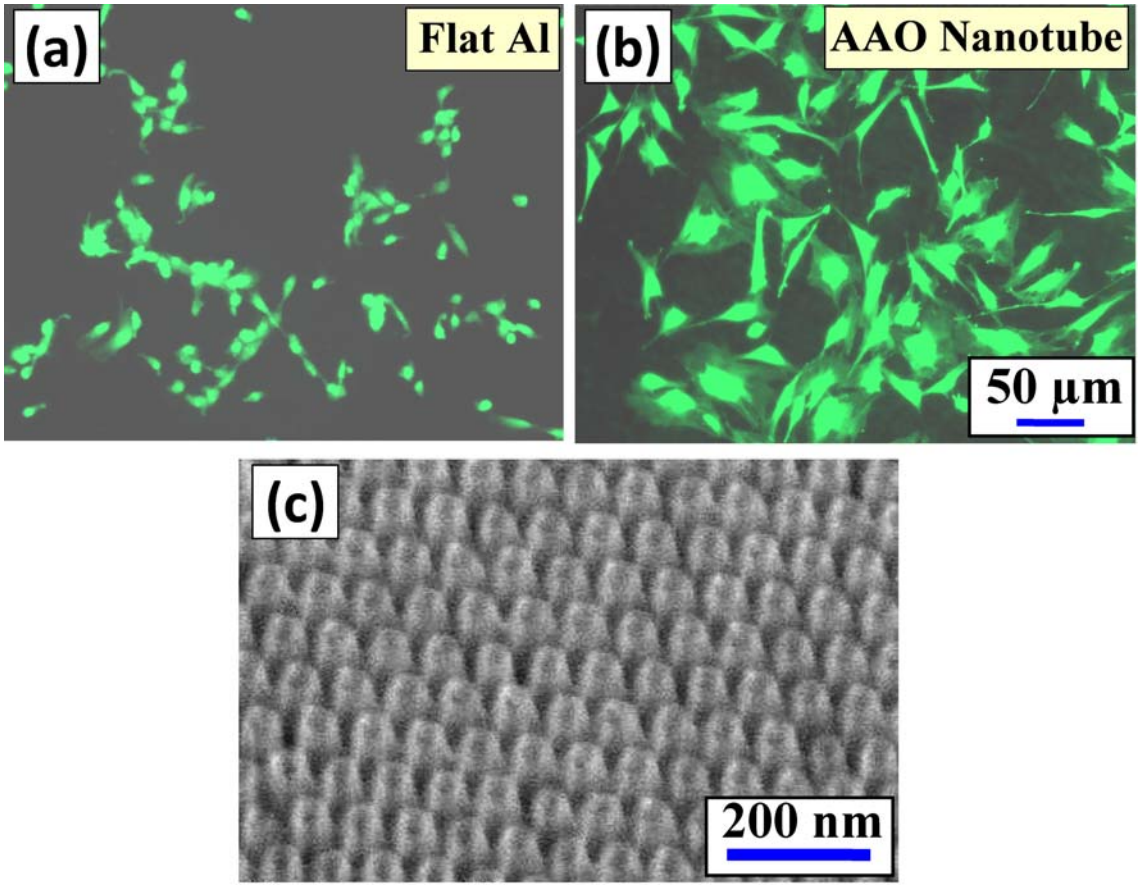
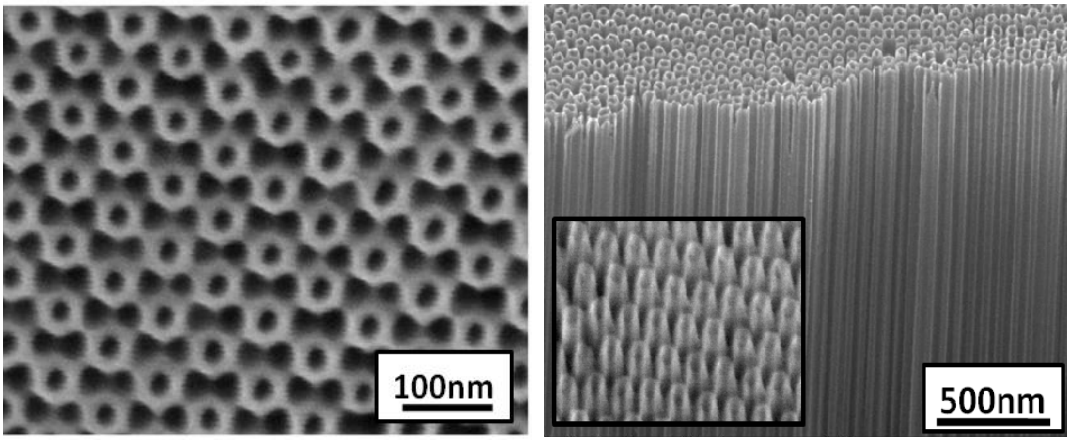


Figure 5.8: Osteoblast (bone) cell viability determined by FDA (live fluorescent staining, green color) after 24 hours of culture time (a) on flat Al_2O_3 and (b) on Al_2O_3 nanotubes. Clearly, the cell adhesion/spreading are significantly enhanced on the nanotube surface. (c) Oblique view SEM image of vertically aligned highly periodic AAO nanotubes for cell culture.

5.3.3 Drug loading and release

The vertically aligned, periodic AAO nanotube structure used as a drug carrier is illustrated in the scanning electron microscopy (SEM) images in Figure 5.9 (top row). In contrast to conventional AAO nanopore structures, AAO nanotube unit cells are separated from each other while being loosely connected to each other, which is an interesting feature. In our nanotube samples, the nanotube center pore size (~20nm) is

practically the same as the size of the voids (spacing between adjacent nanotubes) surrounding the center pore. This makes our AAO nanotube structure favorable due to larger surface area in terms of loading drugs or catalyst chemicals into the AAO nanotubes. The equal size of the center pore and voids was achieved by the relatively low anodizing voltage (35V) which ensures both relatively small center pore size and interpore distance compared to the higher voltage evolution under the constant current anodization technique conducted by Zhao et al.[50]



Film Thickness, Wall Heigth (μm)	Pore size (nm)	Wall Thickness (nm)	Interpore Distance (nm)	Porosity (%)	Surface Area (cm^2)
38	20	15	73/42/36*	25.1	1830

Figure 5.9: Top row: bottom view, cross-sectional view, and oblique angle (inset) SEM images of AAO nanostructures used as drug carriers showing a vertically aligned, periodic nanotube films. Bottom row: Chart describing the details of the physical dimensions of the nanotube films. Note that values in the asterisk is the distance of center to center hole, center hole to surrounding void distance, void-to-void distance, respectively.

This is the first study to utilize the AAO nanotube structure for applications in drug elution. The nanotube film shows a highly ordered and uniform nanotube morphology and long-range order with nanotube height reaching ~38μm, which is the tallest used thus far in nanopore/nanotube ceramic alumina and titania drug elution studies. Physical details of the AAO nanotubes are portrayed in the chart shown in Figure 5.9 (bottom row). One of the advantages of our nanotube structure is the increased porosity (~25%) and the high surface-to-volume ratio. Here we show the surface area is increased by three orders of a magnitude by introducing the nanostructures on the surface, where a 1×1 cm^2 sample has perceivably $1830 cm^2$ of surface area. The interstitial spaces between the tube walls and the inner pore walls aid in this calculation. Another benefit to our AAO drug release system is that we can design the nanotubes to match a desired pore size, structural shape, available porosity, and surface area which can help tailor to specific implant needs and controlled release.

Factors such as adsorption properties (interactions between drug and matrix), pore size, pore connectivity, and pore geometry are just a few of the aspects to take into account when designing a controlled drug delivery system. It has been suggested that during AAO fabrication, stress cracking and other residual defects due to the oxidation volume expansion (Al becoming Al_2O_3) may be present and these imperfections can leave charges on the surface, such as Al^{3+} and O^{2-} [14]. For the purposes of drug loading, this may aid in electrostatic adsorption of the drug molecules and help concentrate the drug within the nanotube "depots" so to speak.

For this study, amoxicillin (AMX), a common pharmaceutical antibiotic, is used as a model drug in the following AAO drug elution studies. The size of the AMX molecule is ~0.8nm,[130] a reasonable size to enter and fill the 20nm diameter pores

and interstitial spaces in between the nanotubes. Preoperative oral administration of AMX has been proven to reduce the risk of implant failure,[131, 132] and local delivery of AMX during orthopedic surgery reduced the infections associated with open fractures,[133] compound limb fractures,[134] and with osteoinductive and osteoconductive bone-graft substitutes.[133] As well, local delivery of antibiotics was effective in reducing vascular infections from staphylococcal strains.[135] It can therefore be hypothesized that localized AMX elution from both orthopedic and vascular implants would be highly advantageous. With the more advanced drug delivery, controlled release system such as AAO nanotubes on implants, would help make improvements in delivery efficiency and localization which may also provide a solution for reducing dosages and help minimize toxic side effects and drug waste.

In terms of controlled release, it was found that the AAO nanotubes were cable of carrying cargo molecules (AMX, a small drug molecule) and releasing them in a physiological environment of the simulated body fluid, phosphate buffered solution (PBS). There are several types of controlled release devices and the AAO nanotube system presented here can be considered a drug diffusion-controlled release, where the entrapped drug diffuses out of a matrix at a defined rate.[136] An antibiotic release profile from the AAO nanostructures filled with AMX was obtained for over 5 weeks (35 days), illustrated in Figure 5.10. For a control experiment, electropolished aluminum, without a nanostructured surface, showed almost zero antibiotic release as expected (data not shown). This indicated that it was the nanotube design on the surface which created a reservoir for the AMX that was responsible for the drug release. Figure 3 shows the total amount of amoxicillin released as a function of time. A near steady release profile is achieved after the first week of release (after Day 7). The ideal release

profile for most drugs would follow this type of a steady release rate so that the drug levels in the body remain constant while the drug is being administered.[137] The drug elution from the AAO nanotubes accomplishes the primary objective of a controlled release device which is to provide a sustained release for long periods of time on the order of days, weeks, even months.

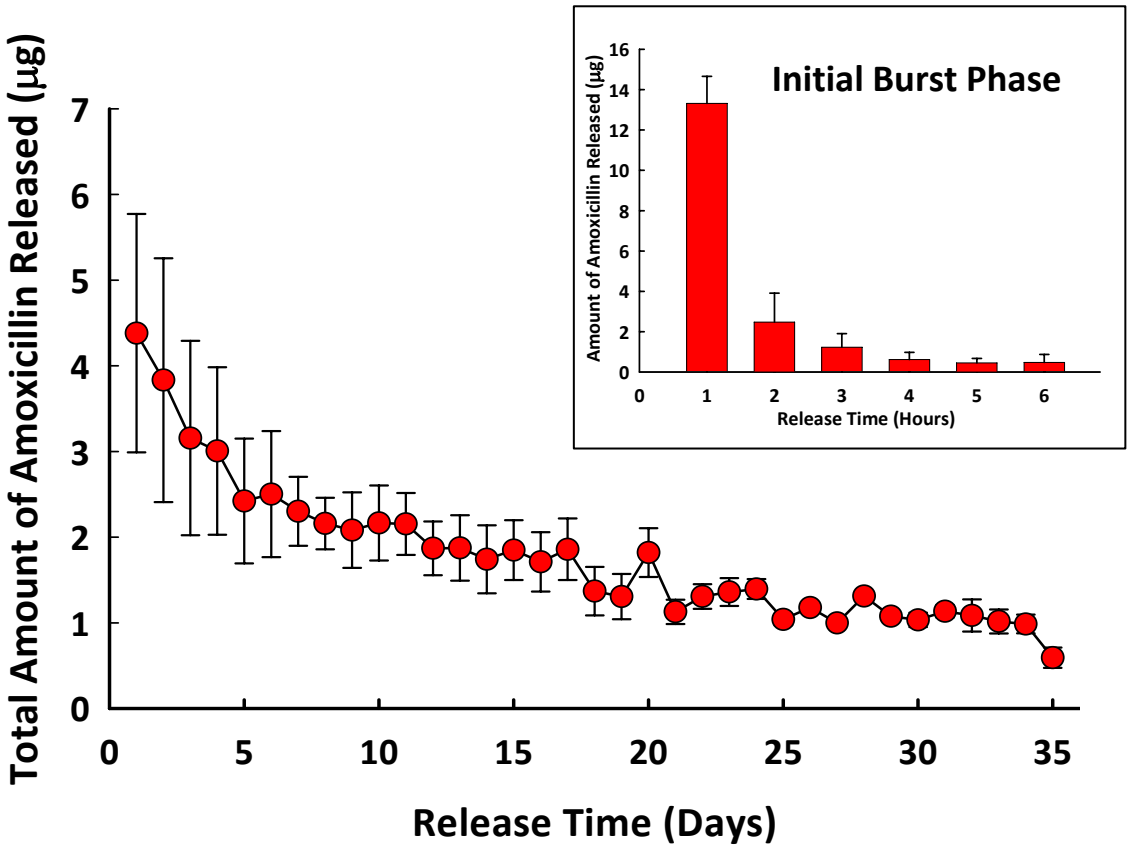


Figure 5.10: Absolute release rates of amoxicillin as a function of sampling time for the AAO nanotube drug carriers. The initial burst of drug from the surface is shown in the inset. The graphs show the mean ± SE (n=3).

In the inset graph of Figure 5.10, which shows the initial release of drug from the nanotubes in the first 6 hours of release, the highest "burst effect" is in the first hour with ~13μg of drug release. The "burst effect" is often seen as controversy as to whether this is due to near-surface entrapped drug or surface-absorbed drug.[138] The initial burst and release of drug from the nanotubes may be related to several factors including (1) high relative top surface area (2) increased drug diffusivity through tube walls/channels and (3) high porosity. In addition, the specifics of the pore dimensions and their uniformity as well as subtle difference in physical form of the nanotubes may play a role at release during the initial short term release (first 7 days) before the steady elution (beyond 7 days in Figure 5.10). At this stage in release, the drugs are being released from the top portion of the film where the so called "matrix surface" becomes a factor. After seven days, however, it is suggested that the drugs are traveling from a distance that is farther down in the matrix and less likely to be affected by the very top surface.

To further characterize the AMX release from the AAO nanotubes, Figure 5.11 illustrates the accumulative release (showing daily and weekly accumulation) and release rate per day over the 5 week elution study. A near steady release rate occurred over the course of the 5 weeks. This type of release would help maintain a drug level in a therapeutic window, avoiding the extremes of systematic drug over-dosages or under-dosages, eliminating the risks of adverse effects, drug waste, or being sub-therapeutic.

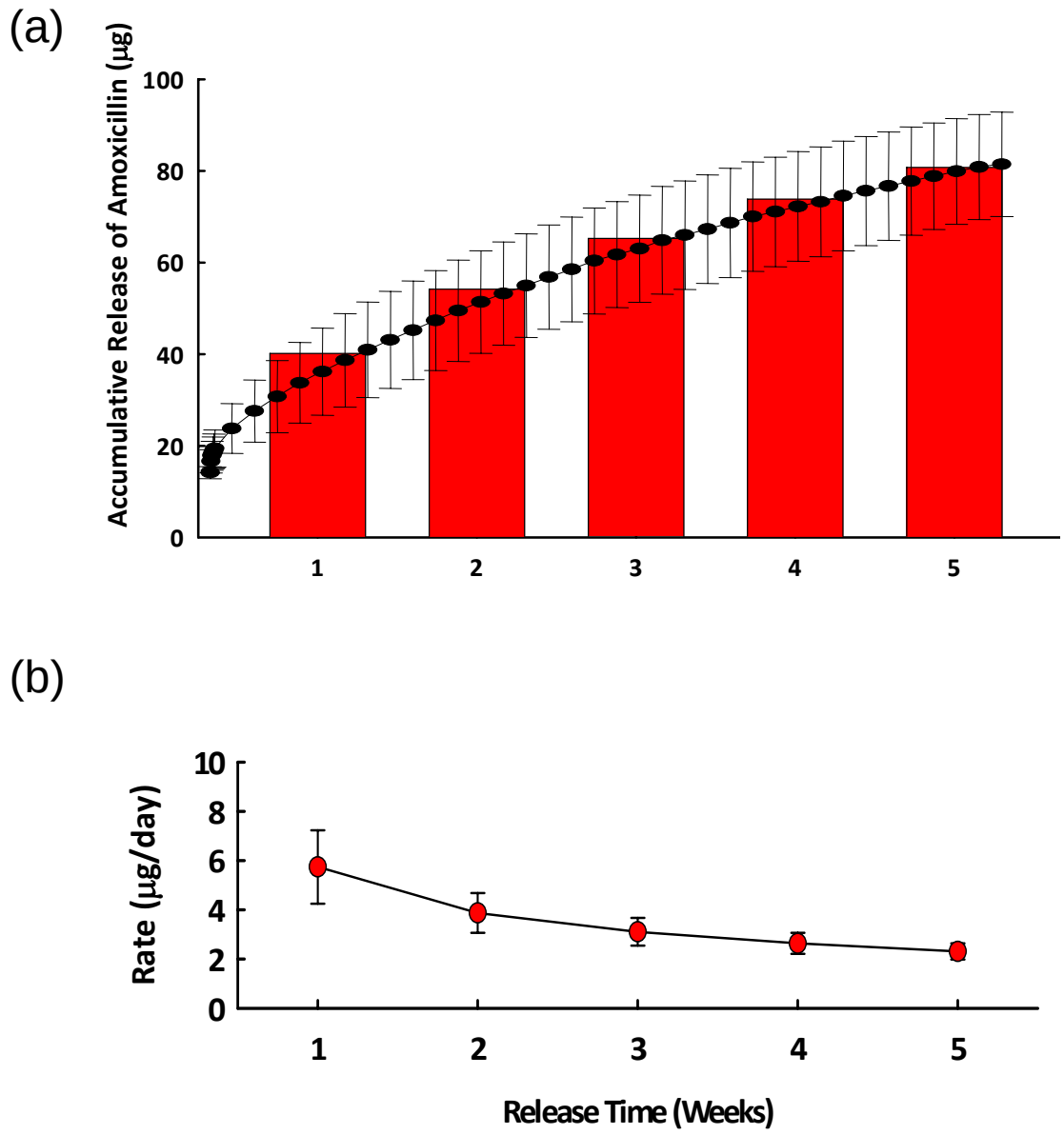


Figure 5.11: (a) Accumulative amoxicillin released as a function of time and (b) release rate per day vs. time. The graph shows mean ± SE (n=3). In (a), the dotted line reveals the daily accumulation over time and the bars represent the average accumulation per week. In (b), release rate is normalized per weekly time point.

When studying the drug release of molecules that have a size regime on the same scale as the matrix features, the basic principle of diffusion as a mixing process with solutes free to undergo Brownian motion in three dimensions may not necessarily apply, in at least on dimension, for the AAO nanotubes because the solute movement is physically constrained by the nanotube walls.[139] The AAO nanotube geometry may impose a rate limiting condition due to the length of the nanotube walls, because the length dictates how far the solute molecules have to travel to be released from the reservoir. While it is not possible to draw significant conclusions without varying the wall height of the AAO nanotubes, this in part will form some of our future work.

Many studies have observed that the release rate of a drug dispersed in a solid matrix (with no erosion of the matrix occurring) is proportional to the square root of time, as predicted by the Higuchi model.[140-142] It was determined that this was because the release rate is inversely proportional to the distance the drug must travel within the matrix to the matrix surface, since the diffusion distance increases with time, the release rate decreases with time.[140] The Higuchi equation follows,

$$\frac{Q_t}{Q_\infty} = k\sqrt{t} \tag{5-4}$$

where $\frac{Q_t}{Q_\infty}$ is the cumulative fractional release at time t and k is the release constant.

To identify the release rate mechanism and model the drug transport in the AAO nanotube system, the hypothesis was made that the release data obtained could be fitted using Eq. (5-4) and the results are given in Figure 5.12, where the fractional AMX release was plotted versus the square root of time. A near perfect linear fit was

observed, demonstrating that the drug kinetics approximately follow the square root of time relationship. The mechanism of release is most likely attributable to a novel constrained diffusion mechanism provided by the AAO nanotube walls.

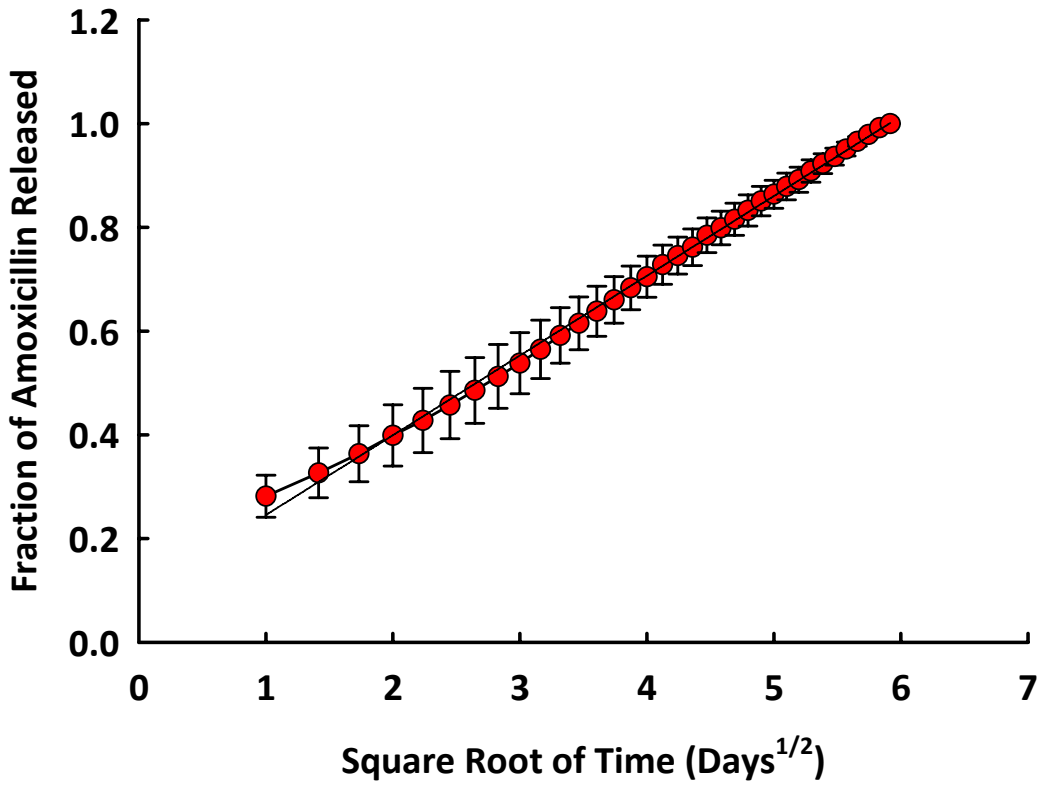


Figure 5.12: Plot of fractional release versus the square root of time representing a near perfect linear fit ($y = 0.154x + 0.092$, $R^2 = 0.998$).

AAO films are simple to prepare and can be easily modified and structurally tailored. As well they are resistant to most physiologic and chemical reactions (bioinert), mechanically strong, and are considered biocompatible *in vitro* and *in vivo*. By utilizing AAO nanotubes as drug carriers, a variety of drugs can be loaded into the device reservoir in a range of physical states, including solutions and crystalline or micronized suspensions.[139] This flexibility with respect to encapsulated drugs provides options to substantially increase the load dose and duration of therapy, as well as stability of drugs that are unstable in certain biological fluids or different biochemical/acidic/alkaline environments. AAO films are structurally robust and will not swell or change its porosity under different pHs or temperatures.[143] Thus, AAO nanotube drug carriers can be used to address the problems associated with conventional drug therapies such as limited drug solubility, poor biodistribution, lack of selectivity and unfavorable pharmacokinetics.[144] Lastly, the potential for AAO nanotube arrays on implant surfaces will help mimic the complex geometries of natural tissue and will provide a porous template for the growth and maintenance of healthy cells and tissue,[145] aiding in implant design as well as local delivery of therapeutics.

5.4 Summary

Highly hexagonally ordered, vertically parallel aluminum oxide nanotube array was fabricated via hard anodization technique. Due to the high-current anodizing process, noticeable voids are formed along the AAO cell boundaries located at triple cell junction, which enhances the separation of adjacent nanotubes during pore widening process.

The Al_2O_3 nanotube arrays so fabricated exhibit a uniform and reproducible dimension, and a quite high aspect ratio of greater than ~1,000. The nanotubes appear to be mechanically flexible. Such high-aspect-ratio, mechanically robust, large-surface-area nanotube array structure can be useful for many technical applications including shear tactile sensors, efficient catalyst supports, chemical reactant releasing materials, and drug storage and slow release biomedical devices.

The controlled release of amoxicillin from anodic alumina oxide (AAO) nanotubes was investigated. The unique AAO nanotube morphology was fabricated using a simple two-step anodization process that resulted in highly uniform, structurally robust nanotubes. This is the first study utilizing the AAO nanotube geometry as a drug carrier and the diffusion characteristics including a drug release profile, drug accumulation plot, and release rate were acquired. The AAO nanotube carriers demonstrated controlled, sustained release of common antibiotic, amoxicillin for approximately 5 weeks. This study illustrates the potential advantages of using AAO nanotubes as a unique alternative in terms of therapeutics concepts for implant surface coatings.

5.5 Future work

Factors affecting sustained release of drugs or catalyst molecules from the AAO nanotubes include the physical dimension of nanotube storage space such as diameter, length and surface area as well as the surface chemistry of platform and its interaction with the stored material itself. Alteration of the nanotube pore entrance dimension could also be important, for example, an intentional partial blockage of the nanotube pore

entrance can be contemplated using a deposition of organic or inorganic material to reduce the diffusion rate of drug release. Shown in Figure 5.13(a)-(c) is an example manipulation of nanotube pore entrance dimension by processing approaches. The pore-widening process for the AAO nanotubes opens up the nanotube tip completely as shown in Figure 5.13(b). Of course a partial nanotube tip opening can be obtained by shorter time pore-widening treatment so as to provide a smaller-diameter nanotube entrance, which would certainly enable a slower-rate, time-extended drug release. Alternatively, a post deposition of additional material onto the open nanotubes can be utilized to partially or completely block the nanotube entrance. An example is shown in Figure 5.13(c) where it is shown that the use of chromium sputter deposition can lead to the intentional blockage of the nanotube entrance. The amount of Cr sputtering can be adjusted to achieve any desired nanotube pore entrance dimension for selected drug release rate. Therefore, further studies on the effect of pore entrance size as well as physical dimensions of AAO nanotubes and surface chemistry needs to be pursued in the future.

Chapter 5, in full, is a reprint of the material as it appears in Journal of Materials Research, 26(2), 186 (2011) written by Kunbae Noh, Karla S. Brammer, Hyunsu Kim, Se-Yeon Jung, Tae-Yeon Seong, and Sungho Jin; and as it was accepted for publication in Journal of Biomaterials and Nanobiotechnology written by Kunbae Noh, Karla S. Brammer, Chulmin Choi, Seung Hyun Kim, Christine J. Frandsen, and Sungho Jin; and The dissertation author was the primary investigator and author of both these papers.

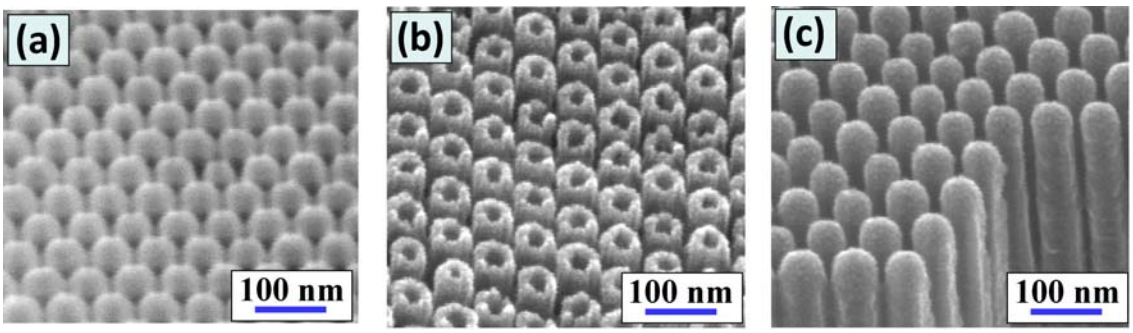


Figure 5.13: SEM images of vertically aligned periodic AAO nanotubes: (a) As hard-anodized, tip-closed nanotube geometry, (b) after chemical etching to open the nanotube tip, and (c) after additional Cr sputter deposition to intentionally re-close the nanotube entrance. An intermediate, partially blocked nanotube structure is obtained if the sputtering time is reduced.

CHAPTER 6: Overall Summary, Conclusions, and Future Work

In this thesis, various aspects of periodic nano-arrays have been discussed including preparations, properties and applications of anodized aluminum oxide (AAO) and PS-b-P4VP (S4VP) di-block copolymer self-assembly.

First, long-range ordered AAO arrays consisting of periodically modulated pores or nanotubes through guided anodization method have been demonstrated. Nanoimprint lithography (NIL) process allowed a faithful pattern transfer of the imprint mold pattern onto Al thin film, which is served as pore initiation sites in the subsequent anodizing process. Self-healing and pattern tripling phenomena were observed, which could be applicable towards fabrication of the NIL master mold having highly dense pattern over large area. Such a periodic arrayed nanostructure could be useful for fabrication of a large-area substrate for predictable positioning of arrayed electronic, magnetic or photonic devices, for enhanced biomedical applications, or for preparation of nanotube-shaped imprint stamps. In addition, a low-temperature deposition technique to produce sub-nanometer flatness in the Al film was devised for improved indentation pattern transfer and anodization, which is meaningful in particular when high density pattern formation is required to enhance pattern transfer fidelity.

Second, magnetic applications have been demonstrated by using S4VP self-assembly and S4VP directed AAO self-assembly. $[Co/Pd]_n$ multilayer patterned magnetic recording media with an anti-dot structure have been created on a hole-patterned Si substrate by using S4VP self assembly. It was observed that the magnetic

properties of $[Co/Pd]_n$ multilayer was altered and improved by nanostructuring Co/Pd multilayer, resulting in significantly improved coercive force with strong perpendicular magnetic anisotropy.

In addition, vertically aligned Ni nanowires have been created into an S4VP-guided AAO membrane on a Si substrate. Ordered AAO pore arrays anodized from Al thin film have not been often reported because of rather limited amount of aluminum material in the film geometry. In this thesis, successful demonstration of ordered AAO pore arrays suitable for 1-D materials synthesis have been accomplished from such thin film AAO nanotemplates. Vertically aligned NiNWs with the average diameter as small as ~30 nm, one of important exemplary materials, were electrochemically synthesized. Due to shape anisotropy of vertically aligned NiNWs, perpendicular magnetic anisotropy was also observed. It is worthwhile to further investigate various approaches of long-range ordered BCP patterns and guided AAO assembly, and AAO pattern multiplications in order to achieve high density nanoarrays using efficient and viable self-assembly technique.

Third, highly hexagonally ordered, vertically parallel aluminum oxide nanotube array was fabricated via hard anodization technique. Due to the high-current anodizing process, noticeable voids are formed along the AAO cell boundaries located at triple cell junction, which enhances the separation of adjacent nanotubes during pore widening process. The Al_2O_3 nanotube arrays so fabricated exhibit a uniform and reproducible dimension, and a quite high aspect ratio of greater than ~1,000. Such high-aspect-ratio, mechanically robust, large-surface-area nanotube array structure can be useful for many technical applications.

For potential applications in biomedical research, the controlled release of antibiotics such as amoxicillin from anodic alumina oxide (AAO) nanotubes was investigated. Study of nanomaterials science and engineering to elucidate factors affecting a sustained release of drugs/catalyst molecules from the AAO nanotubes is highly desirable. In the future, accurate control of the physical dimension of nanotubes, the surface chemistry of the platform, its interaction with the stored materials, and alteration or constriction of the nanotube pore entrance dimension can be attempted for control of drug release kinetics. Moreover, the potential advantages of using AAO nanotubes as a unique alternative in terms of therapeutics concepts for implant surface coatings have been demonstrated.

REFERENCES

1. Keller, F., M.S. Hunter, and D.L. Robinson, *Structural features of oxide coatings on aluminium.* Journal of the Electrochemical Society, 1953. **100**(9): p. 411-419.

2. Bradhurs.Dh and J.S.L. Leach, *Mechanical properties of thin anodic films on aluminum.* Journal of the Electrochemical Society, 1966. **113**(12): p. 1245-&.

3. Diggle, J.W., T.C. Downie, and C.W. Goulding, *Anodic oxide films on aluminum.* Chemical Reviews, 1969. **69**(3): p. 365-&.

4. Osulliva.Jp and G.C. Wood, *Morphology and mechanism of formation of porous anodic films on aluminium.* Proceedings of the Royal Society of London Series a-Mathematical and Physical Sciences, 1970. **317**(1531): p. 511-&.

5. Despić, A. and V.P. Parkhutik, *Electrochemistry of aluminum in aqueous solutions and physics of its anodic oxide.* Modern Aspects of Electrochemistry, 1989. **20**: p. 401-503.

6. Masuda, H. and K. Fukuda, *Ordered metal nanohole arrays made by a 2-step replication of honeycomb structures of anodic alumina.* Science, 1995. **268**(5216): p. 1466-1468.

7. Martin, C.R., *NANOMATERIALS - A MEMBRANE-BASED SYNTHETIC APPROACH.* Science, 1994. **266**(5193): p. 1961-1966.

8. Li, F.Y., L. Zhang, and R.M. Metzger, *On the growth of highly ordered pores in anodized aluminum oxide.* Chemistry of Materials, 1998. **10**(9): p. 2470-2480.

9. Jessensky, O., F. Muller, and U. Gosele, *Self-organized formation of hexagonal pore arrays in anodic alumina.* Applied Physics Letters, 1998. **72**(10): p. 1173-1175.

10. Lei, Y., W.P. Cai, and G. Wilde, *Highly ordered nanostructures with tunable size, shape and properties: A new way to surface nano-patterning using ultra-thin alumina masks.* Progress in Materials Science, 2007. **52**(4): p. 465-539.

11. Sun, Z.J. and H.K. Kim, *Growth of ordered, single-domain, alumina nanopore arrays with holographically patterned aluminum films.* Applied Physics Letters, 2002. **81**(18): p. 3458-3460.

12. Masuda, H., F. Hasegwa, and S. Ono, *Self-ordering of cell arrangement of anodic porous alumina formed in sulfuric acid solution.* Journal of the Electrochemical Society, 1997. **144**(5): p. L127-L130.

13. Masuda, H., K. Yada, and A. Osaka, *Self-ordering of cell configuration of anodic porous alumina with large-size pores in phosphoric acid solution.* Japanese Journal of Applied Physics Part 2-Letters, 1998. **37**(11A): p. L1340-L1342.

14. Li, A.P., et al., *Hexagonal pore arrays with a 50-420 nm interpore distance formed by self-organization in anodic alumina.* Journal of Applied Physics, 1998. **84**(11): p. 6023-6026.

15. Lee, W., K. Nielsch, and U. Gosele, *Self-ordering behavior of nanoporous anodic aluminum oxide (AAO) in malonic acid anodization.* Nanotechnology, 2007. **18**(47).

16. Lee, W., et al., *Fast fabrication of long-range ordered porous alumina membranes by hard anodization.* Nature Materials, 2006. **5**(9): p. 741-747.

17. Lee, W., et al., *Structural engineering of nanoporous anodic aluminium oxide by pulse anodization of aluminium.* Nature Nanotechnology, 2008. **3**(4): p. 234-239.

18. Lee, W., R. Scholz, and U. Gosele, *A continuous process for structurally well-defined Al2O3 nanotubes based on pulse anodization of aluminum.* Nano Letters, 2008. **8**(8): p. 2155-2160.

19. Schwirn, K., et al., *Self-ordered anodic aluminum oxide formed by H2SO4 hard anodization.* Acs Nano, 2008. **2**(2): p. 302-310.

20. Lohrengel, M.M., *Thin anodic oxide layers on aluminum and other valve metals- high-field regime.* Materials Science & Engineering R-Reports, 1993. **11**(6): p. 243-294.

21. Ono, S., et al., *Controlling factor of self-ordering of anodic porous alumina.* Journal of the Electrochemical Society, 2004. **151**(8): p. B473-B478.

22. Shingubara, S., et al., *Self-organization of a porous alumina nanohole array using a sulfuric/oxalic acid mixture as electrolyte.* Electrochemical and Solid State Letters, 2004. **7**(3): p. E15-E17.

23. Nielsch, K., et al., *Self-ordering regimes of porous alumina: The 10% porosity rule.* Nano Letters, 2002. **2**(7): p. 677-680.

24. Jessensky, O., F. Muller, and U. Gosele, *Self-organized formation of hexagonal pore structures in anodic alumina.* Journal of the Electrochemical Society, 1998. **145**(11): p. 3735-3740.

25. Chu, S.Z., et al., *Fabrication of ideally ordered nanoporous alumina films and integrated alumina nanotubule arrays by high-field anodization.* Advanced Materials, 2005. **17**(17): p. 2115-+.

26. Liu, C.Y., A. Datta, and Y.L. Wang, *Ordered anodic alumina nanochannels on focused-ion-beam-prepatterned aluminum surfaces.* Applied Physics Letters, 2001. **78**(1): p. 120-122.

27. Masuda, H., K. Kanezawa, and K. Nishio, *Fabrication of ideally ordered nanohole arrays in anodic porous alumina based on nanoindentation using scanning probe microscope.* Chemistry Letters, 2002(12): p. 1218-1219.

28. Chou, S.Y., P.R. Krauss, and P.J. Renstrom, *Nanoimprint lithography.* Journal of Vacuum Science & Technology B, 1996. **14**(6): p. 4129-4133.

29. Chou, S.Y., P.R. Krauss, and P.J. Renstrom, *Imprint of sub-25nm vias and trenches in polymers.* Applied Physics Letters, 1995. **67**(21): p. 3114-3116.

30. Chou, S.Y., P.R. Krauss, and P.J. Renstrom, *Imprint lithography with 25-nanometer resolution.* Science, 1996. **272**(5258): p. 85-87.

31. Masuda, H., et al., *Highly ordered nanochannel-array architecture in anodic alumina.* Applied Physics Letters, 1997. **71**(19): p. 2770-2772.

32. Masuda, H., K. Yasui, and K. Nishio, *Fabrication of ordered arrays of multiple nanodots using anodic porous alumina as an evaporation mask.* Advanced Materials, 2000. **12**(14): p. 1031-1033.

33. Masuda, H., et al., *Self-repair of ordered pattern of nanometer dimensions based on self-compensation properties of anodic porous alumina.* Applied Physics Letters, 2001. **78**(6): p. 826-828.

34. Masuda, H., et al., *Ordered mosaic nanocomposites in anodic porous alumina.* Advanced Materials, 2003. **15**(2): p. 161-164.

35. Choi, J., et al., *Fabrication of monodomain alumina pore arrays with an interpore distance smaller than the lattice constant of the imprint stamp.* Journal of Vacuum Science & Technology B, 2003. **21**(2): p. 763-766.

36. Kim, B.Y., et al., *Fabrication of ordered anodic aluminum oxide using a solvent-induced array of block-copolymer micelles.* Small, 2007. **3**(11): p. 1869-1872.

37. Choi, J., R.B. Wehrspohn, and U. Gosele, *Mechanism of guided self-organization producing quasi-monodomain porous alumina.* Electrochimica Acta, 2005. **50**(13): p. 2591-2595.

38. Park, C., J. Yoon, and E.L. Thomas, *Enabling nanotechnology with self assembled block copolymer patterns.* Polymer, 2003. **44**(22): p. 6725-6760.

39. Fasolka, M.J. and A.M. Mayes, *Block copolymer thin films: Physics and applications.* Annual Review of Materials Research, 2001. **31**: p. 323-355.

40. Vettiger, P., et al., *The "Millipede" - More than one thousand tips for future AFM data storage.* Ibm Journal of Research and Development, 2000. **44**(3): p. 323-340.

41. Piner, R.D., et al., *"Dip-pen" nanolithography.* Science, 1999. **283**(5402): p. 661-663.

42. Ginger, D.S., H. Zhang, and C.A. Mirkin, *The evolution of dip-pen nanolithography.* Angewandte Chemie-International Edition, 2004. **43**(1): p. 30-45.

43. Parkhutik, V.P., J.M. Albella, and J.M. Martinez-Duart, *Electric breakdown in anodic oxide films.* Modern Aspects of Electrochemistry, 1992. **23**: p. 315-391.

44. Lee, W., J.C. Kim, and U. Gosele, *Spontaneous Current Oscillations during Hard Anodization of Aluminum under Potentiostatic Conditions.* Advanced Functional Materials, 2010. **20**(1): p. 21-27.

45. Li, D.D., et al., *Self-Assembly of Periodic Serrated Nanostructures.* Chemistry of Materials, 2009. **21**(2): p. 253-258.

46. Li, D.D., et al., *Formation of Anodic Aluminum Oxide with Serrated Nanochannels.* Nano Letters, 2010. **10**(8): p. 2766-2771.

47. Crossland, A.C., et al., *Residual flaws due to formation of oxygen bubbles in anodic alumina.* Corrosion Science, 1999. **41**(10): p. 1945-1954.

48. Skeldon, P., et al., *Evidence of oxygen bubbles formed within anodic films on aluminium-copper alloys.* Philosophical Magazine a-Physics of Condensed Matter Structure Defects and Mechanical Properties, 1997. **76**(4): p. 729-741.

49. Losic, D., *Preparation of Porous Anodic Alumina with Periodically Perforated Pores.* Langmuir, 2009. **25**(10): p. 5426-5431.

50. Zhao, S.Y., et al., *Novel structure of AAO film fabricated by constant current anodization.* Advanced Materials, 2007. **19**(19): p. 3004-+.

51. Li, Y., et al., *Novel AAO films and hollow nanostructures fabricated by ultra-high voltage hard anodization.* Chemical Communications, 2010. **46**(2): p. 309-311.

52. Pu, L., et al., *Individual alumina nanotubes.* Angewandte Chemie-International Edition, 2001. **40**(8): p. 1490-+.

53. Noh, K., et al., *Highly Self-assembled Nanotubular Aluminum Oxide by Hard Anodization.* Journal of Materials Research, 2011. **26**(2): p. 186-193.

54. Noh, K., et al., *A New Nano-Platform for Drug Release via Nanotubular Aluminum Oxide.* Journal of Biomaterials and Nanobiotechnology (Accepted), 2011.

55. Macdonald, D.D., *On the formation of voids in anodic oxide-films on aluminum.* Journal of the Electrochemical Society, 1993. **140**(3): p. L27-L30.

56. Mei, Y.F., et al., *Formation mechanism of alumina nanotube array.* Physics Letters A, 2003. **309**(1-2): p. 109-113.

57. Houser, J.E. and K.R. Hebert, *The role of viscous flow of oxide in the growth of self-ordered porous anodic alumina films.* Nature Materials, 2009. **8**(5): p. 415-420.

58. Ono, S., H. Ichinose, and N. Masuko, *Defects in porous anodic films formed on high-purity aluminum.* Journal of the Electrochemical Society, 1991. **138**(12): p. 3705-3710.

59. Habazaki, H., et al., *Inter-relationships between ionic transport and composition in amorphous anodic oxides.* Proceedings of the Royal Society of London Series a-Mathematical Physical and Engineering Sciences, 1997. **453**(1963): p. 1593-1609.

60. Wuthrich, N., *Intrinsic stresses in anodic films on aluminum.* Electrochimica Acta, 1981. **26**(11): p. 1617-1623.

61. Fredrickson, G.H. and F.S. Bates, *Dynamics of block copolymers: Theory and experiment.* Annual Review of Materials Science, 1996. **26**: p. 501-550.

62. Bates, F.S., *POLYMER-POLYMER PHASE-BEHAVIOR.* Science, 1991. **251**(4996): p. 898-905.

63. Leibler, L., *THEORY OF MICROPHASE SEPARATION IN BLOCK CO-POLYMERS.* Macromolecules, 1980. **13**(6): p. 1602-1617.

64. Fredrickson, G.H. and E. Helfand, *FLUCTUATION EFFECTS IN THE THEORY OF MICROPHASE SEPARATION IN BLOCK COPOLYMERS.* Journal of Chemical Physics, 1987. **87**(1): p. 697-705.

65. Ruiz, R., et al., *Density multiplication and improved lithography by directed block copolymer assembly.* Science, 2008. **321**(5891): p. 936-939.

66. Park, S., et al., *Macroscopic 10-Terabit-per-Square- Inch Arrays from Block Copolymers with Lateral Order.* Science, 2009. **323**(5917): p. 1030-1033.

67. Masuda, H. and M. Satoh, *Fabrication of gold nanodot array using anodic porous alumina as an evaporation mask.* Japanese Journal of Applied Physics Part 2-Letters, 1996. **35**(1B): p. L126-L129.

68. Li, C.P., et al., *Fabrication and structural characterization of highly ordered sub-100-nm planar magnetic nanodot arrays over 1 cm(2) coverage area.* Journal of Applied Physics, 2006. **100**(7): p. 074318.

69. Bandyopadhyay, S., et al., *Electrochemically assembled quasi-periodic quantum dot arrays.* Nanotechnology, 1996. **7**(4): p. 360-371.

70. Gapin, A.I., et al., *CoPt patterned media in anodized aluminum oxide templates.* Journal of Applied Physics, 2006. **99**(8): p. 08G902.

71. Li, Y., et al., *Preparation of cadmium sulfide nanowire arrays in anodic aluminum oxide templates.* Chemistry of Materials, 1999. **11**(12): p. 3433-3435.

72. Metzger, R.M., et al., *Magnetic nanowires in hexagonally ordered pores of alumina.* Ieee Transactions on Magnetics, 2000. **36**(1): p. 30-35.

73. Nicewarner-Pena, S.R., et al., *Submicrometer metallic barcodes.* Science, 2001. **294**(5540): p. 137-141.

74. Choi, J.R., et al., *Massive fabrication of free-standing one-dimensional Co/Pt nanostructures and modulation of ferromagnetism via a programmable barcode layer effect.* Nano Letters, 2005. **5**(11): p. 2179-2183.

75. Lee, J.H., et al., *Iron-gold barcode nanowires.* Angewandte Chemie-International Edition, 2007. **46**(20): p. 3663-3667.

76. Matsumoto, F., et al., *Nanometer-scale patterning of DNA in controlled intervals on a gold-disk array fabricated using ideally ordered anodic porous alumina.* Advanced Materials, 2005. **17**(13): p. 1609-1612.

77. Masuda, H., et al., *Square and triangular nanohole array architectures in anodic alumina.* Advanced Materials, 2001. **13**(3): p. 189-192.

78. Park, J., et al., *Geometry transformation and alterations of periodically patterned Si nanotemplates by dry oxidation.* Nanotechnology, 2009. **20**(1).

79. Oh, S., et al., *Significantly accelerated osteoblast cell growth on aligned TiO2 nanotubes.* Journal of Biomedical Materials Research Part A, 2006. **78A**(1): p. 97-103.

80. Oh, S., et al., *Stem cell fate dictated solely by altered nanotube dimension.* Proc Natl Acad Sci U S A, 2009. **106**(7): p. 2130-5.

81. Park, M., et al., *Block copolymer lithography: Periodic arrays of similar to 10(11) holes in 1 square centimeter.* Science, 1997. **276**(5317): p. 1401-1404.

82. Glass, R., et al., *Micro-nanostructured interfaces fabricated by the use of inorganic block copolymer micellar monolayers as negative resist for electron-beam lithography.* Advanced Functional Materials, 2003. **13**(7): p. 569-575.

83. Glass, R., et al., *Block copolymer micelle nanolithography on non-conductive substrates.* New Journal of Physics, 2004. **6**.

84. Glass, R., M. Moller, and J.P. Spatz, *Block copolymer micelle nanolithography.* Nanotechnology, 2003. **14**(10): p. 1153-1160.

85. Zeper, W.B., et al., *Perpendicular magnetic-anisotropy and magneto-optical Kerr effect of vapor-deposited Co/Pt-layered structures.* Journal of Applied Physics, 1989. **65**(12): p. 4971-4975.

86. Zeper, W.B., et al., *Hysteresis, microstructure, and magnetooptical recording in Co/Pd multilayers.* Journal of Applied Physics, 1991. **70**(4): p. 2264-2271.

87. Adeyeye, A.O., J.A.C. Bland, and C. Daboo, *Magnetic properties of arrays of "holes" in Ni80Fe20 films.* Applied Physics Letters, 1997. **70**(23): p. 3164-3166.

88. Choe, S.B. and S.C. Shin, *Magnetization reversal in nanostructured Co/Pd multilayers.* Physical Review B, 1998. **57**(2): p. 1085-1089.

89. Wang, C.C., A.O. Adeyeye, and N. Singh, *Magnetic antidot nanostructures: effect of lattice geometry.* Nanotechnology, 2006. **17**(6): p. 1629-1636.

90. Shin, K., et al., *A simple route to metal nanodots and nanoporous metal films.* Nano Letters, 2002. **2**(9): p. 933-936.

91. Kim, S.H., et al., *Highly oriented and ordered arrays from block copolymers via solvent evaporation.* Advanced Materials, 2004. **16**(3): p. 226-+.

92. Yun, S.H., et al., *Highly ordered arrays of nanoparticles in large areas from diblock copolymer micelles in hexagonal self-assembly.* Chemistry of Materials, 2006. **18**(24): p. 5646-5648.

93. Hellwig, O., et al., *Bit patterned media based on block copolymer directed assembly with narrow magnetic switching field distribution.* Applied Physics Letters, 2010. **96**(5).

94. Zschech, D., et al., *Ordered arrays of < 100 >-oriented silicon nanorods by CMOS-compatible block copolymer lithography.* Nano Letters, 2007. **7**(6): p. 1516-1520.

95. Park, H.J., M.G. Kang, and L.J. Guo, *Large Area High Density Sub-20 nm SiO2 Nanostructures Fabricated by Block Copolymer Template for Nanoimprint Lithography.* Acs Nano, 2009. **3**(9): p. 2601-2608.

96. Chao, C.C., et al., *Robust Block Copolymer Mask for Nanopatterning Polymer Films.* Acs Nano, 2010. **4**(4): p. 2088-2094.

97. Noh, K., et al., *Magnetic properties of anti-dot patterned Co/Pd multilayer film.* IEEE Transactions on Magnetics, 2011.

98. Park, S., et al., *Fabrication of highly ordered silicon oxide dots and stripes from block copolymer thin films.* Advanced Materials, 2008. **20**(4): p. 681-+.

99. Shin, K., et al., *Curving and frustrating flatland.* Science, 2004. **306**(5693): p. 76-76.

100. Xiang, H.Q., et al., *Block copolymers under cylindrical confinement.* Macromolecules, 2004. **37**(15): p. 5660-5664.

101. Xiang, H., et al., *From cylinders to helices upon confinement.* Macromolecules, 2005. **38**(4): p. 1055-1056.

102. Sun, Y.M., et al., *Diameter-dependence of the morphology of PS-b-PMMA nanorods confined within ordered porous alumina templates.* Macromolecular Rapid Communications, 2005. **26**(5): p. 369-375.

103. Wang, Y., U. Gosele, and M. Steinhart, *Mesoporous Block Copolymer Nanorods by Swelling-induced Morphology Reconstruction.* Nano Letters, 2008. **8**(10): p. 3548-3553.

104. Li, L., N. Koshizaki, and G.H. Li, *Nanotube arrays in porous anodic alumina membranes.* Journal of Materials Science & Technology, 2008. **24**(4): p. 550-562.

105. Briggs, E.P., et al., *Formation of highly adherent nano-porous alumina on Ti-based substrates: a novel bone implant coating.* Journal of Materials Science-Materials in Medicine, 2004. **15**(9): p. 1021-1029.

106. Wieneke, H., et al., *Synergistic effects of a novel nanoporous stent coating and tacrolimus on intima proliferation in rabbits.* Catheterization and Cardiovascular Interventions, 2003. **60**(3): p. 399-407.

107. Gultepe, E., et al., *Sustained Drug Release from Non-eroding Nanoporous Templates.* Small, 2010. **6**(2): p. 213-216.

108. Oteiza, P.I., *A mechanism for the stimulatory effect of aluminum on iron-induced lipid-peroxidation.* Archives of Biochemistry and Biophysics, 1994. **308**(2): p. 374-379.

109. Smith, M.A., et al., *Oxidative stress in Alzheimer's disease.* Biochimica Et Biophysica Acta-Molecular Basis of Disease, 2000. **1502**(1): p. 139-144.

110. Parkinson, L.G., et al., *The Potential of Nanoporous Anodic Aluminium Oxide Membranes to Influence Skin Wound Repair.* Tissue Engineering Part A, 2009. **15**(12): p. 3753-3763.

111. Walpole, A.R., et al., *Nano-porous alumina coatings for improved bone implant interfaces.* Materialwissenschaft Und Werkstofftechnik, 2003. **34**(12): p. 1064-1068.

112. Huang, K.T., Z. Huang, and D.B. Kim-Shapiro, *Nitric oxide red blood cell membrane permeability at high and low oxygen tension.* Nitric Oxide-Biology and Chemistry, 2007. **16**(2): p. 209-216.

113. Gong, D.W., et al., *Controlled molecular release using nanoporous alumina capsules.* Biomedical Microdevices, 2003. **5**(1): p. 75-80.

114. Kang, H.J., et al., *Controlled drug release using nanoporous anodic aluminum oxide on stent.* Thin Solid Films, 2007. **515**(12): p. 5184-5187.

115. Darder, M., et al., *Encapsulation of enzymes in alumina membranes of controlled pore size.* Thin Solid Films, 2006. **495**(1-2): p. 321-326.

116. Gultepe, E., et al., *Sustained drug release from non-eroding nanoporous templates.* Small, 2010. **6**(2): p. 213-6.

117. Losic, D. and S. Simovic, *Self-ordered nanopore and nanotube platforms for drug delivery applications.* Expert Opinion on Drug Delivery, 2009. **6**(12): p. 1363-1381.

118. Simovic, S., D. Losic, and K. Vasilev, *Controlled drug release from porous materials by plasma polymer deposition.* Chemical Communications, 2010. **46**(8): p. 1317-1319.

119. Swan, E.E.L., et al., *Fabrication and evaluation of nanoporous alumina membranes for osteoblast culture.* Journal of Biomedical Materials Research Part A, 2005. **72A**(3): p. 288-295.

120. Popat, K.C., et al., *Influence of nanoporous alumina membranes on long-term osteoblast response.* Biomaterials, 2005. **26**(22): p. 4516-4522.

121. Huang, G.S., et al., *Formation mechanism of individual alumina nanotubes wrapping metal (Cu and Fe) nanowires.* Journal of Crystal Growth, 2006. **289**(1): p. 295-298.

122. Wang, C.C., et al., *Organic nanowire-templated fabrication of alumina nanotubes by atomic layer deposition.* Nano Letters, 2007. **7**(6): p. 1566-1569.

123. Lu, C.L., et al., *Crystalline nanotubes of gamma-AlOOH and gamma-Al2O3: hydrothermal synthesis, formation mechanism and catalytic performance.* Nanotechnology, 2009. **20**(21).

124. Jin, S., *Tactile sensor comprising nanowires and method for making the same.* US Patent, 2001. **No. 6,286,226**.

125. Deck, C.P., et al., *The response of carbon nanotube ensembles to fluid flow: Applications to mechanical property measurement and diagnostics.* Journal of Applied Physics, 2009. **106**(7).

126. Brammer, K.S., et al., *Antibiofouling, Sustained Antibiotic Release by Si Nanowire Templates.* Nano Letters, 2009. **9**(10): p. 3570-3574.

127. Feng, B., et al., *Characterization of surface oxide films on titanium and bioactivity.* Journal of Materials Science-Materials in Medicine, 2002. **13**(5): p. 457-464.

128. Popat, K.C., et al., *Influence of engineered titania nanotubular surfaces on bone cells.* Biomaterials, 2007. **28**(21): p. 3188-97.

129. Brammer, K.S., et al., *Improved bone-forming functionality on diameter-controlled TiO2 nanotube surface.* Acta Biomaterialia, 2009. **5**(8): p. 3215-3223.

130. Vallet-Regi, M., et al., *Hexagonal ordered mesoporous material as a matrix for the controlled release of amoxicillin.* Solid State Ionics, 2004. **172**(1-4): p. 435-439.

131. Geisler, S., *Orally administered amoxicillin decreases the risk of implant failures.* J Am Dent Assoc, 2009. **140**(10): p. 1294-6.

132. Esposito, M., et al., *Interventions for replacing missing teeth: antibiotics at dental implant placement to prevent complications.* Cochrane Database of Systematic Reviews, 2008(3): p. 1-20.

133. Beardmore, A.A., et al., *Effectiveness of local antibiotic delivery with an osteoinductive and osteoconductive bone-graft substitute.* Journal of Bone and Joint Surgery-American Volume, 2005. **87A**(1): p. 107-112.

134. Ostermann, P.A., D. Seligson, and S.L. Henry, *Local antibiotic therapy for severe open fractures. A review of 1085 consecutive cases.* J Bone Joint Surg Br, 1995. **77**(1): p. 93-7.

135. Turgut, H., et al., *Systemic and local antibiotic prophylaxis in the prevention of Staphylococcus epidermidis graft infection.* Bmc Infectious Diseases, 2005. **5**(91): p.1-6.

136. Mark Saltzman, W. and S.P. Baldwin, *Materials for protein delivery in tissue engineering.* Adv Drug Deliv Rev, 1998. **33**(1-2): p. 71-86.

137. Rosenholm, J.M. and M. Linden, *Towards establishing structure-activity relationships for mesoporous silica in drug delivery applications.* J Control Release, 2008. **128**(2): p. 157-64.

138. Jiang, G., et al., *Assessment of protein release kinetics, stability and protein polymer interaction of lysozyme encapsulated poly(D,L-lactide-co-glycolide) microspheres.* J Control Release, 2002. **79**(1-3): p. 137-45.

139. Martin, F., et al., *Tailoring width of microfabricated nanochannels to solute size can be used to control diffusion kinetics.* J Control Release, 2005. **102**(1): p. 123-33.

140. Bayomi, M.A., *Geometric Approach for Zero-Order Release of Drugs Dispersed in an Inert Matrix.* Pharmaceutical Research, 1994. **11**(6): p. 914-916.

141. Higuchi, T., *Rate of release of medicaments from ointment bases containing drugs in suspension.* J Pharm Sci, 1961. **50**: p. 874-5.

142. Higuchi, T., *Mechanism of Sustained-Action Medication. Theoretical Analysis of Rate of Release of Solid Drugs Dispersed in Solid Matrices.* J Pharm Sci, 1963. **52**: p. 1145-9.

143. Roy, I., et al., *Ceramic-based nanoparticles entrapping water-insoluble photosensitizing anticancer drugs: a novel drug-carrier system for photodynamic therapy.* J Am Chem Soc, 2003. **125**(26): p. 7860-5.

144. Losic, D. and S. Simovic, *Self-ordered nanopore and nanotube platforms for drug delivery applications.* Expert Opin Drug Deliv, 2009. **6**(12): p. 1363-81.

145. Popat, K.C., et al., *Titania nanotubes: a novel platform for drug-eluting coatings for medical implants?* Small, 2007. **3**(11): p. 1878-81.